

**UNCERTAINTY QUANTIFICATION
IN DAMAGE MECHANICS MODELS**

by

Jerome Troy

A dissertation submitted to the Faculty of the University of Delaware in partial fulfillment of the requirements for the degree of Doctor of Philosophy in Applied Mathematics

Summer 2023

© 2023 Jerome Troy
All Rights Reserved

**UNCERTAINTY QUANTIFICATION
IN DAMAGE MECHANICS MODELS**

by

Jerome Troy

Approved: _____
Mark Gockenbach, Ph.D.
Chair of the Department of Mathematical Sciences

Approved: _____
John A. Pelesko, Ph.D.
Dean of the College of Arts and Sciences

Approved: _____
Louis F. Rossi, Ph.D.
Vice Provost for Graduate and Professional Education and
Dean of the Graduate College

I certify that I have read this dissertation and that in my opinion it meets the academic and professional standard required by the University as a dissertation for the degree of Doctor of Philosophy.

Signed: _____
Petr Plechac, Ph.D.
Professor in charge of dissertation

I certify that I have read this dissertation and that in my opinion it meets the academic and professional standard required by the University as a dissertation for the degree of Doctor of Philosophy.

Signed: _____
Gideon Simpson, Ph.D.
Member of dissertation committee

I certify that I have read this dissertation and that in my opinion it meets the academic and professional standard required by the University as a dissertation for the degree of Doctor of Philosophy.

Signed: _____
Jingmei Qiu, Ph.D.
Member of dissertation committee

I certify that I have read this dissertation and that in my opinion it meets the academic and professional standard required by the University as a dissertation for the degree of Doctor of Philosophy.

Signed: _____
Constantin Bacuta, Ph.D.
Member of dissertation committee

ACKNOWLEDGEMENTS

I thank my advisor, Dr. Petr Plechac, for his continuous support, understanding, and guidance. I have learned so much from you, and working alongside you has been an honor. I will continue to model your example in all my future endeavors. I would also like to thank my other committee members - Drs. Gideon Simpson, Jingmei Qiu, and Constantin Bacuta, for mentoring me and showing me new areas related to my research. I also wish to thank the Department of Mathematical Sciences staff, including Pascale Larouche, David Caldwell, the late Deb See, and Pam Irwin. Finally, I would also like to thank Dr. Jarek Knap of the Army Research Office for the financial support of this research.

The friends I have made here in Delaware have made for a beautiful experience. Joseph and Dan, thank you for making this an incredible adventure. Thank you for always being willing to talk about our problems, both mathematical and worldly. To my parents, Carol and Jay, thank you for your unwavering support, love, and encouragement.

Last, and most of all, I want to thank my wife, Kristen, who has always supported me. Thank you for being there even during sleepless nights and early mornings to walk Rocket. Thank you for listening to me endlessly talk about mathematics. Thank you for providing feedback and support, even when I have gotten on your last nerve. Thank you for helping me to step outside my comfort zone and for always being open to new experiences. I could not have done this without you. I hope the next chapter of our lives is even more wonderful.

TABLE OF CONTENTS

LIST OF TABLES	ix
LIST OF FIGURES	x
LIST OF SYMBOLS	xv
ABSTRACT	xviii
 Chapter	
1 INTRODUCTION	1
2 THE DAMAGE MECHANICS PROBLEM	7
2.1 Introduction	7
2.2 Elastodynamics Damage Mechanics Model	8
2.2.1 1D problem and Well Posedness	14
2.3 Numerical Solution of the Damage Mechanics Model	18
2.3.1 Semidiscretization via P1 Finite Elements	19
2.3.2 Quadratures for Finite Element Representation	21
2.3.3 Modified Generalized- α method	23
2.3.4 Verification of Orders of Accuracy	25
3 RANDOM FIELDS	28
3.1 Introduction and Notation	28
3.2 Univariate Random Variables	29
3.3 Vector Valued Random Variables	31
3.4 Random Fields	32
3.5 Computing the Eigendecomposition of the Covariance Operator	35
3.5.1 Numerical Eigendecomposition	35
3.5.2 Examples of Covariance Operators	37

3.5.3	Log Normal Fields	41
3.5.4	Weibull Fields [61]	41
3.6	Computational Procedure for Sampling Random Fields	41
4	UNCERTAINTY QUANTIFICATION	47
4.1	Introduction	47
4.2	Methods for UQ of QoIs	48
4.2.1	Polynomial Chaos	48
4.2.2	Monte Carlo Methods	50
4.3	Statistical Concepts and Monte Carlo Methods	50
4.3.1	Parametric Statistics and The Maximum Likelihood Estimator	54
4.3.2	Nonparametric Statistics	55
4.4	Uncertainty in Probability Measure	57
4.5	Relative Entropy Between Select Distributions	61
4.5.1	Gaussian Vectors	61
4.5.2	Gaussian Fields	62
4.5.3	Example Relative Entropy Between Two Gaussian Fields . . .	64
4.5.4	Log Normal Fields	66
4.5.5	Weibull Fields	68
4.5.5.1	Relative Entropy Between Univariate Weibulls	69
4.5.5.2	Relative Entropy Between Weibull and Log Normal Variables	72
5	MONTE CARLO SAMPLING FOR SOME QUANTITIES OF INTEREST	78
5.1	Introduction	78
5.2	Expanding Ring and Counting Fragments	78
5.2.1	Geometry and Boundary Conditions	79
5.2.2	Fragment Counts	81
5.2.3	Monte Carlo Sampling	81
5.3	One Dimensional Uniaxial Strain	83

5.4	Two Dimensional Uniaxial Strain Problem	85
5.4.1	Domain and Boundary Conditions	85
5.4.2	Time of First Damage	87
5.4.3	Stress-Strain Curve	89
5.5	Notched Uniaxial Stress Problem	91
5.5.1	Domain and Boundary Conditions	91
5.5.2	Stopping Times - Initial Damage and Time of Breaking	93
5.5.3	Stress-Strain Curve	95
5.5.4	Damage Distribution	98
5.6	Conclusions from MC Sampling	100
6	MULTILEVEL MONTE CARLO SAMPLING FOR QUANTITIES OF INTEREST	103
6.1	Introduction	103
6.2	Standard MLMC	104
6.3	Conditional MLMC for Probabilities	109
6.3.1	Evaluating Conditional Probabilities	110
6.3.1.1	Brute-Force by Subsampling	111
6.3.1.2	KDE by Subsampling	111
6.3.1.3	Sum of Indicators	112
6.3.1.4	Joint KDE	113
6.3.2	Measure of Precision for MLMC Distribution	113
6.4	Notched Uniaxial Stress Problem	115
6.4.1	Domain and Boundary Conditions	115
6.4.2	MLMC Hierarchy and QoIs	117
6.4.3	Stress-Strain Curve	118
6.4.4	Stopping Times - Initial Damage and Time of Breaking	119
6.4.5	Damage Distribution	124
6.5	MLMC on One Dimensional Model for Various Time Steps	126
6.5.1	Stress Strain Curve	128

6.5.2	Stopping Time	129
6.6	MLMC Between 1D and 2D Models	130
6.6.1	Quantities of Interest	135
6.6.2	MLMC Sampling and Results	136
6.6.3	Results	137
6.7	Discussion and Conclusions	140
	BIBLIOGRAPHY	142
	Appendix	
	A PYTHON CODE AND ALGORITHMS USED	149

LIST OF TABLES

6.1	MLMC Hierarchy for number of samples on each refinement level in the notched uniaxial stress problem. The number of samples at each level were rounded up to the nearest 5 for a more elegant and intuitive distribution. The total cost of each refinement level in CPU-hours is also tabulated including the total cost for the MLMC ensemble. . .	118
6.2	Hierarchy structure of 1D MLMC for various Δt values. Maximum variances over stress-strain curves are also shown.	127
6.3	Number of samples to achieve a variance on the stress-strain curve bounded above by 6×10^{-4} . Values have been rounded up to the nearest 5.	128
6.4	MLMC Workloads for each level in the 1D-2D experiment. Total workload W_ℓ is computed as the product of # DoFs and N_t . The values of # DoFs is the number of degrees of freedom in the spatial discretization, while N_t is the number of time nodes in the chronological integration of the system.	136
6.5	Optimal number of samples for each refinement level in the 1D-2D MLMC uniaxial strain experiment.	137

LIST OF FIGURES

2.1	Comparison between stress-strain relations in brittle and quasi-brittle materials. A brittle material will exhibit a sudden drop in stress exactly at material failure. In contrast, a quasi-brittle material will exhibit a continuing drop in stress over a stress softening length, $\Delta\sigma$.	12
2.2	Spatial convergence results for the linear elastodynamics problem (damage fixed at zero) at the final time step. Mesh resolution is measured based on the minimum cell diameter, and the resulting system exhibits second-order convergence as expected by a $P1$ FEM scheme.	26
2.3	Temporal convergence results for the nonlinear damage mechanics problem using a fixed spatial mesh discretization. Displacement (in blue) and damage (in green) can be seen to be second-order convergent in Δt	27
3.1	Example Random field samples from $X \sim \mathcal{N}(0, \mathcal{C}_\ell)$ for varying values of ℓ . From top to bottom $\ell = 1.0, 0.1$, and 0.01 . From left to right are samples 1 and 2 at each value of ℓ	43
3.2	Example Random field samples from log normal random fields X with $\log X \sim \mathcal{N}(\mu, \mathcal{C}_\ell)$ for varying values of ℓ . From top to bottom $\ell = 1.0, 0.1$, and 0.01 . From left to right are samples 1 and 2 at each value of ℓ	44
3.3	Example Random field samples from Weibull random fields W , for shape parameter $\kappa = 5$, for varying values of ℓ . From top to bottom $\ell = 1.0, 0.1$, and 0.01 . From left to right are samples 1 and 2 at each value of ℓ	45
3.4	Comparison of log-normal and Weibull random fields for various correlation lengths. On the left are two log-normal field samples, and on the right are the corresponding Weibull field samples. Correlation lengths are 1.0 for the top figures and 0.01 for the bottom.	46

4.1	Relative entropy between two Gaussian fields of the form (3.55), in which both are mean-zero, but have differing correlation lengths. For regularity, we take $\alpha = 1$	66
4.2	Log plot of the relative entropy between two scalar Weibull variables. When $r = 1$, the shape parameters of the two Weibull variables are equal, and the relative entropy drops to zero.	71
4.3	Upper: optimal value of k to minimize the relative entropy between a Weibull and log-normal distribution with $\sigma^2 = \lambda$. Lower: minimum relative entropy.	74
4.4	Optimal choice for λ and k to minimize the relative entropy in (4.97) with $\mu = -\sigma^2/2$, for various values of σ	76
4.5	Minimum relative entropy between a mean-1 log-normal variable and a Weibull variable, using the parameter values λ, k indicated from Figure 4.4.	77
5.1	Domain and boundaries for the expanding ring problem.	80
5.2	A sample of the expanding ring problem with damage field plotted. An annular segment $A(\phi, \delta\phi)$ is highlighted in green and shows its width relative to the sizes of the cracks.	82
5.3	Weibull fits on fragment count histograms in the expanding ring problem for various correlation lengths. Upper left: $\ell = 0.01$, upper right: $\ell = 0.05$, lower left: $\ell = 0.1$, and lower right : $\ell = 0.2$. In each plot, the fitted Weibull parameters are listed above, and the black curve indicates the Weibull fit. The vertical black bars indicate a 95% Clopper Pearson confidence interval on each histogram bin.	84
5.4	Domain and boundaries for the uniaxial strain problem in a rectangle.	86
5.5	KDE for the time of first damage in the constant speed uniaxial strain problem. The KDE represents an approximation to the PDF for this stopping time.	88
5.6	CDF for the time of first damage in the constant speed uniaxial strain problem. Also shown is a 95% Clopper-Pearson confidence interval for the CDF, which place bounds on the probability of the stopping time occurring before the specified time.	88

5.7	Average stress-strain curve for the uniaxial strain problem. Shaded in grey is a $\pm 1\zeta$ interval on the individual sample stress-strain curve. In solid blue is the mean estimator for the stress-strain curve, while in shaded blue is a 95% confidence interval on the estimator itself.	90
5.8	Diagram of the domain and boundaries in the notched uniaxial stress problem.	92
5.9	Time evolution of Damage, Stress (nonlinear), and Displacement fields for a selected sample of notched uniaxial stress problem. The yield stress field is displayed in the lower right corner. The displacement plot is warped by the displacement field. This warping is scaled up by a factor of 100. Figures are grouped in 2×2 blocks and vertically in order of $t = 0, 1.5, 3, 4$, respectively.	94
5.10	KDE plot for stopping times in the notched uniaxial stress problem. T_{start} corresponds to the time of damage initiation, while T_{fail} corresponds to the final physical time of the simulation when the crack has propagated through to the other side of the domain. The above PDF approximations were made using 100 samples for each stopping time.	95
5.11	Stress-strain curve estimator with 95% confidence bounds on the estimator (blue - using standard error) and $\pm 1\zeta$ interval on the sample (cyan). In addition, the stress-strain curve corresponding to the sample shown in Figure 5.9 is displayed as a green line.	97
5.12	KDE plots for stopping times corresponding to when the damage starts and the final physical time of the notched uniaxial stress simulation are plotted overtop the stress-strain estimator and confidence intervals. The correspondence of the maximum value in the stress-strain curve with the sharp increase in the distribution of failure times indicates a correlation there, which could be used to evaluate the failure characteristics of these simulations.	99
5.13	Mean, standard deviation, and standard error computed pointwise for $\mathcal{D}_{\text{final}}(\mathbf{x})$ in the notched uniaxial stress problem.	101
6.1	Diagram of the domain and boundaries in the notched uniaxial stress problem.	116

6.2	Stress-strain curve for notched uniaxial stress problem, using an MLMC hierarchy of 100 - 40 - 10 samples on refinement levels 1 - 2 - 3 respectively. For reference, a 95% confidence interval is plotted around the mean stress-strain estimator in blue, and a $\pm 1\varsigma$ interval is plotted for the sample in cyan.	120
6.3	Comparison of stress-strain curve estimators using MLMC and standard MC (see Chapter 5). The green band indicates a 95% confidence interval around the MLMC estimator. As a result, we are able to recover the standard MC estimator to within 95%.	121
6.4	Raw KDEs for stopping times in the notched uniaxial stress problem using MLMC hierarchy. In solid lines are the KDE for T_{start} and in dashed are the KDE for T_{fail}	122
6.5	Construction of stopping time CDF for both T_{start} and T_{fail} . In solid lines are the CDFs constructed using the MLMC probability procedure discussed above. In dashed are the CDFs built using standard MC methods, using 100 samples at the highest refinement level. Using the pointwise variance of the indicator function, 95% confidence intervals are shaded around the MLMC CDF estimators. As a result, we are able to reconstruct the CDF from the MC framework with 95% confidence.	123
6.6	Probability the final physical damage is larger than a cutoff value for the MLMC hierarchy. The only area where this is almost sure is near the tip of the notch on the upper boundary. This fans out as it proceeds lower in the domain, and there are very few regions indicating damage away from the center of the domain.	125
6.7	MLMC Variance on $\mathbb{1}(\mathcal{D}_{\text{final}}(\mathbf{x}) \geq d_0)$. The high variance near the center of the domain indicates variability in crack path. The variations along the sides of the domain indicate that some simulations exhibit additional cracking on the boundaries due to the forcing.	125
6.8	Error between MLMC and MC probability for $\mathbb{P}(\mathcal{D}_{\text{final}} \geq d_0)$	126
6.9	Estimators on the mean stress-strain curve for the 1D uniaxial strain model computed using an MLMC hierarchy (solid) and standard MC procedures (dashed). The banded region indicates a 95% confidence interval around the MLMC estimator.	129

6.10	Comparison of stopping time distributions for various levels in the MLMC hierarchy from Table 6.3 for the 1D uniaxial strain problem. The coarseness of time steps at level 1 create a low quality KDE, while higher refinement levels appear to fix the problem.	131
6.11	Comparison of CDFs for stopping time distribution as computed using an MLMC hierarchy in Table 6.3, and standard MC framework. The MC estimator is within a 95% confidence interval of the MLMC estimator.	132
6.12	Comparison of stress-strain curves and T_{start} KDE for 1D and 2D sampling ensembles before performing MLMC.	138
6.13	Stress-strain curve and PDF for T_{start} estimators using the 1D-2D MLMC sampling distribution. In blue is a 95 % confidence interval around the mean stress-strain curve estimator, and in cyan is a $\pm 1\sigma$ interval indicating UQ bounds.	139

LIST OF SYMBOLS

Sets

- \mathbb{R} Real numbers
- \mathbb{N} Natural numbers $\{1, 2, \dots\}$
- Ω Problem domain
- $\partial\Omega$ Boundary of domain Ω

Material Properties

- ρ Material density
- E Young's Modulus
- ν Poisson Ratio
- λ, μ Lamé parameters, μ is also called the Sheer Modulus
- η_1, η_2 Rayleigh damping parameters for mass and stiffness terms resp.

Damage Mechanics Variables

- Σ Critical Yield Stress Field
- $\sigma^{(L)}$ Linear stress
- \mathcal{D} Damage Field
- $\Delta\sigma$ Stress Softening Length
- σ Material stress

- ε Material strain
- u Material displacement field
- t_{\max} Maximum simulation time
- \mathcal{S} Stress-strain relationship: $\mathcal{S} : \varepsilon \mapsto \sigma$

Variable Modifiers

- \mathbf{u} Indicates numerical vector, as in $A\mathbf{u} = \mathbf{b}$
- \underline{u} Indicates physical vector, such as position, \underline{x}
- $\underline{\underline{\varepsilon}}$ Indicates physical tensor, such as strain tensor, $\underline{\underline{\varepsilon}}$

Random Variables

- X random variable X
- $X^{(n)}$ n 'th sample of random variable X
- $\mathbb{P}(\cdot)$ probability
- $\mathbb{E}[\cdot]$ Expectation value
- $\text{Var}[\cdot]$ Variance
- $\text{Cov}[\cdot, \cdot]$ Covariance
- ζ standard deviation
- $\mathbb{1}(\cdot)$ Indicator function
- $D_{KL}(\cdot || \cdot)$ Kulback-Leibler divergence or Relative entropy
- \implies Converges in distribution

Operators

- $\|\cdot\|_X$ Norm on space X
- $\langle \cdot, \cdot \rangle_X$ inner product on inner product space X
- $\text{Proj}_W u$ projection of u onto space W
- $f \circ g$ Function composition
- \otimes Tensor product on space
- \odot Pointwise vector product, $(1, 2) \odot (2, 3) = (2, 6)$
- ∇ Gradient
- $\nabla \cdot$ Divergence
- $(\cdot)^T$ Transpose

Miscellaneous Symbols

- δ_{ij} Kroneker- δ , $\delta_{ij} = 1$ if $i = j$ and 0 otherwise

ABSTRACT

Computational modeling of material response, at the macroscopic scale, under external stimuli, is paramount to predicting material failure in various structural applications. Material properties often vary within a given sample of material, and these distributions will vary from one sample to another. Various methods can be employed to understand these variations and gain insight into how a material will behave when put under external stresses. These responses can be quantified in specific properties such as stress-strain curves, times of failure, and other quantities of interest (QoIs). These QoIs are random variables, and their distributions can be understood using Monte Carlo techniques. This thesis primarily focuses on using these techniques to analyze the results from a specific damage mechanics model. Damage mechanics simulations can be very expensive computationally, and thus we discuss techniques to reduce the required computational costs while maintaining the same level of accuracy and uncertainty as more traditional methods. We investigate these ideas in multiple settings and for various QoIs. Each scenario presents a new challenge depending on the problem geometry and various properties of the QoIs. We present methods to employ uncertainty quantification (UQ), which are generally agnostic to the underlying model and only require knowledge of the model outputs. The presented results are a survey of techniques and potential experiments which can be employed in multiple fields. To aid with the computational complexity involved in the simulations, we apply Multilevel Monte Carlo methods, which combine results from multiple model resolutions. We extend the application of these Multilevel techniques to building confidence intervals and probability distributions. Similarly, the results can be used in UQ techniques to bound modeling errors between the nominal and potential alternative models.

Chapter 1

INTRODUCTION

In materials science and mechanical engineering, a fundamental problem is understanding how a material will respond to a given external stimuli. Particularly in failure modeling and fracture mechanics, understanding when and how a material will fail is paramount to ensuring structural integrity and determining engineering tolerances for materials in the field. Models for material responses and fracture propagation have undergone extensive research in recent decades and provide mathematical tools and techniques to predict material reactions. Such methods have great diversity, and each has specific scenarios and problems to which it is best suited. Often, these techniques involve modeling material responses at each location in a section of material. This can range from examining models on the granular structure of a material to making mean-field approximations of the material and examining more global behavior. Such models can be intensive computationally, as they often require solving nonlinear systems with many unknowns.

Modeling material responses can be performed at either the macroscopic or microscopic levels. Microscopic models examine the material at the granular structure and usually concern themselves with the formation and propagation of microvoids and microcracks within the crystalline structure [34]. Eventually, these microvoids can grow large enough to be observed at the macroscopic or laboratory level. Alternatively, macroscopic models examine this phenomenon at the laboratory scale. In this setting, microscopic properties and microcracking are averaged over larger areas of material, which can be directly observed at the laboratory scale. This thesis will focus on macroscopic modeling, facilitating easier comparison with specific laboratory experiments and results.

Some macroscopic approaches concern themselves with identifying and following the path of cracks as they form in the material. This enables the identification of points of failure and crack propagation as the system evolves. Variational approaches [8, 9, 10] build global energy in the material using developing cracks as parameters. Calculus of variations is applied to minimize this resulting energy, yielding the path of any fissures. Network and fuse models consider a material as a collection of fuses and identify a crack by following the path of failed fuses as the system evolves [11, 12, 13, 14]. Other approaches aim specifically to address the computational complexity of fracture-mechanics simulations. Mesh-free approaches [23] and cohesive finite-element approaches [19, 20, 21, 22] actively divert computational resources away from “pristine” areas of materials and focus efforts near the region of the crack formation.

A more agnostic approach: phase field modeling has shown promise in dealing with pristine and fractured regions in a uniform and elegant way [1, 2, 3, 4, 5, 6, 7]. This approach uses a spatially and temporally varying field that designates and distinguishes cracks from undamaged regions. This field is a component interacting with other models, such as energetic models for temporal evolution. It is an additional unknown in the model, which evolves with the different material quantities. Following the evolution of this field, one can determine where fractures have occurred.

In any case, the material properties must be modeled a priori to obtain an accurate simulation. These material parameters vary spatially within the material. In general, getting precise measurements for these quantities at every point in a material may not be possible before performing a numerical simulation. Similarly, laboratory experiments [44, 45, 52, 53] show significant variability in experimental results from sample to sample. Other experiments [47, 49, 48, 50] show variability in the crystalline structure of various materials, and demonstrate correlations between the crystalline structure and the observed mechanical properties [51]. Consequentially, methods that model the random nature of material properties and their impact on experimental results have undergone significant research in recent decades [15, 16, 17, 18].

The random nature of materials and the resulting impact on observables in laboratory experiments require an accurate model for material response to capture this variability in order to make reliable predictions. To this end, methods from uncertainty quantification (UQ) have been studied in materials modeling contexts [27, 30, 31]. Furthermore, with the amount of data collected and simulated to examine such problems, methods used in big-data analysis have also seen attention [28, 29].

Keeping the idea of a laboratory experiment as a backdrop, we focus on measuring specific observables or quantities of interest regarding the mechanical system. Our goal is to simulate the kind of outputs one might expect from a laboratory experiment. For example, in the expanding ring experiment [45, 46], one might only be able to count the number of fragments generated from a ring shattering. This provides a consistent simulation output through which many experiments can be compared.

The models mentioned so far and that will be studied in this thesis have a common thread - they are all wrong. However, each may be wrong in different ways. They may have different computational complexities and be more or less accurate for specific quantities of interest. By combining outputs from multiple models, it may be possible to achieve better accuracy and precision than would be possible from any one model alone. In this way, we can think of a model as a forward map, \mathcal{F} , evaluating to a solution variable, u , that may depend on space and time. The input for this forward map is a random state variable, X , unique to the sample being examined. Then for each model and corresponding output, we can build an extractor, \mathcal{Q} , for the specific observable in question. In this way, given a collection of samples $X^{(1)}, X^{(2)}, \dots, X^{(N)}$, and a series of different models and corresponding extractors $(\mathcal{Q} \circ \mathcal{F})_1, (\mathcal{Q} \circ \mathcal{F})_2, \dots, (\mathcal{Q} \circ \mathcal{F})_m$, we can evaluate the specified observable Q for a multitude of models: $Q_\ell^{(j)} = (\mathcal{Q} \circ \mathcal{F})_\ell X_j$. Techniques in UQ can be applied to this dataset to understand the distribution of our observable and make predictions about the distribution of the observable in future simulations.

Moreover, UQ can separate the modeling, or epistemic uncertainty, from the random or aleatoric uncertainty. Studies like [65] discuss methods of separating these

uncertainties and quantifying the effect of each on the specified observables. Separating these effects makes it possible to generalize results from one model to another. In examples like [66], bounds can be constructed, giving rise to confidence intervals for observables under the assumptions of a different model. Beyond simple comparisons, multiple models can be combined, giving the resulting UQ results of a more optimal model than the constituent models, as in [69].

The main driver for the solution process will be the elastodynamics equation. To enable multiple models to be considered, we allow the dimension of the problem to depend on the intricacy of the model - namely, we can have a model which exists in \mathbb{R}^d where $d = 1, 2$, or 3 depending on if we want a one- two- or three- dimensional model. The elastodynamics model relies on quantifiable material properties - Young's modulus (or equivalently Bulk modulus), the density, and the Poisson ratio ν . While in general, these quantities can vary spatially within the material [15, 26, 40, 47, 64] for simplicity, we assume that all three of these quantities remain constant throughout the bulk of the material and the duration of the experiment.

Our goal in this thesis is to understand how to apply techniques in UQ to damage mechanics models for certain observables. To refine and achieve this goal, we start by rigorously defining the model we will use. First, we examine the problem of modeling quasi-brittle fracture [36]. Following the ideas presented in [43, 39, 34, 35], we construct a partial differential equation (PDE) model for damage propagation in various laboratory settings. We model crack formation and propagation using a damage variable, \mathcal{D} . The buildup of plastic deformations ultimately causes fissures to form, so these fissures can be identified by determining locations at which the damage variable exceeds a designated threshold. This damage variable is a phase field, enabling the PDE to remain unchanged even during material failure. This results in a more elegant and computationally simple simulation while maintaining similarities to laboratory settings. For the sake of simplicity, we assume the damage variable is a scalar, meaning failure modes are isotropic. A straightforward finite-element discretization is used to facilitate the numerical solution of this PDE and enables the PDE to be applied to

multiple geometries and forcing conditions.

Moreover, we enable this model to depend on given random fields governing material strength, which vary from sample to sample and vary spatially within each sample. These random fields will allow us to capture the same variability observed in laboratory experiments and seen in other numerical simulations. Chapter 2 discusses the damage mechanics model used here in more detail.

To better understand the implications of a random input for the PDE model and resulting observable values, Chapter 3 examines the specifics of spatially varying random fields and how to incorporate them into a PDE model. Since the quantities of interest computed from the PDE model are themselves functions of a random variable, thinking of these observables in the random-variable sense enables the calculation of distribution functions and other quantifiers of their distributions. These ideas are discussed in Chapter 4. In addition, Chapter 4 discusses uncertainty calculations, which allow the computations discussed to become robust against the randomness of the model.

Without an exact solution to the damage mechanics problem, the only way to determine the distribution of the observables is to sample their values by solving the model for multiple inputs. Two methods could be applied: polynomial chaos and Monte Carlo sampling. While polynomial chaos provides a more sophisticated procedure to estimate the resulting distributions of our observables, it is, in practice, difficult to use for this kind of problem because of the high dimensionality of the problem. Instead, Monte Carlo sampling uses brute force to compute the resulting observables for each input sample and then uses statistical analysis on the resulting distribution. The main drawback of Monte Carlo sampling techniques is the high number of samples required to obtain good approximations of the actual distribution. Chapter 5 discusses this in more detail and demonstrates some examples with specific geometries and quantities of interest.

Finally, Chapter 6 introduces both a way to alleviate the computation cost associated with standard Monte Carlo techniques and build a framework that can use

the outputs from multiple kinds of simulations to improve estimates of the actual distribution of an observable. Using techniques in Multilevel Monte Carlo, multi-fidelity analysis, and importance sampling, we can use outputs from multiple simulations to achieve better accuracy [68, 69, 70, 71, 73]. The proposed methodology includes the added benefit of being tunable. This means that the number of samples taken using each model framework is optimized to reduce the computational workload as much as possible and maintain required uncertainty levels. We examine these approaches for multiple observables and apply this idea to various mesh resolutions in a PDE context. We will also investigate the resulting output from different models for the same physical phenomenon.

Chapter 2

THE DAMAGE MECHANICS PROBLEM

2.1 Introduction

In this chapter, we discuss a specific damage mechanics model which will be used in this thesis. Ultimately, we want to understand the distribution of specific observables or quantities of interest (QoIs) resulting from a material fracture problem. We consider these QoIs to be dependent on random material properties and specific experimental configurations. The model discussed here will be the experiment, generating data for specified material input. From those results, QoIs can be computed in post-processing, enabling multiple QoIs to be measured for each experiment. Thus this chapter discusses building a solution from given material properties and experimental configuration.

This chapter will make use of a vector-tensor notation. A vector will be noted as \underline{u} , representing a physical vector such as displacement or position. A physical tensor will be represented as $\underline{\underline{\sigma}}$, which will be used for quantities such as strain or stress. The unit outward normal to a surface will be represented by \underline{n} . The dot, “.”, will be used to indicate a vector-dot product and will similarly work for tensors dotted with vectors such as $\|\underline{u}\|^2 = \underline{u} \cdot \underline{u}$ or

$$\underline{\underline{\sigma}} \cdot \underline{n} \quad \text{with} \quad (\underline{\underline{\sigma}} \cdot \underline{n})_i = \sum_{j=1}^d \sigma_{ij} n_j, \quad (2.1)$$

where σ_{ij} is the i, j component of the $\underline{\underline{\sigma}}$ tensor. The inner product between two tensors will be represented by $:$, such as

$$\underline{\underline{\varepsilon}} : \underline{\underline{\sigma}} = \sum_{i=1}^d \sum_{j=1}^d \varepsilon_{ij} \sigma_{ij}. \quad (2.2)$$

Finally, the operator ∇ will represent the gradient of a field, and $\nabla\psi$ will be a gradient vector,

$$(\nabla\psi)_i = \frac{\partial\psi}{\partial x_i}. \quad (2.3)$$

Where x_i is the i 'th component of the position vector, \underline{x} . Similarly, ∇ may be used to represent a tensor quantity through the gradient of a vector:

$$(\nabla\underline{u})_{ij} = \frac{\partial u_i}{\partial x_j}. \quad (2.4)$$

Additionally, $\nabla \cdot$ will represent the divergence operator, used as a scalar product as in

$$\nabla \cdot \underline{u} = \sum_{j=1}^d \frac{\partial u_j}{\partial x_j}, \quad (2.5)$$

or as the divergence of a tensor as in $\nabla \cdot \underline{\underline{\sigma}}$, resulting in a vector,

$$(\nabla \cdot \underline{\underline{\sigma}})_j = \sum_{i=1}^d \frac{\partial \sigma_{ij}}{\partial x_i}. \quad (2.6)$$

The superscript T will denote the transpose, and can be used for either vectors or tensors:

$$\|\underline{u}\|^2 = \underline{u}^T \underline{u}, \quad (\underline{\underline{\varepsilon}})_{ij}^T = \varepsilon_{ji}. \quad (2.7)$$

2.2 Elastodynamics Damage Mechanics Model

We base the damage mechanics model on the standard elastodynamics problem. The standard elastodynamics problem is a tensor-valued partial differential equation (PDE) modeling how a solid material deforms when subjected to external forces [37, 34]. It relates material displacement, \underline{u} , to a strain tensor, $\underline{\underline{\varepsilon}}$, and stress tensor, $\underline{\underline{\sigma}}$. By assumption, we will be examining a material at rest in its initial configuration, so the motion will only be introduced by external forces. The standard elastodynamics model reads

$$\frac{\partial^2}{\partial t^2}(\underline{u}) = \nabla \cdot \underline{\underline{\sigma}}, \quad \underline{x} \in \Omega, \quad (2.8)$$

$$\underline{\underline{\varepsilon}} = \frac{1}{2} \left(\nabla \underline{u} + (\nabla \underline{u})^T \right), \quad (2.9)$$

$$\underline{\underline{\sigma}} = \underline{\underline{\sigma}}[\underline{\underline{\varepsilon}}], \quad (2.10)$$

$$\underline{u} \Big|_{t=0} = 0, \quad \frac{\partial}{\partial t}(\underline{u}) \Big|_{t=0} = 0. \quad (2.11)$$

We use $\underline{\underline{\sigma}}[\cdot]$ to represent the stress computation based on the provided strain tensor. Most commonly, a linear relationship is used (see below). However, as damage and plastic deformations build up, this relationship can deviate from linearity. This thesis will consider materials that accrue damage while in the linear elasticity regime.

Depending on the geometry of the domain and forcing conditions, the boundary conditions of the problem can vary greatly. However, in general, the boundary conditions comprise a Dirichlet component on the displacement vector and a Neumann component specifying the surface stresses on portions of the domain. The boundary of the domain, $\partial\Omega$, can be split into two disjoint parts, Γ_D and Γ_N , corresponding to the Dirichlet and Neumann parts, respectively. The boundary conditions then read

$$\underline{u} \Big|_{\Gamma_D} = \underline{u}^{(D)}, \quad (2.12)$$

$$\underline{\underline{\sigma}} \cdot \underline{n} \Big|_{\Gamma_N} = \underline{g}^{(N)}, \quad (2.13)$$

$$\partial\Omega = \Gamma_D \cup \Gamma_N, \quad (2.14)$$

where \underline{n} represents the unit outward-normal to Ω .

The standard stress-strain relationship is a linear one. As mentioned above, this holds for materials before enough damage has built up to cause deviations from this relationship [39, 37]. The linear stress, represented as $\underline{\underline{\sigma}}^{(L)}$ is given by

$$\underline{\underline{\sigma}}^{(L)}[\underline{\underline{\varepsilon}}] = 2\mu\underline{\underline{\varepsilon}} + \lambda \operatorname{tr}(\underline{\underline{\varepsilon}})\underline{I}. \quad (2.15)$$

In (2.15), \underline{I} is the identity tensor, and tr is the trace operator. The Lamé parameters, λ , and μ are nondimensionalized parameters depending on the material's Poisson ratio. The second Lamé parameter, μ , is often referred to as the Shear-modulus. The Lamé parameters can be rewritten in terms of the Poisson ratio (ν) according to

$$\lambda = \frac{\nu}{(1 + \nu)(1 - 2\nu)}, \quad \mu = \frac{1}{2(1 + \nu)}. \quad (2.16)$$

As materials expand, plastic deformations build up and weaken the stress-strain relationship. This can be thought of as a strain-softening [39, 38, 7, 34], which modifies

the stress-strain relation causing deviations from linearity. Following the approach in [43, 32], we use a scalar damage field, \mathcal{D} , which modifies the stress-strain relationship and models the softening. Areas where $\mathcal{D} = 0$ correspond to pristine, undamaged material, while $\mathcal{D} = 1$ corresponds to a fully broken material that has failed. It is shown in [34] that in the isotropic case, the rate of damage formation is directly proportional to the rate of plastic strain formation. The proportionality variable encapsulates the thermodynamics of microvoid formation, which disrupts the pristine material lattice. Supposing the thermodynamics of the system remains fixed in time, then the damage variable is directly proportional to the total plastic strain the material has accrued. Therefore, the damage variable can be directly computed in some cases during laboratory experiments on real materials.

To determine the value of the damage variable throughout the simulation, we need to relate it back to the elastodynamics PDE. We follow a procedure similar to [43]. The damage variable enters the equation as a coefficient in the now nonlinear stress-strain relation. The stress-strain relation is then modified to read

$$\underline{\underline{\sigma}}[\underline{\underline{\varepsilon}}] = \underline{\underline{\sigma}} = (1 - \mathcal{D})\underline{\underline{\sigma}}^{(L)} = (1 - \mathcal{D})(2\mu\underline{\underline{\varepsilon}} + \lambda \text{tr}(\underline{\underline{\varepsilon}})\underline{\underline{I}}). \quad (2.17)$$

For the remainder of this thesis, we will use $\sigma^{(L)}$ to refer to the linear stress-strain relationship, and σ will refer to the relationship in equation (2.17).

Updates to the damage variable can be computed by comparing the material stress to a critical stress criterion, which describes the strength of the material. Once the material stresses exceed the critical stress, damage in the material begins to increase. In [43], this is done by comparing the Von Mises Equivalent stress, given in (2.18), to a critical yield stress, Σ . The Von Mises Equivalent stress can be written as

$$\sigma_{eq} := \sqrt{\frac{3}{2}\underline{\underline{s}} : \underline{\underline{s}}}, \quad \underline{\underline{s}} = \underline{\underline{\sigma}} - \frac{1}{3} \text{tr}(\underline{\underline{\sigma}})\underline{\underline{I}}. \quad (2.18)$$

Alternatively, the maximum principal stress (σ_{max}) can be used instead of the Von Mises Equivalent Stress. It can be shown that the maximum principal stress is

equal to the largest eigenvalue of the stress tensor:

$$\sigma_{max} = \max \Lambda(\underline{\underline{\sigma}}), \quad (2.19)$$

where Λ represents the collection of eigenvalues for a matrix.

In a truly brittle material [34], failure occurs whenever the Von Mises, or maximum principal stress, exceeds the critical stress. When the material fails, $\mathcal{D} = 1$, and the stress drops to zero. In this way, the stress-strain relation would read

$$\underline{\underline{\sigma}}^{(\text{brittle})}[\underline{\underline{\varepsilon}}; t] = \begin{cases} \underline{\underline{\sigma}}^{(L)} & \sigma_{max}(\underline{\underline{\varepsilon}}; s) < \Sigma \quad \forall s \leq t \\ \underline{\underline{0}} & \sigma_{max}(\underline{\underline{\varepsilon}}; s) \geq \Sigma \quad \text{for some } s \leq t \end{cases}. \quad (2.20)$$

However, such a relation poses difficulties mathematically due to the sudden jump in stress value past the critical stress. To avoid such jumps, we use a modified model that is piecewise-linear and continuous. As such, we call it a quasi-brittle model [24, 42, 43].

$$\underline{\underline{\sigma}}^{(\text{quasi-brittle})}[\underline{\underline{\varepsilon}}; t] = \begin{cases} \underline{\underline{\sigma}}^{(L)} & \sigma_{max}(\underline{\underline{\varepsilon}}; s) < \Sigma \quad \forall s \leq t \\ \frac{\Sigma}{\Delta\sigma} \cdot ((\Sigma + \Delta\sigma)\underline{\underline{I}} - \underline{\underline{\sigma}}^{(L)}(\underline{\underline{\varepsilon}}; s)) & \Sigma \leq \sup_{s \leq t} \sigma_{max}(\underline{\underline{\varepsilon}}; s) \leq \Sigma + \Delta\sigma \\ \underline{\underline{0}} & \Sigma + \Delta\sigma < \sup_{s \leq t} \sigma_{max}(\underline{\underline{\varepsilon}}; s) \end{cases}. \quad (2.21)$$

This new relationship is a piecewise linear stress-strain relationship, which exhibits linear elastic behavior below the ultimate yield stress of the material. There is then a stress-softening region of size $\Delta\sigma$ in which the material yields and exhibits plastic deformation. Beyond the stress softening region, the material has fractured, and the stress value drops to zero. As $\Delta\sigma \rightarrow 0$, the model gets closer to a true brittle model. A sketch of the quasi-brittle stress-strain relation can be seen in a sketch in Figure 2.1.

Using that $\underline{\underline{\sigma}}[\underline{\underline{\varepsilon}}] = (1 - \mathcal{D})\underline{\underline{\sigma}}^{(L)}$, it is then possible to determine the damage

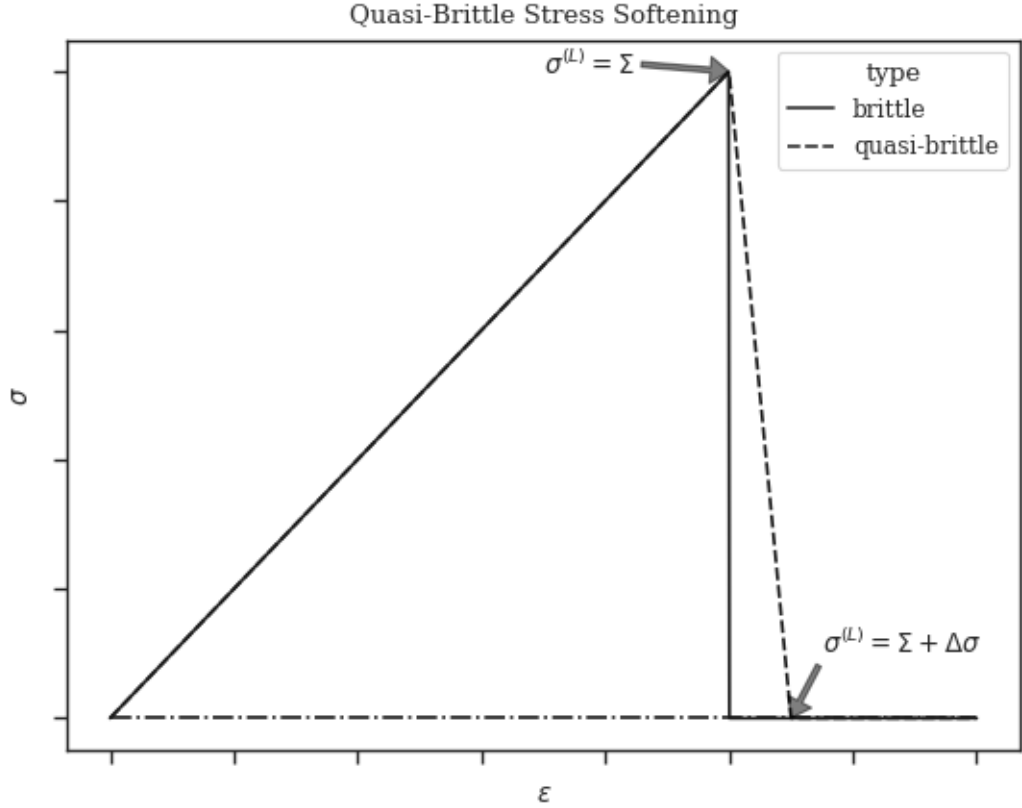


Figure 2.1: Comparison between stress-strain relations in brittle and quasi-brittle materials. A brittle material will exhibit a sudden drop in stress exactly at material failure. In contrast, a quasi-brittle material will exhibit a continuing drop in stress over a stress softening length, $\Delta\sigma$.

variable value from the maximum principal and yield stresses.

$$\mathcal{D}^{(\text{instant})}(\underline{x}, t) = \begin{cases} 0 & \sigma_{max}(\underline{\underline{\varepsilon}}(\underline{x}, s)) < \Sigma \quad \forall s \leq t \\ \frac{\Sigma + \Delta\sigma}{\Delta\sigma} \left(1 - \frac{\Sigma}{\sigma_{max}(\underline{\underline{\varepsilon}}(\underline{x}, s))} \right) & \Sigma \leq \sigma_{max}(\underline{\underline{\varepsilon}}(\underline{x}, s)) \leq \Sigma + \Delta\sigma \\ 1 & \Sigma + \Delta\sigma < \sigma_{max}(\underline{\underline{\varepsilon}}(\underline{x}, t)) \end{cases} \quad (2.22)$$

The above equation governs the behavior of the instantaneous damage. However, to incorporate a history dependence, we ensure damages are irreversible. Therefore, we

use

$$\mathcal{D}(\underline{x}, t) = \sup_{s \leq t} \mathcal{D}^{(\text{instant})}(\underline{x}, s). \quad (2.23)$$

An important observation is that in the regime of the stress-softening, the right-hand side of (2.8) is negative, indicating a negative stress-strain relationship. To ensure mathematical well-posedness, we employ Rayleigh damping parameters, modifying the elastodynamics equation by transforming it into a visco-elastic equation.

$$\frac{\partial^2}{\partial t^2} \underline{u} + \eta_1 \frac{\partial}{\partial t} \underline{u} - \eta_2 \frac{\partial}{\partial t} (\nabla \cdot \underline{\underline{\sigma}}^{(L)}) = \nabla \cdot \underline{\underline{\sigma}}, \quad 0 < \eta_1, \eta_2 \ll 1 \quad (2.24)$$

The Rayleigh damping parameters η_1, η_2 transform the equation into a damped hyperbolic equation in the linear stress-strain regime and avoid the equation turning elliptic through the stress-softening region.

For now, we will leave open the question of boundary conditions and the precise shape of the domain, Ω . We ultimately wish to run simulations in multiple configurations with various forcing conditions, so will leave this assignment for a later section.

The damage mechanics problem in full reads

$$\frac{\partial^2}{\partial t^2} \underline{u} + \eta_1 \frac{\partial}{\partial t} \underline{u} - \eta_2 \frac{\partial}{\partial t} (\nabla \cdot \underline{\underline{\sigma}}^{(L)}) = \nabla \cdot \underline{\underline{\sigma}}, \quad \underline{x} \in \Omega, t \in (0, t_{\max}), \quad (2.25)$$

$$\underline{\underline{\sigma}} = (1 - \mathcal{D}) \underline{\underline{\sigma}}^{(L)}, \quad (2.26)$$

$$\underline{\underline{\sigma}}^{(L)} = 2\mu \underline{\underline{\varepsilon}} + \lambda \text{tr}(\underline{\underline{\varepsilon}}) \underline{\underline{I}}, \quad (2.27)$$

$$\underline{\underline{\varepsilon}} = \frac{1}{2} (\nabla \underline{u} + (\nabla \underline{u})^T), \quad (2.28)$$

$$\mathcal{D}^{(\text{instant})} = \begin{cases} 0 & \sigma_{max} \leq \Sigma \\ \frac{\Sigma + \Delta\sigma}{\Delta\sigma} \left(1 - \frac{\Sigma}{\sigma_{max}}\right) & \Sigma < \sigma_{max} < \Sigma + \Delta\sigma, \\ 1 & \Sigma + \Delta\sigma \leq \sigma_{max} \end{cases} \quad (2.29)$$

$$\mathcal{D}(\underline{x}, t) = \sup_{s \leq t} \{ \mathcal{D}^{(\text{instant})}(\underline{x}, s) \}, \quad (2.30)$$

$$\underline{u} \Big|_{t=0} = \frac{\partial}{\partial t} \underline{u} \Big|_{t=0} = 0, \quad (2.31)$$

$$\underline{u} \Big|_{\Gamma_D} = \underline{u}^{(D)}, \quad \underline{\underline{\sigma}} \cdot \underline{n} \Big|_{\Gamma_N} = \underline{g}^{(N)}. \quad (2.32)$$

Once boundary conditions are assigned, equations (2.25) - (2.32) provide a mathematical framework to map the critical yield stress, Σ to a solution $(\underline{u}, \mathcal{D})$ for $(\underline{x}, t) \in \Omega \times [0, T]$.

2.2.1 1D problem and Well Posedness

An important concept in dealing with mathematical problems is the concept of well-posedness. For a mathematical problem to be well-posed, it must have a unique solution, and this solution must depend on input data in a continuous way. That is, small changes to the input data produce only small changes in the output. Due to the random nature of the damage mechanics problem, it is not clear that a unique solution exists, let alone that this solution depends on the critical yield stress in a continuous way.

In [32], we examined the one-dimensional analog of the damage mechanics problem to demonstrate well-posedness. Afterward, we examined some numerical examples to understand the impact of the critical yield stress field on the stress-strain curve. The one-dimensional analog of the problem described in (2.25) - (2.32) is

$$\frac{\partial^2 u}{\partial t^2} + \eta_1 \frac{\partial u}{\partial t} - \eta_2 \frac{\partial}{\partial t} \left(\frac{\partial^2 u}{\partial x^2} \right) = \frac{\partial}{\partial x} \left((1 - \mathcal{D}) \frac{\partial u}{\partial x} \right), \quad (x, t) \in (0, 1) \times (0, t_{\max}), \quad (2.33)$$

$$\mathcal{D}^{(\text{instant})} = \begin{cases} 0 & \frac{\partial u}{\partial x} \leq \Sigma \\ \frac{\Sigma + \Delta\sigma}{\Delta\sigma} \left(1 - \frac{\Sigma}{\frac{\partial u}{\partial x}} \right) & \Sigma < \frac{\partial u}{\partial x} < \Sigma + \Delta\sigma, \\ 1 & \Sigma + \Delta\sigma \leq \frac{\partial u}{\partial x} \end{cases} \quad (2.34)$$

$$\mathcal{D}(x, t) = \sup_{s \leq t} \{ \mathcal{D}^{(\text{instant})}(x, s) \}, \quad (2.35)$$

$$u \Big|_{t=0} = \frac{\partial u}{\partial t} \Big|_{t=0} = 0. \quad (2.36)$$

Again, we use an instantaneous damage variable to compute the damage for each time point and incorporate history dependence by ensuring damages are irreversible. In

[32], we examined the uniaxial strain version of this problem, in which the boundary conditions read

$$u \Big|_{x=0} = 0, \quad u \Big|_{x=1} = r(t). \quad (2.37)$$

To prove well-posedness, in our paper [32], we begin by reformulating the PDE problem into a semi-linear parabolic system with a random coefficient. To do so, we start by defining functions p and q by

$$p(x, t) = \int_0^x \frac{\partial u}{\partial t} - r'(t)y \, dy - \int_0^1 \int_0^x \frac{\partial u}{\partial t} - r'(t)y \, dy \, dx \quad (2.38)$$

$$q(x, t) = \eta_2 \cdot \left(\frac{\partial u}{\partial x} - r(t) \right) - p(x, t), \quad (2.39)$$

and let $z = (p, q)$. Then we can cast the 1D problem in (2.33) - (2.37) as

$$\frac{dz}{dt} + Az = f[z, r] + g(t) \quad t > 0, \quad (2.40)$$

with initial condition $z(x, 0) = z_0(x)$. The linear operator, A is defined by

$$A = \begin{bmatrix} \eta_1 I - \eta_2 \frac{\partial^2}{\partial x^2} & 0 \\ 0 & I \end{bmatrix}, \quad (2.41)$$

where I is the identity operator. For the nonlinear term, we introduce the stress operator acting on the displacement by $\sigma[u] = (1 - \mathcal{D}) \frac{\partial u}{\partial x}$, and define f by

$$f[z, r] = \begin{bmatrix} f_1(z, r) \\ q + \eta_1 p - f_1(z, r) \end{bmatrix}, \quad (2.42)$$

where

$$f_1(z, r) = \sigma[\eta_2^{-1}(p + q) + r] - \int_0^1 \sigma[\eta_2^{-1}(p + q) + r] \, dx. \quad (2.43)$$

Lastly, the rates of change of the boundary term are captured by the forcing term, $g(t)$, by

$$g(t) = \frac{1}{6}(\eta_1 r'(t) + r''(t)) \begin{bmatrix} 1 - 3x^2 \\ -(1 - 3x^2) \end{bmatrix}. \quad (2.44)$$

We define a space on which the solutions to (2.40) will exist. First, define the space X by

$$X = \left\{ (p, q) \in L^2(0, 1) \times C([0, 1]) : \int_0^1 p(x, t) dx = \int_0^1 q(x, t) dx = 0 \right\}. \quad (2.45)$$

The space X is equipped with the norm $\|(p, q)\|_X = \|p\|_{L^2} + \|q\|_C$. Then we take a subset $X^\alpha \subset X$. This space, $X^\alpha \subset H^{2\alpha}((0, 1)) \times C([0, 1])$, is equipped with the norm

$$\|\cdot\|_{X^\alpha} : (p, q) \mapsto \|A_1^\alpha p\|_{L^2} + \|q\|_C, \quad (2.46)$$

where $A_1^\alpha = (\eta_1 I - \eta_2 \partial_{xx})^\alpha$ for $\alpha \in (1/4, 1)$. The value of α tunes the regularity of the solutions. We extend the X^α norm through a maximum integration time, T , by

$$\|f\|_{X_T^\alpha} = \sup_{t \leq T} \|f(t)\|_{X^\alpha}, \quad (2.47)$$

which applies to functions $f \in C([0, T]; X^\alpha)$.

Since the yield stress, Σ is a random field, the instantaneous damage variable is a random variable over a probability space $(\Xi, \mathcal{B}, \mathbb{P})$. The instantaneous damage variable is thus a function of the form $\mathcal{D}^{(\text{instant})} = \mathcal{D}^{(\text{instant})}(\varepsilon, x; \xi)$, where ε is the 1D strain, x is the position and $\xi \in \Xi$ captures the randomness of the function. We further assume that $\mathcal{D}^{(\text{instant})}$ is Lipschitz continuous in ε , with Lipschitz constant $L_{\mathcal{D}}$, which is bounded above by a value $\bar{L}_{\mathcal{D}} < \infty$. This damage function then comes from a collection of admissible damage functions $\mathcal{A}_{\mathcal{D}}(\varepsilon_{max}, \bar{L}_{\mathcal{D}})$. The value of ε_{max} is related to the upper bound on the boundary condition, r .

The transformation of the 1D damage mechanics problem into the semilinear parabolic system (2.40) means that once well-posedness is proved for (2.40), the well-posedness result holds for (2.33) - (2.37). To show the well-posedness of the semilinear parabolic system, we make the following assumptions:

(A1) There is a $Z_0 > 0$, with $z_0 \in X^\alpha$ ($\alpha \in (1/4, 1)$) that has $\|z_0\|_{X^\alpha} \leq \frac{1}{2} \frac{Z_0}{a_0}$,

(A2) The boundary term, $r \in C^2(0, T_r)$ for some $T_r > 0$, and there is an ε_{max} with $\eta_2^{-1} \max\{c_\alpha, 1\} Z_0 + \|r\|_{C_{T_r}} < \varepsilon_{max}$,

$$(A3) \quad \mathcal{D}^{(\text{instant})} \in \mathcal{A}_{\mathcal{D}}(\varepsilon_{\max}, \bar{L}_{\mathcal{D}}),$$

$$(A4) \quad \eta_1 \leq \eta_1^{(0)} < \infty \text{ and } \eta_2 \leq \eta_2^{(0)} < \infty$$

The value of a_0 in (A1) comes from the boundedness of the semilinear operator A by

$$\|A^\theta e^{-tA}\| \leq a_\theta t^{-\theta}; \quad (2.48)$$

and the value of c_α in (A2) is the Sobolev embedding constant of $H^{2\alpha} \hookrightarrow C$.

Theorem 2.1. *Assume that (A1) - (A4) hold, and let $(\mathcal{D}^{(\text{instant})}, \bar{L}_{\mathcal{D}})$ be strongly \mathbb{P} -measurable and $\mathcal{D}^{(\text{instant})} \in \mathcal{A}_{\mathcal{D}}(\varepsilon_{\max}, \bar{L}_{\mathcal{D}})$ almost surely. Then there is a strongly \mathbb{P} -measurable mild solution $\xi \mapsto z(\xi) \in X_{T(\xi)}^\alpha$ of (2.40) with $T(\xi) > 0$ almost surely. In addition, this solution $z(\xi)$ is a strong solution for almost all $\xi \in \Xi$. Let*

$$u(x, t) = \int_0^x \eta_2^{-1}(p(y, t) + q(y, t)) + r(t) dy, \quad (2.49)$$

then u is a weak solution to the 1D damage mechanics PDE in (2.33).

Definition 2.1. *Let $z_0 \in X^\alpha$. A function $z \in C([0, T], X^\alpha)$ is a **mild solution** of the semilinear parabolic equation (2.40) provided it solves the integral equation*

$$z(t) = e^{-tA} z_0 + \int_0^t e^{-(t-s)A} (f(z, r)(s) + g(s)) ds, \quad 0 \leq t \leq T. \quad (2.50)$$

Definition 2.2. *For $z_0 \in X^\alpha$, the function*

$$z \in C([0, T]; X) \cap C([0, T]; X^\alpha) \cap C^1((0, T]; X) \cap C((0, T]; X^1), \quad (2.51)$$

is a **strong solution** if it satisfies (2.40) with equality holding in the X -norm sense for $0 < t \leq T$ and $z(0) = z_0$.

We rigorously proved this theorem in [32], but for convenience, the proof is summarized as follows. We show that for some time $T(\xi)$ that the mild solution z depends continuously on the instantaneous damage function and that $T(\xi) > 0$ almost surely. Next, we split the damage function and solution z into a series of simple

functions. By showing the resulting series are Cauchy, we can show their limits are strongly \mathbb{P} -measurable. Lastly, we show that a mild solution is also a strong solution of the semilinear problem. Then through a change of variables, we construct a weak solution to the 1D PDE.

In principle, the procedure we applied in [32] can be applied to the d -dimensional PDE, although this is technically involved. Performing this computation and verification, therefore, remains an open problem.

Having demonstrated well-posedness in the 1D case, in [32], we demonstrate numerical results for the stress-strain relationship over the time of the problem for various random fields. Define the mean stress over the domain of the problem as

$$\hat{\sigma}(t) = \int_0^1 \sigma(x, t) dx. \quad (2.52)$$

The mean stress can be plotted against the mean strain for each time:

$$\hat{\varepsilon}(t) = \int_0^1 \frac{\partial u}{\partial x} dx = r(t). \quad (2.53)$$

The random field used, Σ , is the 1-dimensional analog of the inverse-Helmholtz operator described in Chapter 3, see (3.43). Because of the dependence of this random field distribution on a correlation length parameter, ℓ , we examine how the stress-strain curve distribution changes for various values of ℓ . Figure 4 in [32] shows how the mean stress-strain curve remains relatively unchanged for multiple values of ℓ . Instead, what changes most is the variance of this stress-strain curve. For a modeled material, this random field may not be known exactly. Chapter 4 addresses how differences between the computed results and those results under an alternative model can be bounded, provided one knows the variance of the stress-strain curve and has a measure of the difference between the current and alternative models.

2.3 Numerical Solution of the Damage Mechanics Model

The damage mechanics problem described in (2.25) - (2.32) is discretized using a method of lines strategy in which spatial domains are discretized using finite elements,

and the resulting second-order time-dependent ordinary differential equation (ODE) system is solved forward in time using the Generalized- α method.

2.3.1 Semidiscretization via P1 Finite Elements

To illustrate this process, let \underline{v} be a test vector function in $\bigotimes_{k=1}^d H_{\Gamma_D}^1$, which is the space defined as

$$H_{\Gamma_D}^1 =: \left\{ f \in H^1(\Omega) : f \Big|_{\Gamma_D} = 0 \right\} \quad (2.54)$$

Integrating against the test function and casting the PDE into variational form, we obtain

$$\begin{aligned} \frac{d^2}{dt^2} \int_{\Omega} \underline{v} \cdot \underline{u} \, dx + \frac{d}{dt} \int_{\Omega} \eta_1 \underline{v} \cdot \underline{u} + \eta_2 (\nabla \underline{v}) : \underline{\underline{\sigma}}^{(L)}(\underline{u}) \, dx + \int_{\Omega} (1 - \mathcal{D})(\nabla \underline{v}) : \underline{\underline{\sigma}}^{(L)}(\underline{u}) \, dx = \\ \eta_2 \frac{d}{dt} \int_{\Gamma_N} \underline{v} \cdot \underline{g}^{(N)} \, ds + \int_{\Gamma_N} \underline{v} \cdot \underline{g}^{(N)} \, ds, \\ \text{subject to } \underline{u} \Big|_{\Gamma_D} = \underline{u}^{(D)}. \end{aligned} \quad (2.55)$$

Because the stress and strain tensors are symmetric, it is possible to rewrite the tensor inner products based on the strain of the test function rather than the gradient:

$$\begin{aligned} \frac{d^2}{dt^2} \int_{\Omega} \underline{v} \cdot \underline{u} \, dx + \frac{d}{dt} \int_{\Omega} \eta_1 \underline{v} \cdot \underline{u} + \eta_2 \underline{\underline{\varepsilon}}(\underline{v}) : \underline{\underline{\sigma}}^{(L)}(\underline{u}) \, dx + \int_{\Omega} (1 - \mathcal{D}) \underline{\underline{\varepsilon}}(\underline{v}) : \underline{\underline{\sigma}}^{(L)}(\underline{u}) \, dx = \\ \eta_2 \frac{d}{dt} \int_{\Gamma_N} \underline{v} \cdot \underline{g}^{(N)} \, ds + \int_{\Gamma_N} \underline{v} \cdot \underline{g}^{(N)} \, ds, \\ \text{subject to } \underline{u} \Big|_{\Gamma_D} = \underline{u}^{(D)}. \end{aligned} \quad (2.56)$$

Here we denote by the strain and linear stress operators

$$\underline{\underline{\varepsilon}}(\underline{v}) = \frac{1}{2} (\nabla \underline{v} + (\nabla \underline{v})^T), \quad (2.57)$$

$$\underline{\underline{\sigma}}^{(L)}(\underline{u}) = 2\mu \underline{\underline{\varepsilon}}(\underline{u}) + \lambda \text{tr}(\underline{\underline{\varepsilon}}(\underline{u})) \underline{I}. \quad (2.58)$$

The above variational form is discretized using $P1$ finite elements. Let $U \subset H_{\Gamma_D}^1$ be a finite-dimensional vector space whose elements consist of piecewise linear

functions. We consider the degrees of freedom defining U to be the values of a particular component of \underline{u} at the vertices from a triangular mesh over Ω . We define the vector function space $V = \bigotimes_{k=1}^d U$, which consists of stacked elements of U for the number of spatial dimensions of the physical problem. Let $\underline{\phi}_j \in V$ be the standard $P1$ FEM basis for V .

We also define the finite-dimensional $W \subset L^\infty(\Omega)$. This space is defined over the same triangulation used to define U above. The degrees of freedom defining W are averages over the constituent elements. This means the corresponding basis functions w_j are piecewise constant over the elements. This space W approximates the damage variable while V approximates the displacement field. We build the variational form in parts by converting each term in the weak formulation into its corresponding matrix. In this way, we build a mass, stiffness, and damping matrix according to

$$\text{Mass Matrix: } M \quad M_{ij} = \int_{\Omega} \underline{\phi}_i \cdot \underline{\phi}_j \, dx \quad (2.59)$$

$$\text{Damping Matrix: } C \quad C_{ij} = \eta_1 M_{ij} + \eta_2 K(0)_{ij} \quad (2.60)$$

$$\text{Stiffness Matrix: } K(\mathcal{D}) \quad K(\mathcal{D})_{ij} = \int_{\Omega} (1 - \mathcal{D}) \underline{\underline{\varepsilon}}(\underline{\phi}_i) : \underline{\underline{\sigma}}^{(L)}(\underline{\phi}_j) \, dx. \quad (2.61)$$

It should be noted that the damping matrix, C , does not depend on the value of \underline{u} since this term is linear with displacement. However, the stiffness matrix, K , does depend on displacement due to the nonlinearity introduced by the damage field. We have the right-hand side load vector to consider next. We assume η_2 is small enough that the load vector can be approximated by the second term on the right-hand side.

$$\text{Load Vector } \mathbf{b}(t) \quad b_i(t) = \int_{\Gamma_N} \underline{\phi}_i \cdot \underline{g}^{(N)}(\underline{x}, t) \, ds - \sum_{j=1}^N \int_{\Omega} \underline{\phi}_i \cdot \left(\underline{u}^{(D)}(\underline{x}_j, t) \odot \underline{\phi}_j \right) \, dx \quad (2.62)$$

Where the \odot represents element-wise vector multiplication. We can then represent the solution to the variational problem by a collection $(\underline{u}(\underline{x}, t), \mathcal{D}(\underline{x}, t)) \in V \times W$. Furthermore, we can write the displacement and damage as linear combinations of the

spanning functions for their respective spaces

$$\begin{aligned}\underline{\mathbf{u}}(\underline{\mathbf{x}}, t) &= \sum_{i=1}^{\dim V} \underline{\phi}_i(\underline{\mathbf{x}}) u_i(t), & \mathbf{u}(t)_i &:= u_i(t). \\ \mathcal{D}(\underline{\mathbf{x}}, t) &= \sum_{i=1}^{\dim W} w_i(\underline{\mathbf{x}}) \mathcal{D}_i(t), & \mathbf{d}(t)_i &:= \mathcal{D}_i(t).\end{aligned}\tag{2.63}$$

Thus for an unknown solution vector $\mathbf{u}(t)$, we can approximate the solution to the PDE with the solution to the ODE system given by

$$M \frac{d^2 \mathbf{u}}{dt^2} + C \frac{d\mathbf{u}}{dt} + K(\mathbf{d}) \mathbf{u} = \mathbf{b}(t),\tag{2.64}$$

where by $K(\mathbf{d})$ we indicate

$$K(\mathbf{d})_{ij} = \sum_{m=1}^{\dim(W)} \int_{\Omega} (1 - d_m w_m) \underline{\underline{\epsilon}}(\underline{\phi}_i) : \underline{\underline{\sigma}}^{(L)}(\underline{\phi}_j) dx.\tag{2.65}$$

The initial conditions, by the assumption of a system starting at rest and undamaged, are

$$\mathbf{u}(t=0) = \dot{\mathbf{u}}(t=0) = \mathbf{0}, \quad \mathbf{d}(t=0) = \mathbf{0}\tag{2.66}$$

The resulting ODE system is extremely stiff [54, 55, 56, 57], and as a result, explicit integration schemes can prove to be problematic. We opt instead for an implicit scheme. Numerical methods for equations of the form in (2.64) come up in structural dynamics, a common method for solving problems of the form of equation (2.64) is the Newmark- β method. More recently, improvements to the Newmark- β method have yielded the Generalized- α method.

Before discussing the integration methods used for (2.64), it is worth examining the construction for the nonlinear stiffness matrix, as this is a nonstandard FEM construction.

2.3.2 Quadratures for Finite Element Representation

The constructions of the finite element components, mass, stiffness, and damping matrices are handled using the FEniCS library for Python [75]. The mass and

damping matrices follow a standard procedure to generate, and so we will not discuss those in depth. Instead, we will focus our attention on the nonlinear stiffness matrix.

Let \mathcal{T} be a triangulation of the domain Ω . The integral of a finite element form, F , can thus be represented by summing its components on each element $T \in \mathcal{T}$.

$$\int_{\Omega} F dx = \sum_{T \in \mathcal{T}} \int_T F dx. \quad (2.67)$$

Let $\psi_i \in U$ be a collection of finite element basis functions for the scalar finite element space U . The $\underline{\phi}_i$ come from a tensor product of this scalar basis. Thus the quadratures used in (2.59) and (2.61) can be understood through the corresponding quadratures on the space U . In particular, let $\dim U$ be the dimension of U . Then $\dim V = d \cdot \dim U$ and

$$\underline{\phi}_i = \psi_{\text{floor}(i/d)} \underline{e}_{(i \bmod d)+1}, \quad (2.68)$$

where \underline{e}_1 is the unit vector in the x direction, \underline{e}_2 in the y , and so on.

Let $\hat{\psi}_k$ be a local finite element basis on the reference element, T_{ref} . There is an affine transformation $A_T : T_{\text{ref}} \rightarrow T$ for all $T \in \mathcal{T}$ such that

$$\psi_i \Big|_T = \hat{\psi}_k(A_T^{-1}(\underline{x})), \quad \text{for some } k. \quad (2.69)$$

Since the damage variable exists in a separate space, W , there is a mixed representation that must be handled. To this end, let $w_i \in W$ be a basis function for the damage variable over Ω . In addition, we will build the stiffness matrix using the function $\kappa = 1 - \mathcal{D}$. As with the displacement variable, we can represent this in terms of an affine transformation from a local basis function on the reference element.

$$w_i \Big|_T = \hat{w}_k(A_T^{-1}(\underline{x})) \quad \text{for some } k, \quad (2.70)$$

where \hat{w}_k is the local basis for the damage variable on the reference element. On the reference element, we can build a local stiffness tensor of the form

$$\hat{K}_{ijk} = \int_{T_{\text{ref}}} \hat{w}_k \hat{\psi}_i \hat{\psi}_j dx. \quad (2.71)$$

Then using the corresponding affine transformation, we can extract the corresponding component of \hat{K}_{ijk} to build the global stiffness matrix over every $T \in \mathcal{T}$. Let p be the degree of the quadrature in (2.71). For $p \leq 6$, hard-coded rules following the approximations in [78] are used to build the quadratures. For degrees larger than 6, these quadratures default to Gauss-Jacobi rules [76].

A special case is when \mathcal{D} is piecewise constant. In this case, there is only one \hat{w}_k and $\hat{w} \equiv 1$. Therefore the local stiffness tensor is a local stiffness matrix. The construction of the nonlinear stiffness matrix is then straightforward. The contribution to the stiffness matrix for every T is simply scaled by the average of $1 - \mathcal{D}$ over that particular element.

2.3.3 Modified Generalized- α method

The Generalized- α time stepping method is an extension of the Newmark- β method designed to solve second-order time-dependent ODEs of the form

$$\begin{aligned} M\ddot{\mathbf{u}} + C\dot{\mathbf{u}} + K\mathbf{u} &= \mathbf{f}, \quad t > 0 \\ \mathbf{u}(t=0) &= \mathbf{u}^{(0)}, \quad \dot{\mathbf{u}}(t=0) = \mathbf{v}^{(0)}. \end{aligned} \quad (2.72)$$

The Generalized- α method extends the Newmark- β method by applying a weighted average in the new and old solutions in the primary ODE [54]. Each time step forward is computed by solving the system

$$M\mathbf{a}^{(n+1-\alpha_m)} + C\mathbf{v}^{(n+1-\alpha_f)} + K\mathbf{u}^{(n+1-\alpha_f)} = \mathbf{f}^{(n+1-\alpha_f)}, \quad (2.73)$$

subject to the constraints

$$\begin{aligned} \mathbf{u}^{(n+1)} &= \mathbf{u}^{(n)} + \Delta t \mathbf{v}^{(n)} + \frac{\Delta t^2}{2} ((1 - 2\beta)\mathbf{a}^{(n)} + 2\beta\mathbf{a}^{(n+1)}), \\ \mathbf{v}^{(n+1)} &= \mathbf{v}^{(n)} + \Delta t ((1 - \gamma)\mathbf{a}^{(n)} + \gamma\mathbf{a}^{(n+1)}). \end{aligned} \quad (2.74)$$

The field $\mathbf{g}^{(n+1-\alpha)}$ for a time-dependent vector \mathbf{g} represents a weighted average of $\mathbf{g}^{(n+1)}$ and $\mathbf{g}^{(n)}$ of the form

$$\mathbf{g}^{(n+1-\alpha)} = \alpha\mathbf{g}^{(n)} + (1 - \alpha)\mathbf{g}^{(n+1)}. \quad (2.75)$$

The time stepping parameters for the Generalized- α method β , γ , and Δt are shared with that of Newmark- β . The weightings $\alpha_m, \alpha_f \in [0, 1)$ represent the time delay weightings of the acceleration and forcing terms, respectively. The Generalized- α method can be expressed in a block structure as

$$\mathbb{A}^{(n+1)}\mathbf{U}^{(n+1)} = \mathbb{F}^{(n)}\mathbf{U}^{(n)} + \mathbf{G}^{(n+1)}, \quad (2.76)$$

where the matrices \mathbb{A} and \mathbb{F} are defined by

$$\mathbb{A}^{(n+1)} = \begin{bmatrix} (1 - \alpha_f)K^{(n+1)} & (1 - \alpha_f)C & (1 - \alpha_m)M \\ I & 0 & -\beta\Delta t^2 I \\ 0 & I & -\gamma\Delta t I \end{bmatrix}, \quad (2.77)$$

and

$$\mathbb{F}^{(n)} = \begin{bmatrix} -\alpha_m M & -\alpha_f C & -\alpha_f K^{(n)} \\ I & \Delta t & \frac{(1 - 2\beta)}{2} \Delta t^2 I \\ 0 & I & (1 - \gamma)\Delta t I \end{bmatrix}. \quad (2.78)$$

The vectors $\mathbf{U}^{(n)}$ and $\mathbf{G}^{(n+1)}$ are defined as

$$\mathbf{U}^{(n)} = \begin{bmatrix} \mathbf{u}^{(n)} \\ \mathbf{v}^{(n)} \\ \mathbf{a}^{(n)} \end{bmatrix}, \quad \mathbf{G}^{(n+1)} = \begin{bmatrix} (1 - \alpha_f)\mathbf{f}^{(n+1)} + \alpha_f\mathbf{f}^{(n)} \\ \mathbf{0} \\ \mathbf{0} \end{bmatrix}. \quad (2.79)$$

In the above equations, we denote

$$K^{(n)} = K(\mathbf{d}^{(n)}). \quad (2.80)$$

Note that in the case $\alpha_m = \alpha_f = 0$, the Generalized- α method reverts back to the Newmark- β method.

Since the stiffness matrix depends on the current damage value, which depends on the current displacement field, the standard Generalized- α method would require solving a highly nonlinear problem at each time step. To avoid the incurred computational complexity caused by this, we modify the method so that the damage is effectively delayed during the time solution step:

$$\mathbb{A}^{(n)}\mathbf{U}^{(n+1)} = \mathbb{F}^{(n)}\mathbf{U}^{(n)} + \mathbf{G}^{(n+1)}. \quad (2.81)$$

Once we determine $\mathbf{u}^{(n+1)}$, we use that value to determine the corresponding $\mathbf{d}^{(n+1)}$ according to the damage mechanics described by (2.29) and (2.30). By doing so, we produce more local truncation error since we are no longer solving the exact system described in the Generalized- α method. However, we make the problem much more computationally feasible. The basic time evolution can then be thought of as a splitting method $(\mathbf{u}^{(n)}, \mathbf{d}^{(n)}) \rightarrow (\mathbf{u}^{(n+1)}, \mathbf{d}^{(n)}) \rightarrow (\mathbf{u}^{(n+1)}, \mathbf{d}^{(n+1)})$.

In the case of Dirichlet boundary conditions on the displacement, boundary conditions on the velocity and acceleration can be precomputed and added to the system in (2.76). However, if one wishes to avoid this safely, the forms of $\mathbf{v}^{(n+1)}$ and $\mathbf{a}^{(n+1)}$ can be substituted in terms of $\mathbf{u}^{(n+1)}$ as in (2.74). Those known terms can be moved to the right-hand side, leaving behind a system in which only $\mathbf{u}^{(n+1)}$ needs to be solved.

2.3.4 Verification of Orders of Accuracy

To verify our numerical implementation, we examine the numerical convergence of our methods with increasing refinement. For this, we consider unit square for the domain, with stress-free (zero Neumann) boundary conditions at the top and bottom. The left boundary is fixed in position (Dirichlet zero), and the right boundary is pulled at a constant expansion speed. The boundary conditions can be summarized below

$$\Omega = (0, 1) \times (0, 1) \ni (x, y) = \underline{x}; \quad (2.82)$$

$$\underline{\underline{\sigma}} \cdot \underline{\underline{n}} = \underline{\underline{0}}, \quad y = 0, 1; \quad (2.83)$$

$$\underline{\underline{u}} = \underline{\underline{0}}, \quad x = 0; \quad \underline{\underline{u}} = ct\underline{\underline{e}}_x, \quad x = 1. \quad (2.84)$$

The value c is a fixed expansion speed, t is time, and $\underline{\underline{e}}_x$ is the unit vector in the x direction. Figure 2.2 illustrates the L^2 convergence error of the displacement field. It can be seen from Figure 2.2 that this displacement field error is second-order accurate.

Next, we consider the convergence of the numerical scheme in t . Because we are using a modified Generalized- α method, we need to examine the convergence while

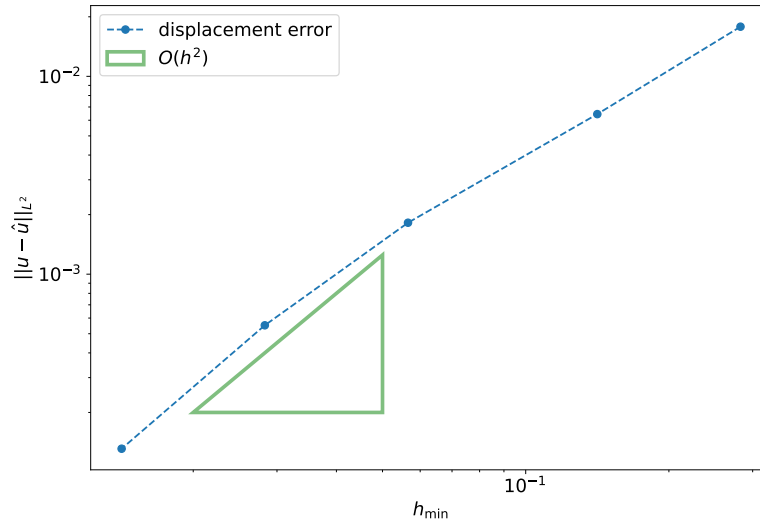


Figure 2.2: Spatial convergence results for the linear elastodynamics problem (damage fixed at zero) at the final time step. Mesh resolution is measured based on the minimum cell diameter, and the resulting system exhibits second-order convergence as expected by a $P1$ FEM scheme.

allowing damages. To this end, we use a fixed field for Σ , defined by

$$\Sigma = 1 - \frac{1}{2} \exp\left(-\frac{\|4(\underline{x} - (0.5, 0.5))\|^2}{2}\right). \quad (2.85)$$

This critical stress field exhibits a dip to 0.5 in the center of the domain. Again, we compare the errors at the final time step, and the reference solution is taken as the solution using the smallest value of Δt ($\Delta t = 1/300$). We are able to observe convergence in displacement as being second-order. Moreover, because nonzero damages are produced, we can also examine the convergence of this variable. It can be seen that both the damage and displacement variables exhibit second-order convergence. Those results can be seen in Figure 2.3.

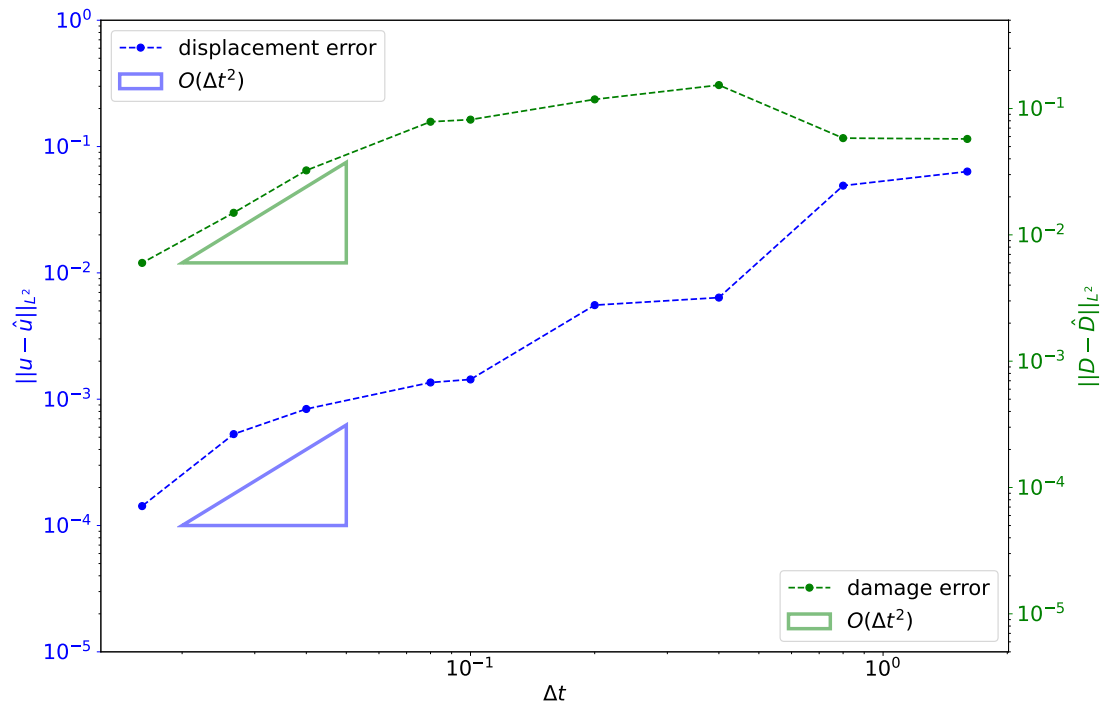


Figure 2.3: Temporal convergence results for the nonlinear damage mechanics problem using a fixed spatial mesh discretization. Displacement (in blue) and damage (in green) can be seen to be second-order convergent in Δt .

Chapter 3

RANDOM FIELDS

3.1 Introduction and Notation

A key feature of the damage mechanics problem is the unpredictability of when and where fracture will occur. Different samples of material have differing distributions of defects. To model this fact, we will approximate the defects of the material using a random field [43, 62]. Additionally, we can tune specific characteristics of the desired field by examining the parameters governing the underlying distribution of the field.

To understand a random field, we need a framework that allows us to interpret its meaning and enables computations and evaluations of the random field. We begin by defining a probability space for a random variable [59].

Definition 3.1. A *probability space* is a triplet $(\Xi, \mathcal{F}, \mathbb{P})$ consisting of a set Ξ of outcomes, a σ -field over Ξ of events, \mathcal{F} , and a probability measure \mathbb{P} on Ξ .

Generally, the set Ξ is used for a hidden variable ξ , which cannot be directly observed. In this way, a random variable, X , is considered a real-valued, measurable function of the unobservable variable ξ : $X(\xi)$. The randomness can then be understood as the inability to observe the value of ξ . In practice, we often do not explicitly refer to Ξ or to \mathcal{F} and instead rely on the distribution function of X through its pre-image.

Definition 3.2. Let X be a random variable on probability space $(\Xi, \mathcal{F}, \mathbb{P})$, and let \mathcal{X} be the range of X or all possible values for X . The **distribution function** of X is a function P that, for every $B \subset \mathcal{X}$ has

$$P(B) = \mathbb{P}(X^{-1}(B)) = \mathbb{P}\{\xi \in \Xi : X(\xi) \in B\}. \quad (3.1)$$

It should be noted that because of the equivalence between P acting on \mathcal{X} and \mathbb{P} acting on Ξ , P itself is a probability measure. We will refer to P as the probability measure of a random variable X , skipping all references to the underlying probability space $(\Xi, \mathcal{F}, \mathbb{P})$.

Finally, we can differentiate between discrete and continuous random variables based on their ranges.

Definition 3.3. A *discrete* random variable X has a range \mathcal{X} that is isomorphic to a subset of \mathbb{N} . That is, it takes on either finitely or countably many states. For each element $x \in \mathcal{X}$, the **probability mass function** of X is given by

$$m(x) := P(\{x\}), \quad \text{and} \quad \sum_{x \in \mathcal{X}} m(x) = P(\mathcal{X}) = 1. \quad (3.2)$$

A *continuous* random variable Y has a range \mathcal{Y} , which is isomorphic to a subset of \mathbb{R}^d and has an uncountable number of states.

3.2 Univariate Random Variables

The standard case of random variables is a single variable, X , which can be continuous or discrete. Each sample of this random variable is a scalar and takes on a single value. As mentioned above, a discrete random variable can be identified with its probability mass function (PMF). On the other hand, a continuous random variable Y has a range \mathcal{Y} that is isomorphic to a subset of \mathbb{R} , so it can take on uncountably many states. In cases of a continuous random variable, for this thesis, we will only be considering random variables whose probability measures are absolutely continuous with respect to the Lebesgue measure.

Definition 3.4. A measure ν on a set Ω is **absolutely continuous** with respect to another measure, μ , if

$$\mu(A) = 0 \implies \nu(A) = 0. \quad (3.3)$$

For all $A \subset \Omega$. We write $\nu \ll \mu$ to indicate ν is absolutely continuous with respect to μ . This property is equivalent to the existence of a Radon-Nikodym derivative, g , a μ -measurable function, with

$$\nu(A) = \int_A g d\mu. \quad (3.4)$$

Definition 3.5. The **probability density function (PDF)** of a continuous random variable X is the Radon-Nikodym derivative of its distribution function with respect to the Lebesgue measure, that is, the PDF of X , ρ , has

$$P(A) = \int_A \rho(x) dx, \quad \forall A \subset \mathcal{X}. \quad (3.5)$$

We will use several continuous random variables extensively in this thesis, each defined by their own PDFs.

Univariate Gaussian Random Variables

For a Gaussian random variable with mean μ and standard deviation σ , its PDF is given by

$$\rho(x; \mu, \sigma) = \frac{1}{\sigma\sqrt{2\pi}} e^{-\frac{(x-\mu)^2}{2\sigma^2}}. \quad (3.6)$$

A Gaussian random variable is often also called a normally-distributed random variable. We write this distribution as $\mathcal{N}(\mu, \sigma^2)$ to represent a normally distributed random variable with mean μ and variance σ^2 .

Univariate Log-Normal Random Variable

A scalar log-normal random variable Y has $\log(Y) \sim \mathcal{N}(\mu, \sigma^2)$, that is, Y is the pointwise exponential of a Gaussian random variable. It has a PDF given by

$$\rho(y; \mu, \sigma) = \begin{cases} \frac{1}{y\sigma\sqrt{2\pi}} \exp\left(-\frac{(\log y - \mu)^2}{2\sigma^2}\right) & y > 0 \\ 0 & y \leq 0 \end{cases}. \quad (3.7)$$

Univariate Weibull Random Variable

A scalar Weibull random variable W has PDF given by

$$\rho(x; \lambda, \kappa) = \begin{cases} \frac{\kappa}{\lambda} \left(\frac{x}{\lambda}\right)^{\kappa-1} e^{-(x/\lambda)^\kappa} & x \geq 0 \\ 0 & x < 0 \end{cases}. \quad (3.8)$$

The shape parameter, κ , dictates the shape of the distribution's tails, and λ acts as a scaling on x .

3.3 Vector Valued Random Variables

In building random fields, the next step is to construct a random vector. Given a collection of N random variables, X_1, X_2, \dots, X_N , defined over the same probability space, we can define the random vector as $\mathbf{X} = (X_1, X_2, \dots, X_N)^T$. We can then identify this vector-valued random variable with its own probability space: $(\tilde{\Xi}, \tilde{\mathcal{F}}, \tilde{\mathbb{P}})$. Similarly, we can evaluate either its probability mass function or probability density function as appropriate depending on whether the X_j are continuous or discrete.

In general, it may be possible to gain information regarding the distribution of X_j , given information on X_k , for some j and k . We discuss the joint distribution of two random variables, X and Y .

Definition 3.6. *The **joint distribution** of random variables X and Y is*

$$P_{XY}(A, B) = \mathbb{P}\{\xi \in \Xi : X(\xi) \in A \text{ and } Y(\xi) \in B\}. \quad (3.9)$$

We will write $\mathbb{P}(X \in A, Y \in B)$ to describe the probability that X is in A and Y is in B . The lack of either “and” or “or” will default to the “and” case, i.e., $X \in A, Y \in B$ is read $X \in A$ and $Y \in B$.

Similarly, we can define the conditional probability of $X \in A$ given that $Y \in B$:

$$\mathbb{P}(X \in A | Y \in B) = \begin{cases} \frac{\mathbb{P}(X \in A, Y \in B)}{\mathbb{P}(Y \in B)}, & \mathbb{P}(Y \in B) > 0 \\ 0 & \mathbb{P}(Y \in B) = 0 \end{cases} \quad (3.10)$$

In addition, this can be converted to the conditional distribution of X , given a priori information about Y .

$$P_{X|Y \in B}(A) = \mathbb{P}(X \in A | Y \in B). \quad (3.11)$$

Definition 3.7. *Two random variables, X and Y are **independent** if*

$$\mathbb{P}(X \in A | Y \in B) = \mathbb{P}(X \in A) \quad \text{for every } A, B. \quad (3.12)$$

*We say X and Y are **independent and identically distributed (i.i.d.)** if X and Y are independent and have the same distribution function.*

3.4 Random Fields

Definition 3.8. *Let $(\Xi, \mathcal{F}, \mathbb{P})$ be a probability space, and let Ω be a topological space. For all $x \in \Omega$, let $Z(x)$ be a random variable on the probability space $(\Xi, \mathcal{F}, \mathbb{P})$, taking values in \mathcal{Z} . Then the collection $\{Z(x) : x \in \Omega\}$ is a **\mathcal{Z} -valued random field** on Ω .*

Generating samples from a random field can pose a challenge. In particular, this thesis concerns random fields which exist inside a Hilbert space, \mathcal{H} over a domain $\Omega \subset \mathbb{R}^d$. In general, we can define a random Gaussian field over \mathcal{H} . Then non-Gaussian fields can be generated via a transformation of a Gaussian random field [61].

Definition 3.9. *A **Gaussian field**, Y , on a domain $\Omega \subset \mathbb{R}^d$ has for all $x_1, x_2, \dots, x_n \in \Omega$ that the random vector $(Y(x_1), Y(x_2), \dots, Y(x_n))$ is a multivariate normal random variable.*

Definition 3.10. *A **multivariate normal random variable \mathbf{X}** is a collection of Gaussian random variables (X_1, X_2, \dots, X_N) , that can be described by a mean vector, $\boldsymbol{\mu} \in \mathbb{R}^N$ and covariance matrix $\Sigma \in \mathbb{R}^{N \times N}$, given by*

$$\mu_i = \mathbb{E}[X_i] \quad (3.13)$$

$$\Sigma_{ij} = \text{Cov}[X_i, X_j] =: \mathbb{E}[(X_i - \mathbb{E}[X_i])(X_j - \mathbb{E}[X_j])]. \quad (3.14)$$

Where $\text{Cov}[\cdot, \cdot]$ represents the covariance between two random variables (note that $\text{Cov}[X, X] = \text{Var}[X]$). Furthermore, the probability density function of such a random vector is given by

$$\frac{1}{(2\pi)^{N/2} \sqrt{\det \Sigma}} \exp\left(-\frac{1}{2}(\mathbf{x} - \boldsymbol{\mu})^T \Sigma^{-1}(\mathbf{x} - \boldsymbol{\mu})\right), \quad (3.15)$$

provided that Σ has full rank. To indicate \mathbf{X} is a Gaussian vector with mean $\boldsymbol{\mu}$ and covariance matrix Σ , we will write $\mathbf{X} \sim \mathcal{N}(\boldsymbol{\mu}, \Sigma)$.

The above definition for a Gaussian field admits a representation for Y with a mean function, $\mu \in \mathcal{H}$, and covariance function k .

Definition 3.11. Let \mathcal{H} be a Hilbert space. Let Y be an \mathcal{H} -valued Random Gaussian field on Ω . The **mean** of Y is defined by

$$\mu(x) = \mathbb{E}[Y(x)]. \quad (3.16)$$

The **covariance function** or **covariance kernel** of Y is defined by

$$k(x, y) = \text{Cov}[Y(x), Y(y)]. \quad (3.17)$$

Note that by construction

1. k is symmetric: $k(x, y) = k(y, x)$
2. k is positive semi-definite: $k(x, x) \geq 0$ for all $x \in \Omega$

In addition, we define the **covariance operator** by

$$\mathcal{C} : \mathcal{H} \rightarrow \mathcal{H} \quad (3.18)$$

$$\mathcal{C}f = \int_{\Omega} k(x, y)f(y) dy. \quad (3.19)$$

The Gaussian field Y with mean μ and covariance operator \mathcal{C} is written as $Y \sim \mathcal{N}(\mu(x), \mathcal{C})$. In particular, this random field Y introduces a Gaussian measure γ onto the Hilbert space \mathcal{H} . To generate samples of Y , we can rely on the nature of the

Hilbert space \mathcal{H} , admitting an orthogonal basis. By writing Y as a sum of these basis functions, one can generate samples for Y .

Alternatively, the Karhunen-Loève Expansion (KLE) provides a mechanism to sample from a random field based on a decomposition of the covariance operator [60, 63]. To do so, consider the eigenvalue problem for the linear operator \mathcal{C} :

$$\mathcal{C}\phi = \lambda\phi. \quad (3.20)$$

As the covariance kernel k is symmetric, \mathcal{C} is self-adjoint. Consequentially the eigenfunctions can be shown to be orthogonal. The KLE for a random field $Y \sim \mathcal{N}(\mu, \mathcal{C})$ rewrites Y as a series of the form:

$$Y(x) = \mu(x) + \sum_{n=1}^{\infty} Z_n \sqrt{\lambda_n} \phi_n(x). \quad (3.21)$$

Where the $Z_n \sim \mathcal{N}(0, 1)$ are i.i.d. univariate standard normal random variables and the eigenfunctions are scaled as to have $\|\phi_n\|_{L^2(\Omega)} = 1$. It can also be shown that the λ_k are non-negative. Provided the eigenvalues, λ_n are sorted so that $\lambda_n \geq \lambda_{n+1}$ for all n , then this sum can be truncated to make it computationally feasible:

$$Y \approx \tilde{Y} = \mu(x) + \sum_{n=1}^N Z_n \sqrt{\lambda_n} \phi_n(x). \quad (3.22)$$

In this way, the KLE provides a framework for associating a random Gaussian vector: $\mathbf{Z} \sim \mathcal{N}(\mathbf{0}, I)$ with a random Gaussian field $Y(x)$. One can also bound the error resulting from this truncation by

$$\left\| Y - \tilde{Y} \right\|_{L^2(\Omega)}^2 = \sum_{n=N+1}^{\infty} Z_n^2 \lambda_n. \quad (3.23)$$

This error is a random variable and still requires an infinite number of the Z_n to be realized. However, taking the expectation value of this quantity yields

$$\mathbb{E} \left[\left\| Y - \tilde{Y} \right\|_{L^2(\Omega)}^2 \right] = \sum_{n=N+1}^{\infty} \lambda_n. \quad (3.24)$$

3.5 Computing the Eigendecomposition of the Covariance Operator

The choice of covariance kernel, k , determines the operator \mathcal{C} . In general, it may be difficult to compute an exact eigendecomposition for \mathcal{C} given an arbitrary kernel. One approach is to generate a numerical approximation to the eigendecomposition.

3.5.1 Numerical Eigendecomposition

Let Y be an \mathcal{H} -valued Gaussian field over Ω . In the problem description discussed in Chapter 2, the damage variable exists on a finite-dimensional subspace of a Hilbert space. Let this subspace be W . As a result, we only need to determine an approximation to Y on this subspace W . To this end, we consider building samples for the projected random variable: $\text{Proj}_W Y$.

Applying this to the KLE in (3.21), gives

$$\text{Proj}_W Y = \text{Proj}_W \mu + \sum_{n=1}^{\infty} Z_n \sqrt{\lambda_n} \text{Proj}_W \phi_n. \quad (3.25)$$

And applying the projection to (3.20), we see

$$\lambda_n \text{Proj}_W \phi_n = \text{Proj}_W (\mathcal{C} \phi_n). \quad (3.26)$$

Enforcing this be an eigenvalue problem on W , we can let $\psi = \text{Proj}_W \phi_n$, giving

$$\lambda_n \psi = \text{Proj}_W (\mathcal{C} \psi). \quad (3.27)$$

Proposition 3.1. *Let $\Omega \subset \mathbb{R}^d$ be a bounded set, and let \mathcal{H} be a Hilbert space on Ω . Let W be a finite-dimensional subspace of \mathcal{H} , with basis functions w_j for $j = 1, 2, \dots, \dim W$. The eigenvalue problem*

$$\text{Proj}_W (\mathcal{C} \psi) = \lambda \psi, \quad \psi \in W, \quad (3.28)$$

where

$$\mathcal{C} \psi = \int_{\Omega} k(x, y) \psi(y) dy, \quad (3.29)$$

can be solved numerically by

$$MCM\mathbf{a} = \lambda M\mathbf{a}. \quad (3.30)$$

Where

$$\psi = \sum_{j=1}^{\dim W} a_j w_j(x), \quad (3.31)$$

$$M_{ij} = \langle w_i, w_j \rangle_{L^2(\Omega)}, \quad (3.32)$$

$$C_{ij} = \int_{\Omega} \int_{\Omega} w_i(x) w_j(y) k(x, y) dx dy. \quad (3.33)$$

Proof. As $\psi \in W$, we can write

$$\psi(x) = \sum_{j=1}^{\dim W} a_j w_j(x). \quad (3.34)$$

Since (3.28) only holds in the weak sense on W , casting to weak form yields

$$\langle w_i, \text{Proj}_W(\mathcal{C}\psi) \rangle_{L^2(\Omega)} = \lambda \sum_{j=1}^{\dim W} a_j \langle w_i, w_j \rangle_{L^2(\Omega)}, \quad i = 1, 2, \dots, \dim W. \quad (3.35)$$

In the above equation, we see the right-hand-side of (3.30) by the terms in the mass matrix, M .

For the left-hand side, consider the projection operator. This operator is such that for any ϕ

$$\langle w_i, \phi - \text{Proj}_W \phi \rangle_{L^2(\Omega)} = 0. \quad (3.36)$$

Therefore we have

$$\langle w_i, \text{Proj}_W(\mathcal{C}\psi) \rangle_{L^2(\Omega)} = \langle w_i, \mathcal{C}\psi \rangle_{L^2(\Omega)}. \quad (3.37)$$

Expanding this using the form of ψ gives

$$\langle w_i, \mathcal{C}\psi \rangle_{L^2(\Omega)} = \sum_{j=1}^{\dim W} a_j \langle w_i, \mathcal{C}w_j \rangle_{L^2(\Omega)}. \quad (3.38)$$

Recalling the form of \mathcal{C} , the above inner product may be expanded to

$$\langle w_i, \mathcal{C}w_j \rangle_{L^2(\Omega)} = \int_{\Omega} \int_{\Omega} k(x, y) w_i(x) w_j(y) dy dx. \quad (3.39)$$

To examine the values of k in this finite element representation, we need to approximate k onto the collection of basis functions w_i . To this end, we can write

$$k(x, y) \approx \sum_{k=1}^{\dim W} \sum_{m=1}^{\dim W} C_{km} w_k(x) w_m(y). \quad (3.40)$$

Which gives that

$$\langle w_i, \mathcal{C}w_j \rangle_{L^2(\Omega)} = \sum_{k=1}^{\dim W} \sum_{m=1}^{\dim W} M_{ik} C_{km} M_{mj}. \quad (3.41)$$

It remains to demonstrate the form of C . Building the projection of k onto the space $W \times W$, we can see

$$C_{ij} = \int_{\Omega} \int_{\Omega} w_i(x) k(x, y) w_j(y) dy dx. \quad (3.42)$$

□

The finite-dimensional representation of the problem deals with the problem of an infinite sum directly, as the problem is reduced to a finite-dimensional linear-algebra system. The resultant eigenvectors, \mathbf{a} , can be scaled so that the L^2 -norms of the resulting eigenfunctions have values of 1.

As an alternative to computing a numerical decomposition, clever choices of k (and therefore \mathcal{C}) can admit relatively simple solutions to the eigenvalue problem (3.20). Doing so enables an exact expansion in the KLE.

3.5.2 Examples of Covariance Operators

We consider a covariance operator that will be used for several of the examples discussed in later sections. In particular, we examine an operator of the form

$$\mathcal{C} = \alpha^2 \left(-\Delta + \frac{1}{\ell^2} \right)^{-r}, \quad \text{on } H_{\text{per}}^1((0, 1) \times (0, 1)). \quad (3.43)$$

Here H_{per}^1 denotes the subspace of H^1 with periodic boundary conditions. The parameter r tunes the regularity of the resulting field. For the problems discussed in Chapters 5 and 6, we will use $r = 1$.

It should be noted that in this case, the aforementioned operator is not trace class [80]. This holds for 2D and higher, but the operator is trace class when restricted to 1D. As a result, using this as the covariance operator for a 2D Gaussian field poses a problem. In the following example, we show how this operator can be decomposed using its eigenexpansion. By truncating this expansion, we construct a finite-dimensional

operator. This finite-rank operator, $\tilde{\mathcal{C}}$, is a covariance operator which is now trace class. This truncated operator will be used in the numerical examples demonstrated in the following chapters.

Example 3.1. *The eigenvalue problem for the operator in (3.43) has*

$$\mathcal{C}\phi_{k,m}^{(j)} = \lambda_{k,m}\phi_{k,m}^{(j)}, \quad k, m \in \mathbb{N}, \quad j \in \{1, 2, 3, 4\}, \quad (3.44)$$

where

$$\begin{aligned} \phi_{k,m}^{(1)}(x, y) &= \frac{1}{2} \sin(2\pi kx) \sin(2\pi my), & \phi_{k,m}^{(2)}(x, y) &= \frac{1}{2} \sin(2\pi kx) \cos(2\pi my) \\ \phi_{k,m}^{(3)}(x, y) &= \frac{1}{2} \cos(2\pi kx) \sin(2\pi my), & \phi_{k,m}^{(4)}(x, y) &= \frac{1}{2} \cos(2\pi kx) \cos(2\pi my). \end{aligned}$$

And the eigenvalues are given by

$$\lambda_{k,m} = \alpha^2 \frac{\ell^2}{1 + 4\pi^2 \ell^2 (k^2 + m^2)}. \quad (3.45)$$

Proof. First we note that if $\mathcal{C}_\ell \phi = \lambda \phi$ then applying the inverse, $\phi = \lambda \mathcal{C}_\ell^{-1} \phi$,

$$\frac{\lambda}{\alpha^2} \left(-\Delta \phi + \frac{1}{\ell^2} \phi \right) = \phi \quad \text{on} \quad (0, 1) \times (0, 1). \quad (3.46)$$

Rearranging yields the eigenvalue problem on the unit square with periodic boundary conditions.

$$\Delta \phi + \mu^2 \phi = 0, \quad \mu^2 = \frac{\alpha^2}{\lambda} - \frac{1}{\ell^2}. \quad (3.47)$$

Therefore, we have four distinct eigenfunctions for integer pairs m, n :

$$\phi_{k,m}^{(1)} = \tilde{a} \sin(2\pi kx) \sin(2\pi my) \quad (3.48)$$

$$\phi_{k,m}^{(2)} = \tilde{b} \sin(2\pi kx) \cos(2\pi my) \quad (3.49)$$

$$\phi_{k,m}^{(3)} = \tilde{c} \cos(2\pi kx) \sin(2\pi my) \quad (3.50)$$

$$\phi_{k,m}^{(4)} = \tilde{d} \cos(2\pi kx) \cos(2\pi my), \quad (3.51)$$

and their coefficients can be shown to have $\tilde{a} = \tilde{b} = \tilde{c} = \tilde{d} = 0.5$ so that $\|\phi_{m,n}^{(j)}\|_{L^2(\Omega)} = 1$.

The corresponding eigenvalues can be computed first by determining μ^2 :

$$\mu^2 = 4\pi^2 (k^2 + m^2). \quad (3.52)$$

It follows from (3.47)

$$\lambda = \alpha^2 \frac{\ell^2}{1 + \ell^2 \mu^2}. \quad (3.53)$$

□

We construct the truncated operator by only using a finite set of eigenmodes. This is usually done so that $\lambda_{k,m} \leq \tau$ for all $k, m \geq N$ for a given tolerance, τ . Alternatively, one can truncate it before the oscillations in ϕ are no longer resolved by the finite element discretization. This truncated operator: $\tilde{\mathcal{C}}$, is trace class, and a Gaussian field $Y \sim \mathcal{N}(0, \tilde{\mathcal{C}})$ has KLE of the form

$$Y = \sum_{k=1}^N \sum_{m=1}^N \sum_{j=1}^4 Z_{k,m,j} \alpha \sqrt{\lambda_{k,m}} \phi_{k,m}^{(j)}(x), \quad Z_{k,m,j} \sim \mathcal{N}(0, 1) \quad i.i.d. \quad (3.54)$$

Moreover, this corresponding covariance operator can be written using its covariance kernel, which is now constructed using a finite sum.

$$\mathcal{C}f = \int_{\Omega} k(x, y) f(y) dy, \quad k(x, y) = \sum_{k=1}^N \sum_{m=1}^N \sum_{j=1}^4 \alpha^2 \lambda_{k,m} \phi_{k,m}^{(j)}(x) \phi_{k,m}^{(j)}(y). \quad (3.55)$$

Example random fields can be seen in Figure 3.1. These use the covariance operator defined in (3.55) for various correlation lengths. As the correlation length decreases, the random field becomes more uniform and homogeneous throughout the material. High values for the correlation length result in fields with large areas of high or low strength and exhibit fewer repeating patterns throughout the domain.

It is worth briefly examining two related covariance operators. We will not prove the following two cases, as they follow very similarly to that of the above case.

Example 3.2. *Let*

$$\mathcal{C} = \alpha^2 \left(-\Delta + \frac{1}{\ell^2} \right)^{-1}, \quad \text{on } H_0^1((0, 1) \times (0, 1)). \quad (3.56)$$

Where $H_0^1(\Omega)$ denotes the subspace of H^1 with zero-Dirichlet boundary conditions. Then the KLE of a mean-zero Gaussian field with a truncated version of the above covariance operator is

$$Y = \sum_{k=1}^N \sum_{m=1}^N \sum_{j=1}^2 \zeta_{k,m,j} \alpha \sqrt{\lambda_{k,m}} \phi_{k,m}^{(j)}(x), \quad \zeta_{k,m,j} \sim \mathcal{N}(0, 1) \quad i.i.d. \quad (3.57)$$

Where

$$\phi_{k,m}^{(1)}(x, y) = \frac{1}{2} \sin(2\pi kx) \sin(2\pi my), \quad \phi_{k,m}^{(2)}(x, y) = \frac{1}{2} \sin(2\pi kx) \sin(2\pi my)$$

And the eigenvalues are given by

$$\lambda_{k,m} = \alpha^2 \frac{\ell^2}{1 + 4\pi^2 \ell^2 (k^2 + m^2)}. \quad (3.58)$$

Example 3.3. Let

$$\mathcal{C} = \alpha^2 \left(-\Delta + \frac{1}{\ell^2} \right)^{-1}, \quad \text{on } H_{\text{Neu}}^1((0, 1) \times (0, 1)). \quad (3.59)$$

Where $H_{\text{Neu}}^1(\Omega)$ are mean-zero H^1 functions with zero-Neumann boundary conditions. Then the KLE of a mean-zero Gaussian field with a truncated version of the above covariance operator is

$$Y = \sum_{k=1}^N \sum_{m=1}^N \sum_{j=1}^2 \zeta_{k,m,j} \alpha \sqrt{\lambda_{k,m}} \phi_{k,m}^{(j)}(x), \quad \zeta_{k,m,j} \sim \mathcal{N}(0, 1) \quad \text{i.i.d.} \quad (3.60)$$

Where

$$\phi_{k,m}^{(1)}(x, y) = \frac{1}{2} \cos(2\pi kx) \cos(2\pi my), \quad \phi_{k,m}^{(2)}(x, y) = \frac{1}{2} \cos(2\pi kx) \cos(2\pi my)$$

And the eigenvalues are given by

$$\lambda_{k,m} = \alpha^2 \frac{\ell^2}{1 + 4\pi^2 \ell^2 (k^2 + m^2)}. \quad (3.61)$$

The constant term, corresponding to $k = m = 0$ can be safely disregarded, as by assumption, the Gaussian field has mean zero:

$$\int_{\Omega} Y(x) dx = 0. \quad (3.62)$$

In engineering studies, log-normal and Weibull fields are often of interest because they more realistically capture the variations seen in reality [33, 41]. Most often, these fields are constructed from simpler fields, which allows for a more simplistic construction of sampling algorithms.

3.5.3 Log Normal Fields

A random field Y over domain Ω is said to be log-normal when $\log(Y)$ is a Gaussian field. Because of this, we will often write

$$\log(Y(x)) \sim \mathcal{N}(\mu(x), \mathcal{C})$$

to indicate a log-normal field. Sampling from such a field can be done as follows. First, sample the Gaussian field, $X \sim \mathcal{N}(\mu, \mathcal{C})$, which can be done using the KLE as detailed above. Then build Y through $Y(x) = e^{X(x)}$, pointwise for every $x \in \Omega$.

Example log-normal random fields can be seen in Figure 3.2. These use the covariance operator defined in (3.55) for various correlation lengths.

3.5.4 Weibull Fields [61]

A Weibull field resembles a log-normal field but has an additional shape parameter κ . A Weibull field with mean $\mu(x) > 0$, covariance \mathcal{C} , and shape parameter κ can be built as follows. Sample $X_1, X_2 \sim \mathcal{N}(0, \mathcal{C})$ i.i.d. as described by the KLE. Then assemble a random field W via

$$W(x) = \mu(x) \frac{(X_1(x)^2 + X_2(x)^2)^{1/\kappa}}{2\Gamma(1 + 1/\kappa)}, \quad (3.63)$$

where $\Gamma(\cdot)$ is the Gamma function. The new variable W will have the desired Weibull distribution: $\mathcal{W}(\kappa, \mu, \mathcal{C})$. Example Weibull fields can be seen in Figure 3.3. These use the covariance operator defined in (3.55) for various correlation lengths.

Additionally, Figure 3.4 shows a side-by-side comparison of some example log-normal and Weibull random fields.

3.6 Computational Procedure for Sampling Random Fields

Samples for one of the aforementioned random fields can be generated using the following procedures. Assuming the covariance operator \mathcal{C} decomposition, a specified correlation length, ℓ and a mean function $\mu(x)$, and shape parameter (Weibull only) κ , one can generate samples using the following algorithms. In the above examples,

the eigenvalues and eigenfunctions are multi-indexed due to the various modes in the x and y directions. However, we can renumber these using a single index, i , which has a unique mapping from i to the multi-index (k, m, j) , for $i = 1, 2, \dots, I$. This re-indexing and eigendecomposition for the covariance operator can be done prior to any sample generation, then the resulting decomposition can simply be loaded for the required sample.

Algorithm 1 Sample from a 2D Mean-zero Random Gaussian Field

Input: Number of modes, I ; eigendecomposition $(\lambda_i, \phi_i(\underline{x}))$

Output: Sample $G(\underline{x})$

- 1: $Z_i \leftarrow \mathcal{N}(0, 1)$ for $i = 1, 2, \dots, I$, i.i.d.
 - 2: $G(\underline{x}) \leftarrow \sum_{i=1}^I Z_i \sqrt{\lambda_i} \phi_i(\underline{x})$
-

Algorithm 2 Sample from a 2D Random Log-Normal Field with Mean μ

Input: No. modes, I ; decomposition $(\lambda_i, \phi_i(\underline{x}))$; Mean, μ

Output: Sample $L(\underline{x})$

- 1: $G(\underline{x}) \leftarrow (\mathbf{Algorithm\ 1} \leftarrow (I, (\lambda_i, \phi_i)))$
 - 2: $T \leftarrow \sum_{i=1}^I \lambda_i$
 - 3: $\tilde{\mu} \leftarrow \exp(\mu(\underline{x}) - T/2)$
 - 4: $L(\underline{x}) \leftarrow \tilde{\mu}(\underline{x}) \cdot \exp(G(\underline{x}))$
-

Algorithm 3 Sample from a 2D Random Weibull Field

Input: No. modes, I ; decomp. $(\lambda_i, \phi_i(\underline{x}))$; Mean, μ ; Shape param. κ

Output: Sample $W(\underline{x})$

- 1: $G^{(1)}(\underline{x}) \leftarrow (\mathbf{Algorithm\ 1} \leftarrow (I, (\lambda_i, \phi_i)))$
 - 2: $G^{(2)}(\underline{x}) \leftarrow (\mathbf{Algorithm\ 1} \leftarrow (I, (\lambda_i, \phi_i)))$
 - 3: $E(\underline{x}) \leftarrow \left((G^{(1)})^2 + (G^{(2)})^2 \right) / 2$
 - 4: $W(\underline{x}) \leftarrow \mu(\underline{x}) \cdot (E(\underline{x}))^{1/\kappa} / \Gamma(1 + 1/\kappa)$
-

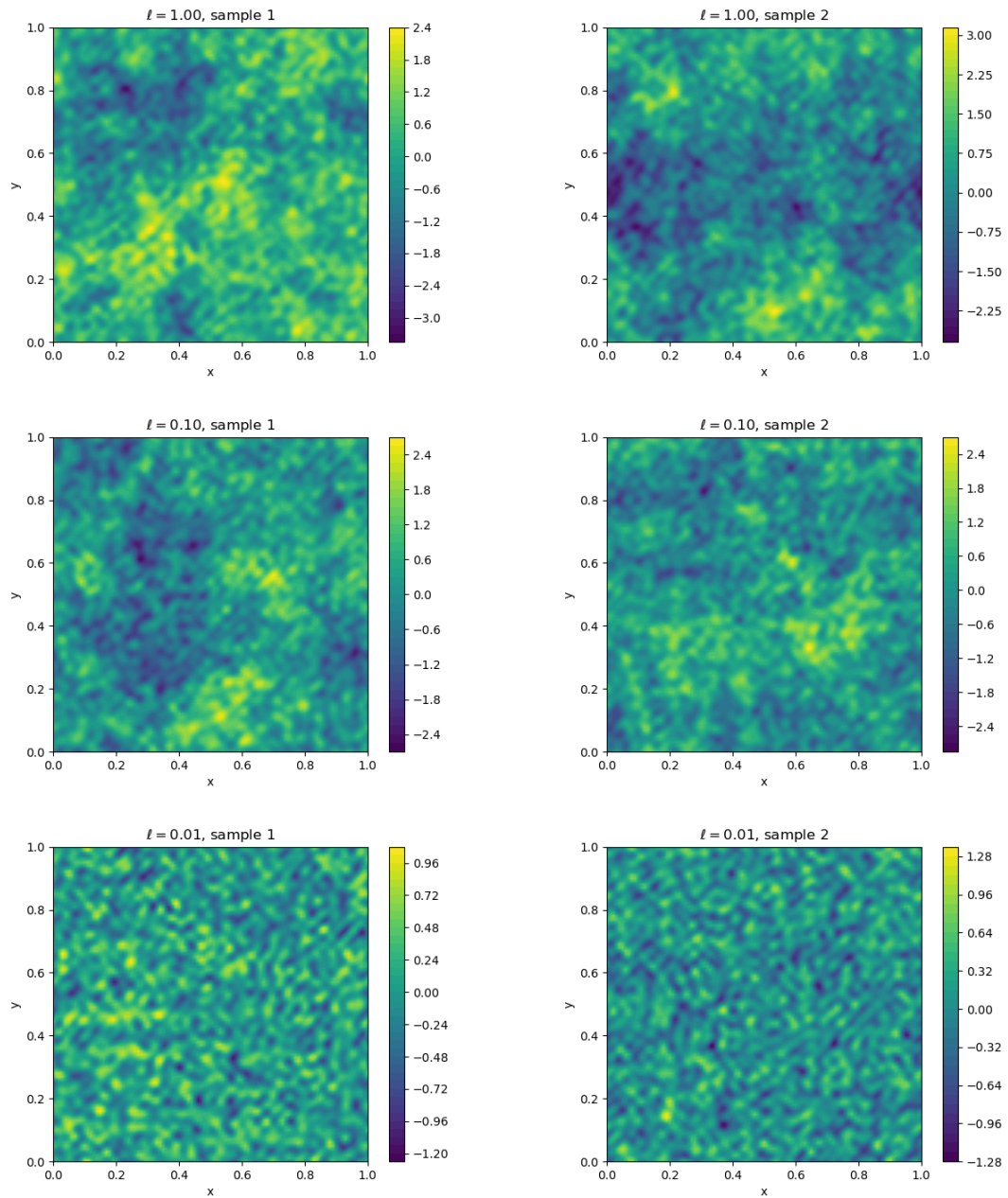


Figure 3.1: Example Random field samples from $X \sim \mathcal{N}(0, \mathcal{C}_\ell)$ for varying values of ℓ . From top to bottom $\ell = 1.0, 0.1$, and 0.01 . From left to right are samples 1 and 2 at each value of ℓ .

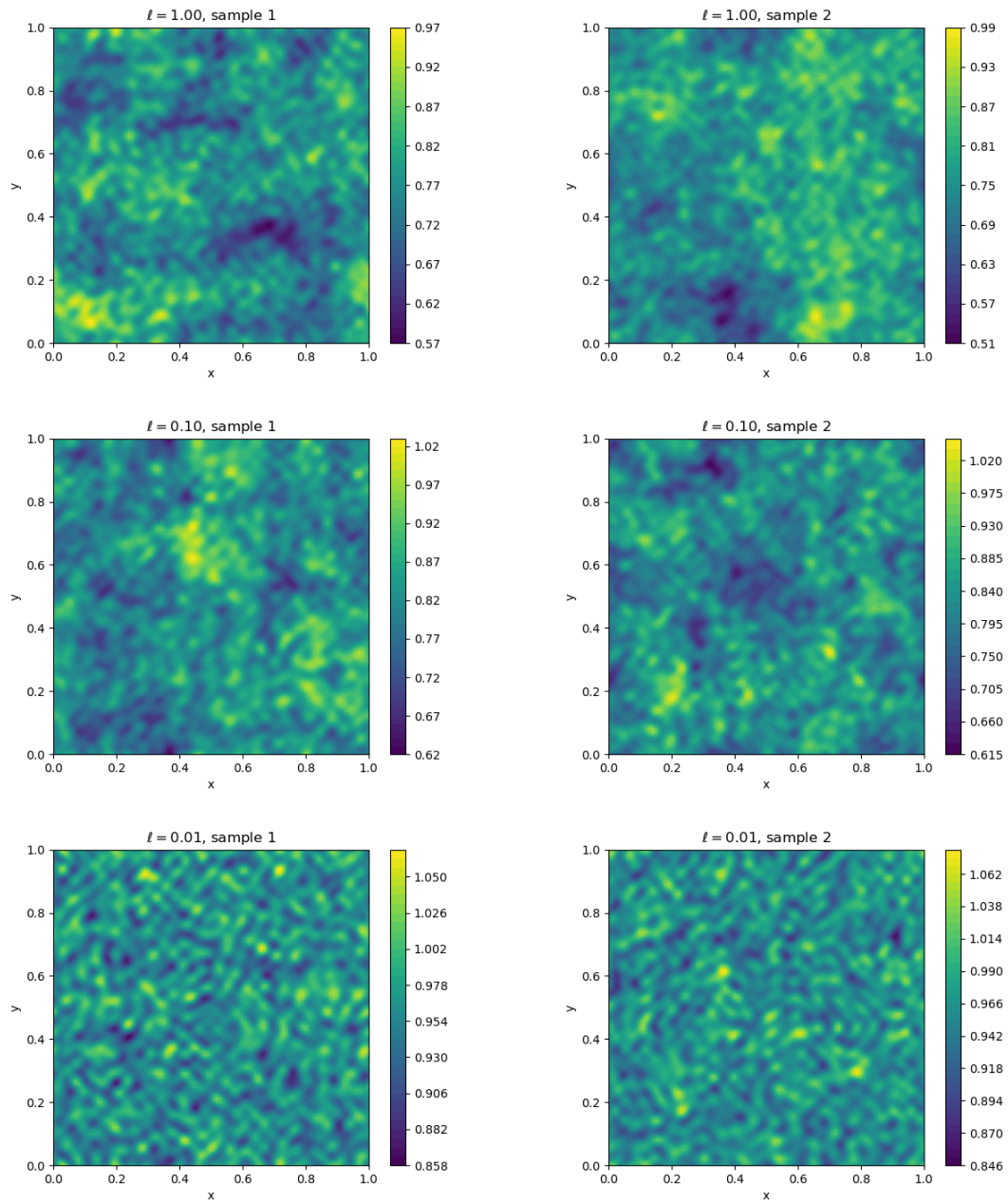


Figure 3.2: Example Random field samples from log normal random fields X with $\log X \sim \mathcal{N}(\mu, \mathcal{C}_\ell)$ for varying values of ℓ . From top to bottom $\ell = 1.0, 0.1$, and 0.01 . From left to right are samples 1 and 2 at each value of ℓ .

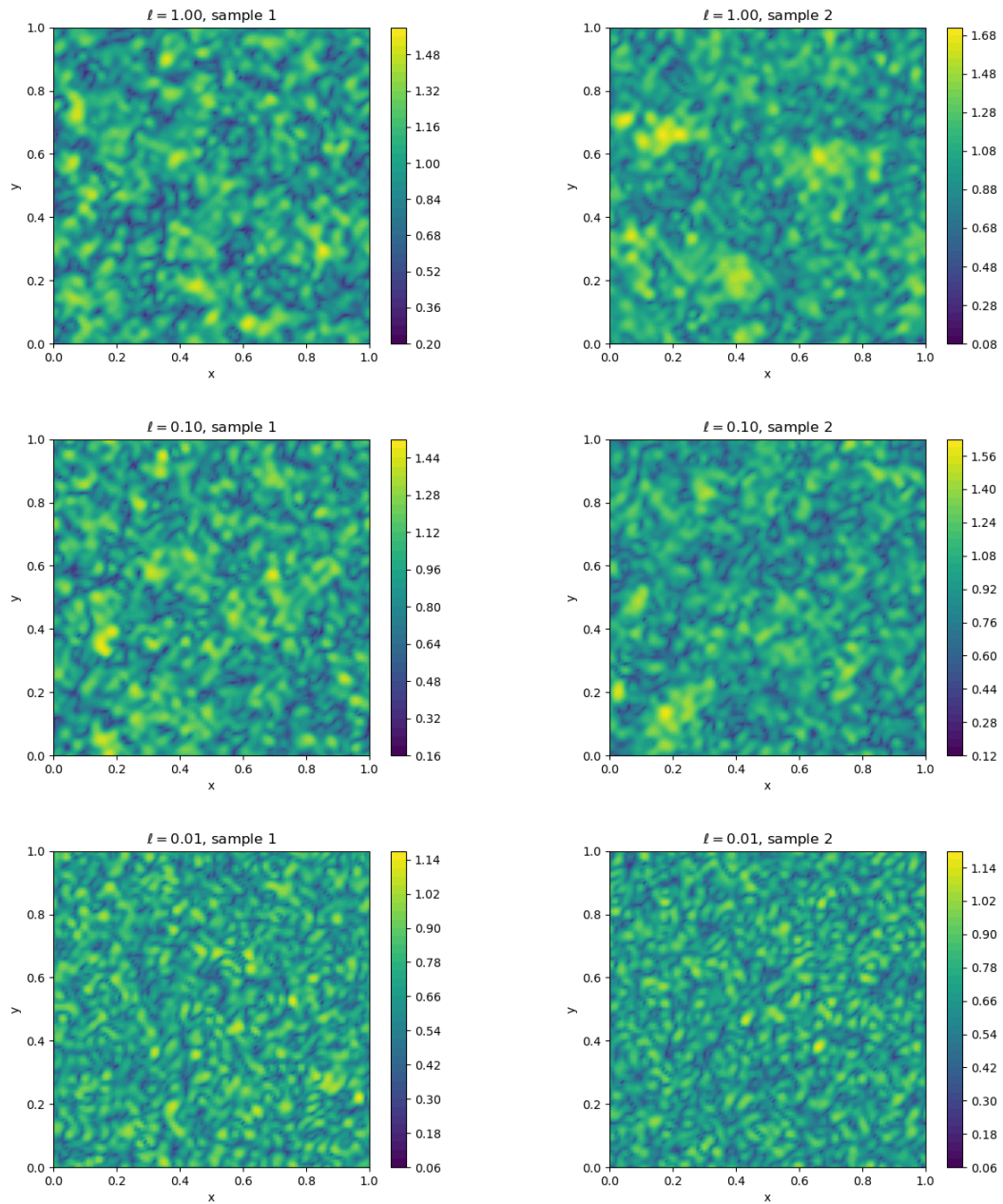


Figure 3.3: Example Random field samples from Weibull random fields W , for shape parameter $\kappa = 5$, for varying values of ℓ . From top to bottom $\ell = 1.0, 0.1$, and 0.01 . From left to right are samples 1 and 2 at each value of ℓ .

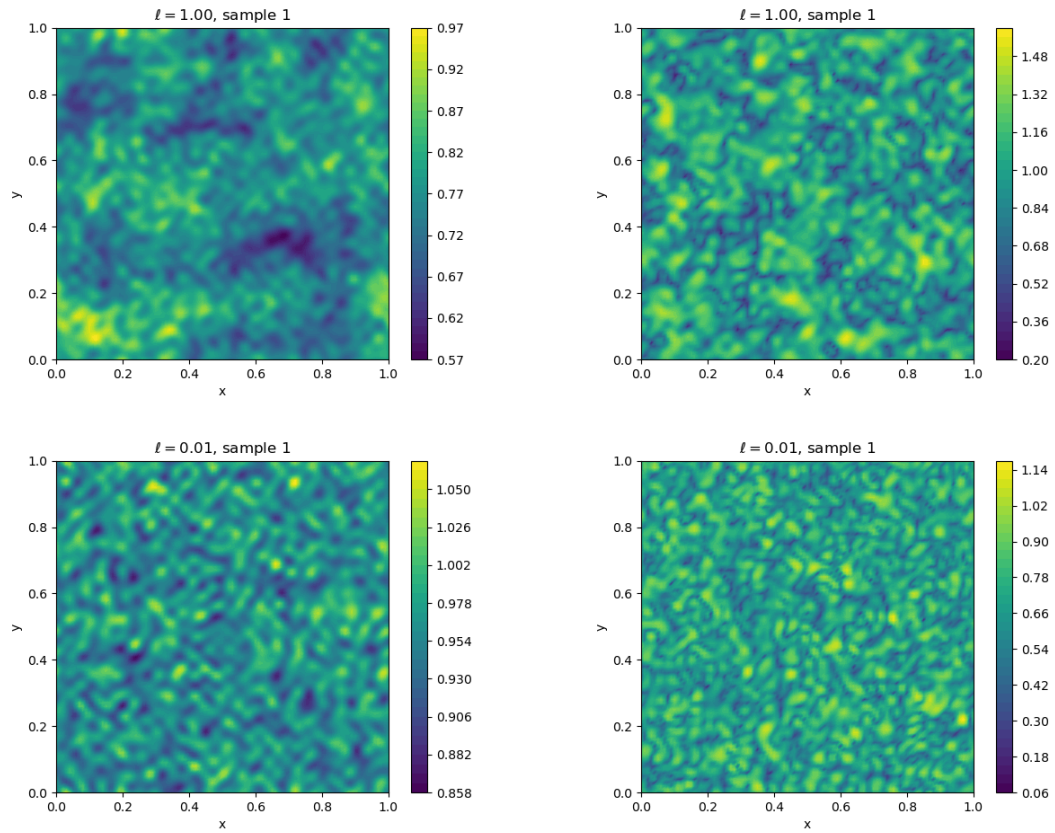


Figure 3.4: Comparison of log-normal and Weibull random fields for various correlation lengths. On the left are two log-normal field samples, and on the right are the corresponding Weibull field samples. Correlation lengths are 1.0 for the top figures and 0.01 for the bottom.

Chapter 4

UNCERTAINTY QUANTIFICATION

4.1 Introduction

In Chapter 3, we discussed random fields and how to build samples thereof. These fields can be used as input for the model described in Chapter 2, which produces a solution to the damage mechanics problem. From this solution, we can extract specific quantities of interest (QoIs), characterizations such as the stress-strain curve and times at which specific damage events occur.

The measured QoIs are themselves random variables. As such, we want to discuss and describe the uncertainty associated with their values. One example of this is the following: What are the conditions we need to look for, indicating material failure is imminent? The ideas from the area of Uncertainty Quantification (UQ) aim to address concerns such as these. Before proceeding, we will formally define what it is we mean when referring to a QoI.

Definition 4.1. *Let \mathcal{F} represent a model which takes (random) input X and produces (random) solution Y , that is $\mathcal{F} : X \mapsto Y$. From the output of the model, we extract specific values, $Q = \mathcal{Q}(Y)$. These extracted **quantities of interest (QoIs)** are resulting outputs from the model that we use to make decisions or conclusions about the underlying system being modeled [60].*

Importantly, \mathcal{F} is only a model, and

“[...] all models are wrong, but some are useful” - George E.P. Box [60]

So we need to contend not only with the randomness of our model input, X , but also with errors produced by our model. Both of these can be sources of uncertainty, adding

to the potential unknowns in the problem. We can separate these uncertainties into two main types.

Definition 4.2. ***Aleatoric uncertainty** is uncertainty coming from inherent randomness. Our models rely on a random field, which determines the evolution of the system, and there is no way to avoid the randomness of the underlying random field.*

***Epistemic uncertainty** is uncertainty stemming from the modeling assumptions. In principle, a better model capturing more physics can help to reduce this uncertainty, but it can never be fully eliminated.*

The various moments for a QoI can be used to build an idea for the distribution of the QoI and to better understand the associated uncertainty. For example, the mean of a random variable is the first moment, while the variance is a function of the second moment. Moreover, this idea can be expanded to any function of a random variable.

Definition 4.3. *Let X be a random variable, with a range of values \mathcal{X} , and a probability measure μ on \mathcal{X} . Let $f : \mathcal{X} \rightarrow \mathcal{Y}$ be a μ -measurable function. Then $Y = f(X)$ is a random variable, and the **expectation value** of $f(X)$ is given by*

$$\mathbb{E}[f(X)] = \sum_{x \in \mathcal{X}} f(x)\mu(x). \quad (4.1)$$

*Furthermore, if $f(x) = x$, this expectation value is the **mean of X** . Similarly, letting $f(x) = (x - \mathbb{E}[X])^2$, the expected value is the **variance of X** , written as $\text{Var}[X]$.*

The main idea in UQ, therefore, is to build estimates for the expectation value of various functions of the random QoI. These can be to determine the mean, variance, or standard deviation; as well as other values.

4.2 Methods for UQ of QoIs

4.2.1 Polynomial Chaos

A method gaining traction in the area of UQ is polynomial chaos. The basic idea of this is as follows [65]. In general, the QoI-forward-eval map may depend on

non-random parameters such as time, in addition to its random inputs. This means we can write $Q = \mathcal{G}(\boldsymbol{\beta}, \mathbf{X})$, where $\boldsymbol{\beta}$ are the non-stochastic inputs, and \mathbf{X} represent the random inputs. If we know the distribution for \mathbf{X} (assumed to be a continuous random variable), we define a probability density function (PDF), ρ , of \mathbf{X} . We can further define an inner product using ρ over \mathcal{X} by

$$\langle f, g \rangle_\rho := \int_{\mathcal{X}} f(\mathbf{x})g(\mathbf{x})\rho(\mathbf{x}) dx = \mathbb{E}[f \cdot g]. \quad (4.2)$$

We can choose an orthonormal basis for continuous functions over \mathcal{X} under this inner product (see [65] for specific cases of common distributions). Let these basis functions be $\phi_j(\mathbf{x})$.

Next, we can choose a collection of collocation points, \mathbf{x}_k , for $k = 1, 2, \dots, N$, at which we will evaluate the model. Let $L_k(\mathbf{x})$ represent the Lagrange polynomial basis from the collocation points. We can then represent the forward map via its interpolant:

$$\mathcal{G}(\boldsymbol{\beta}, \mathbf{x}) = \sum_{k=1}^N \mathcal{G}(\boldsymbol{\beta}, \mathbf{x}_k)L_k(\mathbf{x}). \quad (4.3)$$

A change of basis formula can be applied to transform the coefficients into those for the orthonormal basis mentioned above:

$$\mathcal{G}(\boldsymbol{\beta}, \mathbf{x}) = \sum_{k'=1}^{N'} \hat{\mathcal{G}}_{k'}(\boldsymbol{\beta})\phi_{k'}(\mathbf{x}). \quad (4.4)$$

This can be done using the orthonormality of the ϕ_j by

$$\hat{\mathcal{G}}_j(\boldsymbol{\beta}) = \langle \phi_j, \mathcal{G}(\boldsymbol{\beta}, \mathbf{x}) \rangle_\rho = \sum_{k=1}^N \mathcal{G}(\boldsymbol{\beta}, \mathbf{x}_k) \langle \phi_j, L_k \rangle_\rho. \quad (4.5)$$

Then, expectation values can be taken using the orthonormality properties of the ϕ_k . For example, if $\phi_1 = 1$, then

$$\mathbb{E}[\mathcal{G}(\boldsymbol{\beta}, \mathbf{X})] = \hat{\mathcal{G}}_1(\boldsymbol{\beta}) \quad (4.6)$$

$$\text{Var}[\mathcal{G}(\boldsymbol{\beta}, \mathbf{X})] = \sum_{k'=1}^{N'} \hat{\mathcal{G}}_{k'}^2(\boldsymbol{\beta}). \quad (4.7)$$

Polynomial chaos has an advantage in that collocation points can be chosen strategically to reduce uncertainty. Given the model evaluations at the collocation points, producing higher moments of the resulting QoI distribution is straightforward.

The main disadvantage of polynomial chaos arises from applying it to high-dimensional problems. In the case of a random field, which is infinitely dimensional, this becomes prohibitively difficult. While the KLE discussed in Chapter 3 enables random fields to be identified with a finite-dimensional random vector, the length of this vector can be large enough to make polynomial chaos infeasible.

4.2.2 Monte Carlo Methods

Monte Carlo (MC) methods provide a simplistic but reliable method to sample from a random QoI. The basic approach is as follows: Generate a collection of samples for the random input data \mathbf{X} . We call these samples $\mathbf{X}^{(1)}, \mathbf{X}^{(2)}, \dots, \mathbf{X}^{(N)}$. These samples are drawn from the given distribution for \mathbf{X} , and in the case of a random field, the KLE can be used to make the sampling feasible. For each sample, compute the corresponding QoI: $Q^{(n)} = \mathcal{Q} \circ \mathcal{F}(\boldsymbol{\beta}, \mathbf{X}^{(n)})$. Afterward, apply statistical methods to the resultant QoI samples $Q^{(1)}, Q^{(2)}, \dots, Q^{(N)}$.

The simplicity of MC methods makes them easy to implement and use. However, their main drawback comes from the sheer number of samples needed to obtain reliable results. This can easily be illustrated through the most common use of MC methods - the Central Limit Theorem.

The examples presented in the following chapters will rely on MC methods for sampling QoIs. The nature of the random field Σ means polynomial chaos will be far too computationally intensive to be of much use. To this end, we will examine how we can extract estimates for our QoI distributions using the output of MC sampling sets.

4.3 Statistical Concepts and Monte Carlo Methods

After performing MC sampling, we will have a collection of data $Q^{(1)}, Q^{(2)}, \dots, Q^{(N)}$, representing samples of a particular QoI. We need a way to build an estimate of the

overall distribution of Q from these samples.

Definition 4.4. An *estimator* based on samples $Q^{(1)}, \dots, Q^{(N)}$ is a procedure to build a quantity describing part or all of the distribution of Q . The *estimate* is a realization of the estimator, for a collection of realized samples.

The most common example of an estimator is the sample mean:

$$\overline{Q}^{(N)} = \frac{1}{N} \sum_{n=1}^N Q^{(n)}. \quad (4.8)$$

More generally, an estimator for an arbitrary function, f of Q can be computed in an analogous way

$$\overline{f(Q)}^{(N)} = \frac{1}{N} \sum_{n=1}^N f(Q^{(n)}). \quad (4.9)$$

Once we collect a set of N samples for $Q^{(n)}$ and evaluate the numeric value of $\overline{Q}^{(N)}$, we will have realized the sample mean. An important result for these estimators is the Central Limit Theorem, which describes how large sample sizes will behave.

Theorem 4.1 (Central Limit Theorem (CLT) [59]). *Let $Q^{(1)}, \dots, Q^{(N)}$ be i.i.d. samples for a random variable Q . Then*

$$\frac{\overline{Q}^{(N)} - \mathbb{E}[Q]}{\sqrt{\text{Var}[Q]/N}} \implies \mathcal{N}(0, 1), \quad (4.10)$$

as $N \rightarrow \infty$. Here \implies indicates convergence in distribution.

Definition 4.5. Let X_n be a sequence of random variables, each with cumulative distribution function (CDF) $F_n(x)$ respectively, and Y be a random variable with CDF $G(y)$. We say $X_n \implies Y$ or X_n **converges in distribution** to Y as $n \rightarrow \infty$ when

$$\lim_{n \rightarrow \infty} F_n(x) = G(x), \quad (4.11)$$

for all x at which G is continuous [59].

Rearranging the CLT gives that for large N , $\overline{Q}^{(N)}$ converges in distribution to a normally distributed random variable, with mean $\mathbb{E}[Q]$ and variance $\text{Var}[Q]/N$. To make the power of this statement more clear, we define some other useful quantities:

Definition 4.6. The **standard deviation** of a random variable Z , ς_Z is given by

$$\varsigma_Z = \sqrt{\text{Var}[Z]}. \quad (4.12)$$

Given a collection of samples of Z , $Z^{(1)}, Z^{(2)}, \dots, Z^{(N)}$, the estimator itself, $\bar{Z}^{(N)}$, is a random variable. The standard deviation of the estimator is called the **standard error**[58], and can be written

$$\varsigma_{\bar{Z}} = \sqrt{\frac{\text{Var}[Z]}{N}}. \quad (4.13)$$

The **sample standard deviation**, s_Z , is given by

$$s_Z = \sqrt{\frac{1}{N} \sum_{n=1}^N \left(Z^{(n)} - \bar{Z}^{(N)} \right)^2}. \quad (4.14)$$

The standard error is often used as a measure of the precision of the estimator. Through the CLT, we can refine the precision simply by evaluating more samples, as the standard error scales like $O(N^{-1/2})$. However, this scaling means we may need to generate an enormous number of samples to achieve a desired precision. For every additional significant figure we wish to obtain, we must use 100 times more samples. Additionally, we often do not have access to the standard deviation of Z , and instead may only have access to the sample standard deviation. Because of this, we will often use the sample standard deviation in place of the true standard deviation. We can still use this to get a read on the standard error, by substituting s_Z in place of $\sqrt{\text{Var}[Z]}$ in (4.13).

Suppose one has an estimator, \bar{Q} , for a QoI Q . If, in addition, one also has access to a true value, \hat{Q} , it is possible to quantify the discrepancy between the estimator and the true value. Two such quantifiers are the bias and mean-square error.

Definition 4.7. Let \bar{Q} be an estimator for a QoI Q , using N samples. Let \hat{Q} be the true value for this estimator. The **bias** of the estimator is given by

$$\text{Bias}(\bar{Q}, \hat{Q}) = \mathbb{E}[\bar{Q}] - \hat{Q}. \quad (4.15)$$

The **mean-square error (MSE)** is given by

$$\text{MSE}(\bar{Q}, \hat{Q}) = \mathbb{E} \left[\left| \bar{Q} - \hat{Q} \right|^2 \right]. \quad (4.16)$$

Additionally, a straightforward calculation reveals the relation,

$$\text{MSE}(\bar{Q}, \hat{Q}) = \text{Var}[\bar{Q}] + \text{Bias}(\bar{Q}, \hat{Q})^2. \quad (4.17)$$

Thus, for an unbiased estimator, the MSE is simply its variance. Distinguishing between these two quantities is important when discussing quantities for which the estimator is biased. Of particular note is the estimator from the CLT, which is an unbiased estimator of the mean. Therefore the MSE of the CLT estimator is simply the square of the standard error. The relation in (4.17) shows how the MSE can be written as to split the error between the statistical error on Q , and the bias of the estimator.

Knowing the standard error and standard deviation from a collection of samples enables the construction of confidence intervals. These confidence intervals indicate bounds for which we expect a realization for a random variable to be contained. This can be extremely useful for UQ applications, as it allows the construction of engineering tolerances.

Definition 4.8. *For a univariate random variable, Z , a **confidence interval** with confidence level $\alpha \in [0, 1]$ is an interval $(z_{\text{lower}}, z_{\text{upper}})$ such that*

$$\mathbb{P}(z_{\text{lower}} < Z < z_{\text{upper}}) \geq 1 - \alpha. \quad (4.18)$$

For a random vector, \mathbf{Z} , the idea of a confidence interval can be extended to a confidence region, R with

$$\mathbb{P}(\mathbf{Z} \in R) \geq 1 - \alpha. \quad (4.19)$$

A common way to do this is to create confidence intervals for each component of \mathbf{Z} and join the intervals together into a rectangular region.

Often these confidence intervals are based on the results from the CLT. Given a realization of the estimator for a QoI, $\bar{Q}^{(N)}$, and its standard error, we can infer that $\bar{Q}^{(N)}$ comes from an approximately normal distribution. Then we can build a confidence interval for a normally distributed random variable with mean $\bar{Q}^{(N)}$ and standard deviation given by its standard error. If $\alpha = 0.05$, for instance, then the

associated bounds $q_{\text{lower}}, q_{\text{upper}}$ are two standard deviations away from the mean and provide 95 % confidence bounds for the potential values of $\mathbb{E}[Q]$.

A note of caution if applying this approach to the random variable itself. The central limit theorem applies only to the estimator of $\bar{Q}^{(N)}$, not to individual samples $Q^{(n)}$. If it is known (or assumed) that Q is a normally distributed random variable, the same process can be applied using the mean $\bar{Q}^{(N)}$ and standard deviation of Q . Doing so will build a confidence interval for the value of $Q^{(n)}$ for a new sample n . There are many programs to do these computations automatically, most notably the `scipy.stats` and `pandas` packages available for Python. Alternatively, one can build an interval which is $k\zeta$'s from the mean, i.e. a 95 % confidence interval is 2ζ 's from the mean.

4.3.1 Parametric Statistics and The Maximum Likelihood Estimator

Gaussian distributions are useful in the context of the CLT, but often the distribution of Q itself may be non-Gaussian. Estimates of $\bar{Q}^{(N)}$ and s_Q can be applied to understand properties of other distributions as well. Parametric statistics use various moment estimators to approximate the parameters of an assumed statistical distribution. In the case of a Gaussian distribution, one needs only determine the mean and variance (or standard deviation equivalently). Similar approaches could be employed for Bernoulli, Poisson, exponential, and geometric distributions as well as others [60].

A common technique for parametric statistics is the Maximum Likelihood Estimator (MLE). The idea of MLE is to construct a likelihood function governed by the parameters in the distribution, then optimize the parameters to maximize the likelihood. In general, let y be an observed variable, which is assumed to have a probability distribution $p(y; \theta)$, where θ is a collection of parameters. We can think of p as providing a probability of observing the value of y , given the parameter values θ .

Given a collection of i.i.d. samples $Y^{(n)}$ for $n = 1, 2, \dots, N$, we can construct the likelihood function, or probability of seeing the observations $Y^{(n)}$ given the parameter

values of θ :

$$\mathcal{L}(Y \mid \theta) = \prod_{n=1}^N p(Y^{(n)}; \theta). \quad (4.20)$$

Then viewing $\mathcal{L}(Y \mid \theta)$ as a function of θ , it is possible to compute the optimal value of θ to maximize \mathcal{L} .

Typically to make the computation easier, we work with the log-likelihood:

$$F(\theta) := \log(\mathcal{L}(Y \mid \theta)) = \sum_{n=1}^N \log(p(Y^{(n)}; \theta)). \quad (4.21)$$

Then optimality can be determined by taking derivatives with respect to θ and optimizing the resulting system. Such procedures can be done automatically using the `scipy.stats` module in Python.

4.3.2 Nonparametric Statistics

Alternatively, non-parametric statistics provide methods to understand distributions other than those parameterized by a fixed set of values. A common approach is using a histogram to group values into specific bins. A histogram will work best for a discrete random variable; however, it can also be applied to random variables which are known to be continuous.

A similar approach is kernel density estimation (KDE) [60]. The idea behind a kernel density estimator is to build a function $\hat{\rho}(x)$ based on a collection of random samples $Q^{(1)}, \dots, Q^{(N)}$ of a random variable, Q , which approximates the PDF of Q , ρ . This is done through the use of a kernel function $\kappa_h(x)$ with a length parameter h , that aids in smoothing the resulting PDF approximation. The KDE for a random variable is constructed by

$$\hat{\rho}(x) = \mathbb{E}[\kappa_h(x - Q)]. \quad (4.22)$$

For a collection of samples, $Q^{(1)}, \dots, Q^{(N)}$ this expectation value can be approximated through an estimator:

$$\bar{\rho}(x) = \frac{1}{N} \sum_{n=1}^N \kappa_h(x - Q^{(n)}). \quad (4.23)$$

The `scipy.stats` package provides methods for building both univariate and multivariate KDEs.

The approximated PDF can be used to build an approximate probability measure for the QoI:

$$\hat{F}(B) = \int_B \hat{\rho}(x) dx. \quad (4.24)$$

For a univariate distribution, this measure is equivalent to a cumulative distribution function (CDF) for a random variable Q , gives probabilities that $Q \leq x$:

$$C(x) = \mathbb{P}(Q \leq x). \quad (4.25)$$

This probability can also be written as the expectation value of an indicator random variable of the event ($Q \leq x$):

$$\mathbb{P}(Q \leq x) = \mathbb{E}[\mathbb{1}(Q \leq x)]. \quad (4.26)$$

The event $\mathbb{1}(Q \leq x)$ is a Bernoulli random variable for all x . Therefore, we can compute its variance as follows:

$$\text{Var}[\mathbb{1}(Q \leq x)] = \mathbb{E}[(\mathbb{1}(Q \leq x) - \mathbb{E}[\mathbb{1}(Q \leq x)])^2] \quad (4.27)$$

$$= \mathbb{E}[\mathbb{1}^2(Q \leq x)] - (\mathbb{E}[\mathbb{1}(Q \leq x)])^2 \quad (4.28)$$

$$= \mathbb{P}(Q \leq x) - \mathbb{P}(Q \leq x)^2. \quad (4.29)$$

This enables the construction of a confidence interval around the constructed CDF, enabling UQ on the distribution itself.

Usually, we don't have access to exact values of $\mathbb{1}(Q \leq x)$, and instead have a collection of samples:

$$p^{(n)}(x) = \begin{cases} 1 & Q^{(n)} \leq x \\ 0 & Q^{(n)} > x \end{cases}. \quad (4.30)$$

Constructing the PDF and CDF uses the determined values of $p^{(n)}$. Assuming the $Q^{(n)}$ are i.i.d. (therefore, so are the $p^{(n)}$), the resulting estimator, $\bar{p}^{(N)}(x) \approx \mathbb{P}(Q \leq x)$, is then a scaled Binomial random variable. One method to build a confidence interval

around Binomial variables is the Clopper-Pearson method. Given a statistical level of significance, $\alpha \in (0, 1)$, we compute values p_{lower} and p_{upper} such that

$$\sum_{k=B}^N \binom{N}{k} p_{\text{lower}}^k (1 - p_{\text{lower}})^{N-k} = \frac{\alpha}{2}, \quad (4.31)$$

$$\sum_{k=0}^B \binom{N}{k} p_{\text{upper}}^k (1 - p_{\text{upper}})^{N-k} = \frac{\alpha}{2}, \quad (4.32)$$

where

$$B = \sum_{n=1}^N p^{(n)}. \quad (4.33)$$

The interval $(p_{\text{lower}}, p_{\text{upper}})$ then provides a set of bounds for $\mathbb{P}(Q \leq x)$ with confidence $1 - \alpha$. This procedure can be repeated for each x to build bounds for the entire CDF.

4.4 Uncertainty in Probability Measure

The PDF for a random variable can be associated with a probability measure. Let ρ be the associated PDF, and μ , its corresponding probability measure. If \mathcal{X} is the domain of ρ , then from the definition of the PDF we can write

$$\mu(B) = \int_B \rho(x) dx \quad \forall B \subset \mathcal{X}. \quad (4.34)$$

However, for QoIs generated by MC sampling, we may not have access to either the true PDF or the true probability measure. As a result, all estimators we generate may be incorrect. This is due to the model's epistemic uncertainty, the limited sampling used in the MC framework, and the ever-present aleatoric uncertainty.

To address this problem, we need to perform UQ on the probability measure itself. To this end, we adopt the nomenclature used in [66].

Definition 4.9. *The **nominal model** will be the model to which we have access, and which produces our results, with the added epistemic uncertainty due to modeling errors. The **alternative model** will represent a different and (presumably) better model, with reduced epistemic uncertainty and/or improved accuracy.*

In [65], the authors present a method to bound the results for estimating a QoI under an alternative model with different epistemic uncertainty than that of the nominal model. For each model, we will have a different probability measure. To that end, we need to quantify the differences between two probability measures.

Let μ and ν be two probability measures on the same space \mathcal{X} . The easiest quantification of their difference, provided we have access to their CDFs, F and G , respectively, is the Kolmogorov-Smirnov Statistic, given by

$$KS(F, G) = \sup_{x \in \mathcal{X}} |F(x) - G(x)|. \quad (4.35)$$

This can be generalized to the total-variation between measures μ and ν by

$$TV(\mu, \nu) = \sup_{B \subset \mathcal{X}} |\mu(B) - \nu(B)|. \quad (4.36)$$

Another quantifier is the relative entropy or Kullback-Leibler divergence.

Definition 4.10. *The **relative entropy** or **Kullback-Leibler divergence** between two probability measures μ and ν is given by*

$$D_{KL}(\mu || \nu) = \begin{cases} \int_{\mathcal{X}} \log \left(\frac{d\mu}{d\nu} \right) \mu(dx) & \mu \ll \nu \\ \infty & \text{otherwise} \end{cases} \quad (4.37)$$

Where \mathcal{X} is the domain of μ , and $\frac{d\mu}{d\nu}$ is the Radon-Nikodym derivative of μ with respect to ν . If the PDFs of μ and ν are ρ_{μ} and ρ_{ν} respectively, then

$$\frac{d\mu}{d\nu} = \frac{\rho_{\mu}}{\rho_{\nu}}, \quad \mu(dx) = \rho_{\mu}(x) dx. \quad (4.38)$$

In [65], the authors demonstrate a method for bounding the expectation value of an estimator under an alternative distribution with different epistemic uncertainty than that of the nominal model. They go on to illustrate how the aleatoric and epistemic uncertainties can be separated in certain cases, allowing one to examine the effect alternate models would have on the epistemic uncertainty alone.

We build on the work of [66] in which the authors extend the work [65] to construct bounds for $\mathbb{E}[Q]$ under an alternative model with a different epistemic uncertainty. Let μ be the probability measure on a space \mathcal{X} associated with the nominal model, and let $\tilde{\mu}$ be the measure for the alternative model.

Theorem 4.2. *Let Q be a random variable, and μ and ν be probability measures on the same space \mathcal{X} . Assume $\nu \ll \mu$, and let*

$$\mathbb{E}_\mu[Q] = \int_{\mathcal{X}} Q d\mu, \quad \text{Var}_\mu[Q] = \mathbb{E}_\mu[(Q - \mathbb{E}_\mu[Q])^2]. \quad (4.39)$$

Then

$$|\mathbb{E}_\nu[Q] - \mathbb{E}_\mu[Q]| \leq \sqrt{\text{Var}_\mu[Q]} \sqrt{2D_{KL}(\nu \parallel \mu)} + O(D_{KL}(\nu \parallel \mu)). \quad (4.40)$$

Theorem 4.2 is rigorously proved in [66]. For convenience, the basic outline of the proof is summarized below.

Consider the log-moment-generate function

$$\Lambda_{\mu,Q}(c) = \log(\mathbb{E}_\mu[e^{c(Q - \mathbb{E}_\mu[Q])}]) = \log\left(\int_{\mathcal{X}} e^{c(Q - \mathbb{E}_\mu[Q])} d\mu\right). \quad (4.41)$$

Building on the work from [65], the authors of [66] show

$$\Lambda_{\mu,Q}(c) = \sup_{\nu \ll \mu} \{c(\mathbb{E}_\nu[Q] - \mathbb{E}_\mu[Q]) - D_{KL}(\nu \parallel \mu)\}. \quad (4.42)$$

Furthermore, this can be rearranged to bound the difference in expectation value under different models,

$$G(-c) \leq \mathbb{E}_\nu[Q] - \mathbb{E}_\mu[Q] \leq G(c), \quad (4.43)$$

where

$$G(c) = \frac{1}{c} \Lambda_{\mu,Q}(c) + \frac{1}{c} D_{KL}(\nu \parallel \mu). \quad (4.44)$$

Taking $\Xi_+ = \inf_{c>0} G(c)$ and $\Xi_- = \sup_{c>0} G(-c)$ as the optimal bounds, [66] linearizes these bounds to build a simple formula for the uncertainty in the difference of expectation value.

This is done by first showing that there is a $c^* > 0$ at which Ξ_{\pm} achieves the respective extrema. This optimal c^* can be written as

$$c^* = \sqrt{\frac{2}{\text{Var}_{\mu}[Q]}}\delta + O(\delta^2) \quad (4.45)$$

for $\delta \in (0, \delta_0)$ with $\delta_0 < \infty$. Moreover, the bounds Ξ_{\pm} admit representation of the form

$$\Xi_{\pm} = \Lambda'_{\mu,Q}(\pm\Phi^{-1}(D_{KL}(\nu \parallel \mu))), \quad (4.46)$$

where Φ^{-1} is the inverse of Φ , which is defined by

$$\Phi(c) = -\Lambda_{\mu,Q}(c) + c\Lambda'_{\mu,Q}(c). \quad (4.47)$$

Taking $\delta^2 = D_{KL}(\nu \parallel \mu)$ and Taylor expanding in δ yields the desired result.

The relation (4.40) presents a tractable method for computing the UQ bounds. Additionally, for non-scalar QoIs, this bound provides a quick way to expand the UQ bounds to the vector or field case. Moreover, values for the relative entropy between parameterized distributions are tabulated, and other distributions can be approximated numerically using various software.

Examining (4.40), it is clear the bound on the uncertainty depends on two separate quantities. The first is the standard deviation of the QoI itself, which is very straightforward to compute. The second quantifies the discrepancy between the two probability distributions. Specifically, the remaining error term indicates this bound holds for distributions around μ with a relatively small relative entropy. We can consider (4.40) in the context of a nominal and alternative model, where the nominal model takes the place of μ , and the alternative model takes the place of ν . Knowing the relative entropy between the two, it is possible to place bounds on the uncertainty of the QoI value.

It is worth noting that for the variables used in this thesis, the underlying distributions come from random fields. The relative entropy computations between various random fields are nontrivial. To this end, some examples are shown below.

4.5 Relative Entropy Between Select Distributions

Consider two Gaussian fields, $\mathcal{N}(\mu, \mathcal{C})$ and $\mathcal{N}(\tilde{\mu}, \tilde{\mathcal{C}})$, with associated Gaussian probability measures γ and $\tilde{\gamma}$ respectively. For simplicity, we will denote $X \sim \gamma$ to denote a random variable from a distribution with measure γ .

Chapter 3 describes how a Gaussian field X can be associated with a Gaussian vector $\mathbf{Z} \sim \mathcal{N}(\mathbf{0}, I)$. In (3.21), we can substitute $\zeta_n = Z_n \sqrt{\lambda_n}$. In the truncated KLE, this means we associate a Gaussian vector $\boldsymbol{\zeta} \sim \mathcal{N}(\mathbf{0}, \Lambda)$ with the Gaussian field X , where Λ is a diagonal matrix whose entries are the eigenvalues from the eigendecomposition of the covariance operator of X . To that end, we can start by examining the relative entropy between two Gaussian vectors.

4.5.1 Gaussian Vectors

Consider a Gaussian vector $\mathbf{X} \sim \mathcal{N}(\mathbf{0}, \Sigma)$. We can evaluate the relative entropy between the distribution of \mathbf{X} and a different Gaussian vector with a different covariance matrix.

Theorem 4.3. *Let $X_i \sim \mathcal{N}(\mathbf{0}, \Sigma_i)$ for $i = 1, 2$ be two N -dimensional random Gaussian vectors with probability measures γ_1, γ_2 . Assume both Σ_i have full rank. Then*

$$D_{KL}(\gamma_2 \parallel \gamma_1) = \frac{1}{2} \left[\log \frac{\det \Sigma_1}{\det \Sigma_2} - N + \text{tr}(\Sigma_1^{-1} \Sigma_2) \right]. \quad (4.48)$$

Proof. Both of these measures admit PDFs in \mathbb{R}^N :

$$\mathbf{X} \sim \mathcal{N}(\mathbf{0}, \Sigma) \implies \rho(\mathbf{x}) = \frac{1}{(2\pi)^{N/2} \sqrt{\det \Sigma}} \exp\left(-\frac{1}{2} \mathbf{x}^T \Sigma^{-1} \mathbf{x}\right). \quad (4.49)$$

Then the relative entropy can be written

$$D_{KL}(\gamma_2 \parallel \gamma_1) = \frac{1}{2} \int_{\mathbb{R}^N} \left[\log \left(\frac{(2\pi)^N \det \Sigma_1}{(2\pi)^N \det \Sigma_2} \right) + \mathbf{x}^T \Sigma_1^{-1} \mathbf{x} - \mathbf{x}^T \Sigma_2^{-1} \mathbf{x} \right] \rho_2(\mathbf{x}) dx. \quad (4.50)$$

By applying that the integral over \mathbb{R}^N of $\rho_2(\mathbf{x})$ must be 1, we have

$$D_{KL}(\gamma_2 \parallel \gamma_1) = \frac{1}{2} \log \frac{\det \Sigma_1}{\det \Sigma_2} + \frac{1}{2} \int_{\mathbb{R}^N} [\mathbf{x}^T \Sigma_1^{-1} \mathbf{x} - \mathbf{x}^T \Sigma_2^{-1} \mathbf{x}] \rho_2(\mathbf{x}) dx. \quad (4.51)$$

On examining the third term, we can diagonalize $\Sigma_2 = V\Lambda V^T$. Letting $\boldsymbol{\xi} = V^T \mathbf{x}$ and using that the covariance matrices are symmetric-positive-definite gives

$$\int_{\mathbb{R}^N} \mathbf{x}^T \Sigma_2^{-1} \mathbf{x} \rho_2(\mathbf{x}) dx = \int_{\mathbb{R}^N} \boldsymbol{\xi}^T \boldsymbol{\xi} \frac{1}{(2\pi)^{N/2} \sqrt{\det \Lambda}} e^{-\boldsymbol{\xi}^T \Lambda \boldsymbol{\xi} / 2} d\boldsymbol{\xi} \quad (4.52)$$

Since Λ is diagonal, this integral can be split into N integrals

$$\int_{\mathbb{R}^N} \mathbf{x}^T \Sigma_2^{-1} \mathbf{x} \rho_2(\mathbf{x}) dx = \frac{1}{\sqrt{2\pi\lambda_1}} \int_{\mathbb{R}} \dots \frac{1}{\sqrt{2\pi\lambda_N}} \int_{\mathbb{R}} \left(\sum_{n=1}^N \xi_n^2 \right) \prod_{n=1}^N e^{-\lambda_n \xi_n^2 / 2} d\boldsymbol{\xi}. \quad (4.53)$$

Using that for a mean-zero Gaussian distribution $\mathbb{E}[X^2] = 1$ gives

$$\int_{\mathbb{R}^N} \mathbf{x}^T \Sigma_2^{-1} \mathbf{x} \rho_2(\mathbf{x}) dx = \sum_{n=1}^N 1 = N. \quad (4.54)$$

We can apply a similar approach to the second term. Diagonalizing $\Sigma_1 = U\tilde{\Lambda}U^T$ and defining $\boldsymbol{\eta} = U^T \mathbf{x}$ we have

$$\int_{\mathbb{R}^N} \mathbf{x}^T \Sigma_1^{-1} \mathbf{x} \rho_2(\mathbf{x}) dx = \int_{\mathbb{R}^N} \boldsymbol{\eta}^T \tilde{\Lambda}^{-1} \boldsymbol{\eta} \frac{1}{(2\pi)^{N/2} \sqrt{\det \Sigma_2}} \exp\left(\frac{1}{2} \boldsymbol{\eta}^T U^T \Sigma_2^{-1} U \boldsymbol{\eta}\right) d\boldsymbol{\eta} \quad (4.55)$$

This can be seen as the expectation value of $\eta_1^2 / \tilde{\lambda}_1 + \dots + \eta_N^2 / \tilde{\lambda}_N$ under the Gaussian distribution with mean zero and covariance matrix $U^T \Sigma_2 U$. This gives

$$\int_{\mathbb{R}^N} \mathbf{x}^T \Sigma_1^{-1} \mathbf{x} \rho_2(\mathbf{x}) dx = \text{tr}\left(\tilde{\Lambda} U^T \Sigma_2^{-1} U\right). \quad (4.56)$$

Using the properties of the trace operator for matrices we can rewrite this in terms of the original covariance matrices:

$$\int_{\mathbb{R}^N} \mathbf{x}^T \Sigma_1^{-1} \mathbf{x} \rho_2(\mathbf{x}) dx = \text{tr}(\Sigma_1 \Sigma_2^{-1}). \quad (4.57)$$

Combining the above results yields the desired result. □

4.5.2 Gaussian Fields

To build an analogous formula to (4.48) for Gaussian fields, it is important to examine the subtlety involved when dealing with an operator on an infinite dimensional Hilbert space. This problem is examined at length in [67]. To apply this result, we first need to rigorously define the determinant and trace of these covariance operators.

Definition 4.11. Let \mathcal{H} be a Hilbert space and $\mathcal{C} : \mathcal{H} \rightarrow \mathcal{H}$ a self-adjoint linear operator, which admits an eigendecomposition (λ_i, ϕ_i) with $\lambda_i \in \mathbb{R}$ and $\phi_i \in \mathcal{H}$. Then the **trace** of \mathcal{C} is

$$\mathrm{tr}(\mathcal{C}) = \sum_{i=1}^{\infty} \lambda_i. \quad (4.58)$$

We say the operator \mathcal{C} is **Trace class** provided this sum is finite. In addition, we define the **extended trace** operator on $\mathcal{C} + \delta I$ by

$$\mathrm{tr}_X(\mathcal{C} + \delta I) = \mathrm{tr}(\mathcal{C}) + \delta, \quad (4.59)$$

where I is the identity operator.

The regularization-like parameter, δ , is used to enable the operators to be modified to ensure values like determinants work appropriately. To that end, [67] defines the extended determinant.

Definition 4.12. Let \mathcal{H} be a Hilbert space and \mathcal{C} a self-adjoint linear operator on \mathcal{H} with eigendecomposition (λ_i, ϕ_i) . The **extended determinant** of \mathcal{C} is

$$\det_X(\mathcal{C} + \delta I) = \exp(\mathrm{tr}_X[\log(\mathcal{C} + \delta I)]). \quad (4.60)$$

In addition, it can be shown

$$\mathrm{tr}_X[\log(\mathcal{C} + \delta I)] = \sum_{i=1}^{\infty} \log(\lambda_i + \delta). \quad (4.61)$$

Thus, the value of δ can be chosen strategically to ensure this extended determinant is finite, even for operators whose unregularized determinant is infinite. Continuing, [67] defines a comparative determinant between two regularized operators. Let \mathcal{C} and \mathcal{B} be two self-adjoint operators on the sample Hilbert space. Define $D_{\log\det}$ by

$$\begin{aligned} D_{\log\det}[\mathcal{C} + \delta I, \mathcal{B} + \beta I] := & \left(\frac{\delta}{\beta} - 1\right) \log\left(\frac{\delta}{\beta}\right) + \mathrm{tr}_X[(\mathcal{B} + \beta I)^{-1}(\mathcal{C} + \delta I) - I] \\ & - \frac{\delta}{\beta} \log(\det_X[(\mathcal{B} + \beta I)^{-1}(\mathcal{C} + \delta I)]). \end{aligned} \quad (4.62)$$

Notice that in the case of the same regularization, $\delta = \beta$, the first term vanishes.

Using the above definitions and following [67] we define the relative entropy between two Gaussian fields. Let \mathcal{H} be a Hilbert space with inner product $\langle \cdot, \cdot \rangle$. Let $\mathcal{C}_1, \mathcal{C}_2$ be self-adjoint linear operators on \mathcal{H} , and let $\mu_1, \mu_2 \in \mathcal{H}$. We associate two Gaussian fields, $X_i \sim \mathcal{N}(\mu_i, \mathcal{C}_i)$ for $i = 1, 2$ with the aforementioned objects, and for each field, associate measures γ_i on \mathcal{H} . Let $\delta \in \mathbb{R}$ be a regularization parameter, and $\tilde{\gamma}_i^{(\delta)}$ be the measure associated with the Gaussian field $\mathcal{N}(\mu_i, \mathcal{C}_i + \delta I)$. Then the relative entropy between the $\tilde{\gamma}_i^{(\delta)}$ is

$$D_{KL} \left(\tilde{\gamma}_1^{(\delta)} \parallel \tilde{\gamma}_2^{(\delta)} \right) = \frac{1}{2} \langle \mu_1 - \mu_2, (\mathcal{C}_2 + \delta I)^{-1} (\mu_1 - \mu_2) \rangle + \frac{1}{2} D_{\log \det} [\mathcal{C}_1 + \delta I, \mathcal{C}_2 + \delta I]. \quad (4.63)$$

The regularization parameters used in the above formulations are employed so that the extended determinants are well-defined and so that the operator inverses exist. However, for positive-definite linear operators, these inverses exist for $\delta = 0$ due to the positivity of the eigenvalues. Therefore, for two positive-definite, self-adjoint linear operators $\mathcal{C}_1, \mathcal{C}_2$, we can safely define the relative entropy between the associated Gaussian measures γ_1, γ_2 by

$$D_{KL} (\gamma_1 \parallel \gamma_2) = \frac{1}{2} \langle \mu_1 - \mu_2, \mathcal{C}_2^{-1} (\mu_1 - \mu_2) \rangle + \frac{1}{2} D_{\log \det} [\mathcal{C}_1, \mathcal{C}_2]. \quad (4.64)$$

4.5.3 Example Relative Entropy Between Two Gaussian Fields

Consider two mean-zero Gaussian fields with covariance operators like those in (3.55). In particular, let $\alpha = 1$, so the scaling is the same, but consider the case where the two operators have different correlation lengths.

Let X_i have correlation length ℓ_i for $i = 1, 2$. With each X_i , associate the Gaussian measure γ_i . Since both fields are mean-zero,

$$D_{KL} (\gamma_1 \parallel \gamma_2) = \frac{1}{2} D_{\log \det} [\mathcal{C}_1, \mathcal{C}_2]. \quad (4.65)$$

Since the regularization parameters are equal (and both zero), we have

$$D_{\log \det} [\mathcal{C}_1, \mathcal{C}_2] = \text{tr}_X [\mathcal{C}_2^{-1} \mathcal{C}_1 - I] - \log (\det_X [\mathcal{C}_2^{-1} \mathcal{C}_1]). \quad (4.66)$$

The second term can be written as

$$\log (\det_X [\mathcal{C}_2^{-1} \mathcal{C}_1]) = \operatorname{tr}_X [\log (\mathcal{C}_2^{-1} \mathcal{C}_1)]. \quad (4.67)$$

Therefore the relative entropy can be determined by examining the spectrum of the operator $\mathcal{C}_2^{-1} \mathcal{C}_1$. Recall from Chapter 3 that both \mathcal{C}_1 and \mathcal{C}_2 will share the same eigenfunctions, and only the eigenvalues will differ. Consider the eigenvalue problem for each operator:

$$\mathcal{C}_i \phi = \lambda^{(i)} \phi. \quad (4.68)$$

Applying the inverse of \mathcal{C}_2 yields the following relation

$$\mathcal{C}_2 \phi = \lambda^{(2)} \phi \implies \mathcal{C}_2^{-1} \phi = \frac{1}{\lambda^{(2)}} \phi. \quad (4.69)$$

Therefore, applying \mathcal{C}_2^{-1} to the eigenvalue problem for \mathcal{C}_1 yields

$$\mathcal{C}_1 \phi = \lambda^{(1)} \phi \quad (4.70)$$

$$\mathcal{C}_2^{-1} \mathcal{C}_1 \phi = \lambda^{(1)} \mathcal{C}_2^{-1} \phi \quad (4.71)$$

$$= \frac{\lambda^{(1)}}{\lambda^{(2)}} \phi. \quad (4.72)$$

With the spectrum of $\mathcal{C}_2^{-1} \mathcal{C}_1$, we can compute the relative entropy between the two distributions.

$$D_{KL} (\gamma_1 \parallel \gamma_2) = \frac{1}{2} \left[\sum_{j,k,m} \left(\frac{\lambda_{j,k,m}^{(1)}}{\lambda_{j,k,m}^{(2)}} - 1 \right) - \sum_{j,k,m} \log \left(\frac{\lambda_{j,k,m}^{(1)}}{\lambda_{j,k,m}^{(2)}} \right) \right]. \quad (4.73)$$

In the above expression, we use $\sum_{j,k,m}$ to indicate

$$\sum_{j,k,m} \dots = \sum_{j=1}^4 \sum_{k=1}^N \sum_{m=1}^N \dots \quad (4.74)$$

For convenience, we recall the eigenvalues for the aforementioned covariance operators with correlation length ℓ and $\alpha = 1$:

$$\lambda_{j,k,m} = \frac{\ell^2}{1 + 4\pi^2 \ell^2 (k^2 + m^2)}, \quad j = 1, 2, 3, 4; k, m \in \{1, 2, \dots, N\}. \quad (4.75)$$

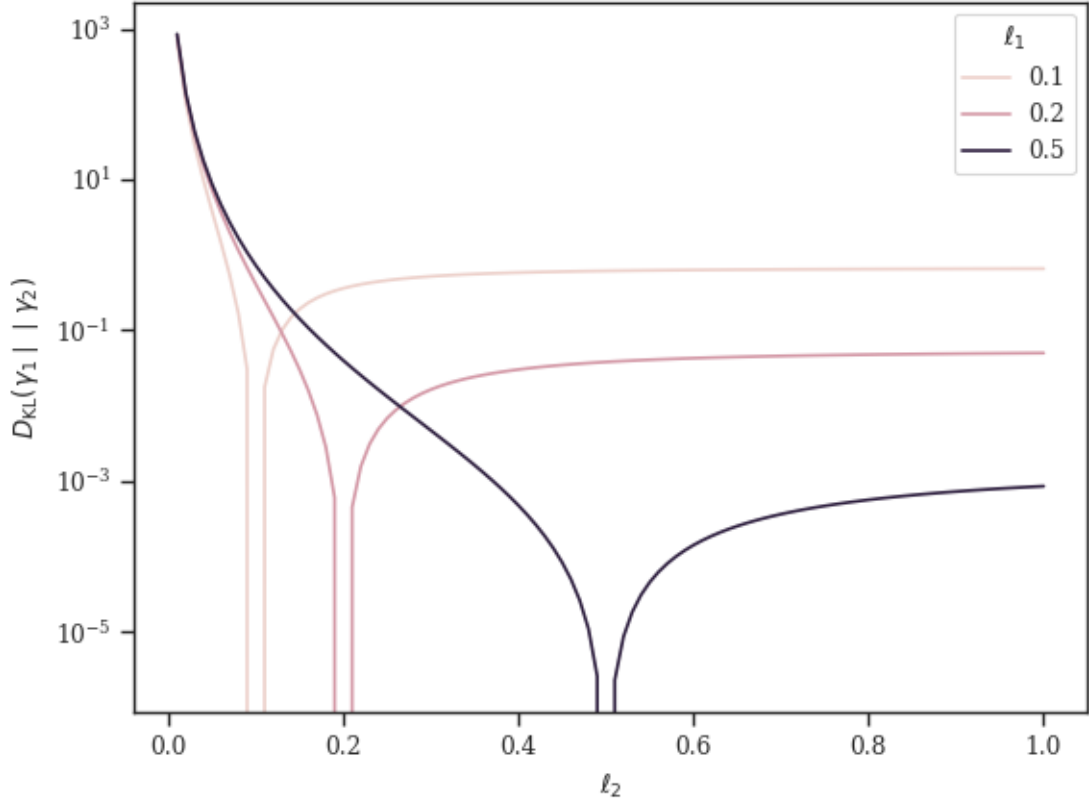


Figure 4.1: Relative entropy between two Gaussian fields of the form (3.55), in which both are mean-zero, but have differing correlation lengths. For regularity, we take $\alpha = 1$.

This is a finite sum and as a result we know the relative entropy between these two fields is well defined. Figure 4.1 shows the relative entropy between two mean-zero Gaussian fields over varying correlation lengths. From this figure, it is possible to determine possible values of the alternative correlation length, for which the bounds in (4.40) can be safely applied.

4.5.4 Log Normal Fields

Consider the relative entropy between two log-normal random fields $Y \sim \nu$ and $\tilde{Y} \sim \tilde{\nu}$. Both fields can be written as transformations of Gaussian random fields

according to

$$Y(x) = e^{X(x)}, \quad \tilde{Y}(x) = e^{\tilde{X}(x)}. \quad (4.76)$$

To determine the relative entropy between these two distributions, we consider only the finite-dimensional version. That is, the KLE provides a framework with which we can associate $X \leftrightarrow \mathbf{Z}$ with $\mathbf{Z} \in \mathbb{R}^N$, and similarly for \tilde{X} . This vector \mathbf{Z} will come from a Gaussian distribution with measure γ . Furthermore, in finite dimensions, this admits a PDF ρ_Z on \mathbb{R}^N . Thus we consider an invertible function $f : \mathbb{R}^N \rightarrow S$, with $Y = f(\mathbf{Z}) \sim \nu$, and similarly for \tilde{Y} .

Proposition 4.1. *Let $\mathbf{Z}, \tilde{\mathbf{Z}} \in \mathbb{R}^N$ be two Gaussian vectors, with associated Gaussian measures γ and $\tilde{\gamma}$. Let $f : \mathbb{R}^N \rightarrow S$ be a measurable function, and define $Y = f(\mathbf{Z})$ and $\tilde{Y} = f(\tilde{\mathbf{Z}})$. Associate with the distributions of Y and \tilde{Y} the measures $\nu, \tilde{\nu}$. Then*

$$D_{KL}(\tilde{\nu} \parallel \nu) = D_{KL}(\tilde{\gamma} \parallel \gamma). \quad (4.77)$$

Proof. By the definition of relative entropy,

$$D_{KL}(\tilde{\nu} \parallel \nu) = \begin{cases} \int_S \log\left(\frac{d\tilde{\nu}}{d\nu}\right) d\tilde{\nu} & \tilde{\nu} \ll \nu \\ \infty & \text{otherwise} \end{cases}. \quad (4.78)$$

Without loss of generality, we need only consider the case $\tilde{\nu} \ll \nu$. By construction, $\nu, \tilde{\nu}$ are absolutely continuous with respect to the Lebesgue measure, and so admit PDFs $\rho_Y, \rho_{\tilde{Y}}$ respectively. The relative entropy then reads

$$D_{KL}(\tilde{\nu} \parallel \nu) = \int_S \log\left(\frac{\rho_{\tilde{Y}}(y)}{\rho_Y(y)}\right) \rho_{\tilde{Y}}(y) dy. \quad (4.79)$$

Since $Y = f(\mathbf{Z})$, we can make the change of variables $y = f(\mathbf{z})$,

$$D_{KL}(\tilde{\nu} \parallel \nu) = \int_{\mathbb{R}^N} \log\left(\frac{\rho_{\tilde{Y}}(f(\mathbf{z}))}{\rho_Y(f(\mathbf{z}))}\right) \rho_{\tilde{Y}}(f(\mathbf{z})) |Jf| dz, \quad (4.80)$$

where $|Jf|$ is the Jacobian of f .

Next, we know that $\mathbb{P}(Y \in B) = \mathbb{P}(f(\mathbf{Z}) \in B) = \mathbb{P}(\mathbf{Z} \in f^{-1}(B))$, where $f^{-1}(B)$ is the pre-image of B , for all $B \subset S$. Therefore

$$\int_B \rho_Y(y) dy = \int_{f^{-1}(B)} \rho_Y(f(\mathbf{z})) |Jf| dz = \int_{f^{-1}(B)} \rho_Z(\mathbf{z}) dz, \quad (4.81)$$

where ρ_Z is the PDF for the variable \mathbf{Z} . As this holds for all $B \subset S$, we have $\rho_Y(f(\mathbf{z}))|Jf| = \rho_Z(\mathbf{z})$. The same can be shown for \tilde{Y} , therefore

$$D_{KL}(\tilde{\nu} \parallel \nu) = \int_{\mathbb{R}^N} \log\left(\frac{\rho_{\tilde{Z}}(\mathbf{z})}{\rho_Z(\mathbf{z})}\right) \rho_{\tilde{Z}}(\mathbf{z}) d\mathbf{z} = D_{KL}(\tilde{\gamma} \parallel \gamma). \quad (4.82)$$

□

4.5.5 Weibull Fields

As a next step, we consider the relative entropy between two Weibull fields. Recall that a Weibull field with shape parameter κ can be written as a transformation of two Gaussian fields by

$$W(x) = \mu(x) \frac{((X_1(x))^2 + (X_2(x))^2)^{1/\kappa}}{2\Gamma(1 + 1/\kappa)}. \quad (4.83)$$

We consider the case of a finite-dimensional problem. Recall from Chapter 3 that a Gaussian field can be approximated by a finite-dimensional Gaussian vector through the KLE.

By construction, both Gaussian fields in the Weibull construction are i.i.d. Therefore we know their respective Gaussian vectors will admit the same diagonalization. To that end, we consider a Gaussian vector $\mathbf{X} \sim \mathcal{N}(\mathbf{0}, \Sigma)$ in \mathbb{R}^N . Since the covariance matrix, Σ is symmetric and positive definite, it admits an eigendecomposition of the form

$$\Sigma = V\Lambda V^T, \quad (4.84)$$

where Λ is a diagonal matrix of eigenvalues, and V is a unitary matrix. A sample for \mathbf{X} can be drawn by taking a standard Gaussian vector, $\mathbf{Z} \sim \mathcal{N}(\mathbf{0}, I)$ and multiplying by Σ :

$$\mathbf{X} = \Sigma\mathbf{Z} = V\Lambda V^T\mathbf{Z}. \quad (4.85)$$

The vector \mathbf{Z} has $Z_j \sim \mathcal{N}(0, 1)$ i.i.d. for $j = 1, 2, \dots, N$.

In an analogous argument, for the Weibull vector, we can consider the random variable defined by

$$\mathbf{U} = \frac{1}{2\Gamma(1 + 1/\kappa)} (\mathbf{Z}_1^2 + \mathbf{Z}_2^2)^{1/\kappa}, \quad (4.86)$$

which is a vector of i.i.d. Weibull variables with shape parameter κ . We wish to exploit the fact the components of \mathbf{U} are independent.

Consider the case of two Weibull variables, \mathbf{W}_1 and \mathbf{W}_2 . In the case that the shape parameters of each Weibull are identical, referring to Proposition 4.1 enables us to compute the relative entropy between the Weibulls by deferring to the underlying Gaussian fields.

Instead, if the underlying Gaussian fields are the same and the shape parameters of the two Weibull distributions are different, we can analyze their analogous diagonalized variants: \mathbf{U}_1 and \mathbf{U}_2 . While there is no simple way to compute \mathbf{W}_i from \mathbf{U}_i , it is possible to get an idea of the limitations and behavior of the relative entropy when applied to Weibull variables.

4.5.5.1 Relative Entropy Between Univariate Weibulls

Recall that for a univariate Weibull variable, its PDF is given by

$$\rho_W(x; \lambda, \kappa) = \begin{cases} \frac{\kappa}{\lambda} \left(\frac{x}{\lambda}\right)^{\kappa-1} e^{-(x/\lambda)^\kappa} & x \geq 0 \\ 0 & x < 0 \end{cases}. \quad (4.87)$$

Proposition 4.2. *Let W_1, W_2 be two scalar Weibull variables, with scaling λ (shared between them) and differing shape parameters k_1, k_2 respectively. Let the probability measures associated with each Weibull be ω_1, ω_2 . Additionally, define $r = k_2/k_1$. Then the relative entropy $D_{KL}(\omega_1 \parallel \omega_2)$ is given by a function $D(r)$, given as*

$$D_{KL}(\omega_1 \parallel \omega_2) = D(r) := -\log r - \gamma(1 - r) - 1 + \Gamma(1 + r), \quad (4.88)$$

where $\Gamma(\cdot)$ is the Gamma function and $\gamma \approx 0.577$ is Euler's constant.

Proof.

$$D_{KL}(\omega_1 \parallel \omega_2) = \int_0^\infty \log \left(\frac{k_1 x^{k_1-1} e^{-x^{k_1}}}{k_2 x^{k_2-1} e^{-x^{k_2}}} \right) k_1 x^{k_1-1} e^{-x^{k_1}} dx. \quad (4.89)$$

Let $u = x^{k_1}$, then

$$D_{KL}(\omega_1 \parallel \omega_2) = \int_0^\infty \log \left(\frac{k_1}{k_2} \frac{uu^{-1/k_1}}{u^{k_2/k_1}u^{-1/k_1}} \frac{e^{-u}}{e^{-u^{k_2/k_1}}} \right) e^{-u} du. \quad (4.90)$$

Expanding the log, we see

$$D_{KL}(\omega_1 \parallel \omega_2) = \int_0^\infty \left[\log \frac{k_1}{k_2} + \log u - \frac{k_1}{k_2} \log u - u + u^{k_2/k_1} \right] e^{-u} du. \quad (4.91)$$

Evaluating this term-by-term yields

$$D_{KL}(\omega_1 \parallel \omega_2) = \log \frac{k_1}{k_2} - \gamma \left(1 - \frac{k_2}{k_1} \right) - 1 + \Gamma \left(1 + \frac{k_2}{k_1} \right), \quad (4.92)$$

where $\gamma \approx 0.577$ is Euler's constant. Thus, making the substitution $r = k_2/k_1$ gives the desired result. \square

A plot of the relative entropy can be seen in Figure 4.2. This shows how close the ratio of the shape parameters of two Weibull variables needs to be to apply the bounds in (4.40).

Next, we consider the case where both the shape parameters and the scaling parameters (λ) are different for each Weibull. In the context of a random vector, this corresponds to when the underlying Gaussians differ. By construction, the scaling parameters λ in the Weibull are equal to the eigenvalue of the covariance matrix defining the underlying Gaussian. A similar argument can be employed, showing that the vector case can still be returned to the scalar case.

Proposition 4.3. *Let W_1, W_2 be two scalar Weibull variables with scaling parameters λ_1, λ_2 and shape parameters k_1, k_2 respectively. Let the probability measures for each variable be ω_1, ω_2 for W_1, W_2 respectively. Then*

$$D_{KL}(\omega_1 \parallel \omega_2) = D(r) + 2D_{KL}(\gamma_1 \parallel \gamma_2), \quad (4.93)$$

where γ_i is the probability measure for a Gaussian variable $X_i \sim \mathcal{N}(0, \lambda_i)$, and $D(r)$ is given in (4.88).

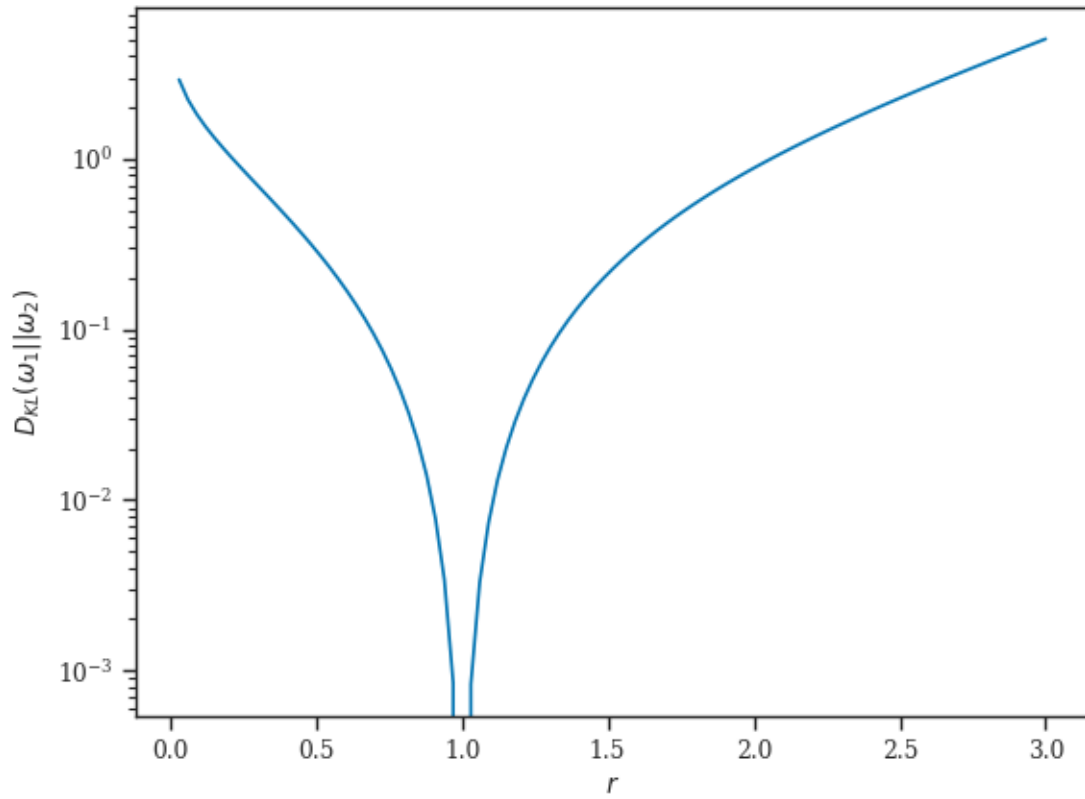


Figure 4.2: Log plot of the relative entropy between two scalar Weibull variables. When $r = 1$, the shape parameters of the two Weibull variables are equal, and the relative entropy drops to zero.

Proof. First, we expand the relative entropy in terms of the respective PDFs

$$D_{KL}(\omega_1 \parallel \omega_2) = \int_0^\infty \log\left(\frac{\rho_W(x; \lambda_1, k_1)}{\rho_W(x; \lambda_2, k_2)}\right) \rho_W(x; \lambda_1, k_1) dx. \quad (4.94)$$

Note that the argument of the log can be rearranged to

$$\frac{\rho_W(x; \lambda_1, k_1)}{\rho_W(x; \lambda_2, k_2)} = \frac{\rho_W(x; \lambda_1, k_1)}{\rho_W(x; \lambda_1, k_2)} \frac{\rho_W(x; \lambda_1, k_2)}{\rho_W(x; \lambda_2, k_2)}. \quad (4.95)$$

Therefore the relative entropy can be split to

$$D_{KL}(\omega_1 \parallel \omega_2) = \int_0^\infty \left[\log\left(\frac{\rho_W(x; \lambda_1, k_1)}{\rho_W(x; \lambda_1, k_2)}\right) + \log\left(\frac{\rho_W(x; \lambda_1, k_2)}{\rho_W(x; \lambda_2, k_2)}\right) \right] \rho_W(x; \lambda_1, k_1) dx. \quad (4.96)$$

The first term becomes $D(r)$ as by Proposition 4.2. The second term is the same Weibull transformation of two Gaussian variables with different variances. The variances of each Gaussian are λ_1, λ_2 by the Weibull construction. Applying Proposition 4.1 yields the desired result. \square

4.5.5.2 Relative Entropy Between Weibull and Log Normal Variables

Next, we consider the case that the nominal model is a Log-Normal field, while the alternative model is a Weibull field. This is the case represented in the examples in later chapters of this thesis. We primarily use a Log-Normal field for the random critical yield stress because of the ease of sampling. However, it has been demonstrated that Weibull fields may better capture the variations in true materials [33].

First, we consider the case that the Weibull and log-normal fields rely on the same underlying Gaussian field. As per Chapter 3, this can be truncated to approximate the Gaussian field by a Gaussian vector. Similarly, this enables the Weibull field and log-normal field by a Weibull vector and log-normal vector, respectively. We will examine a scalar case here, noting that this can provide insight into the behavior of the general vector case.

Referring to [79], we can determine the relative entropy between a Weibull and a log-normal univariate distribution.

Proposition 4.4. *Let L be a log-normal variable with $\log L \sim \mathcal{N}(\mu, \sigma^2)$ and W be a Weibull variable with scaling parameter λ and shape parameter k . Let the probability measures for L and W be ℓ and ω respectively. Then*

$$D_{KL}(\omega \parallel \ell) = \log(\sqrt{2\pi}\sigma) + \log k - 1 - \gamma + \frac{1}{2\sigma^2} \left(\left(-\mu + \frac{\gamma}{k} + \log \lambda \right)^2 + \frac{1}{6} \frac{\pi^2}{k^2} \right). \quad (4.97)$$

We suppose the underlying Gaussian has $\mu = 0$ and $\sigma^2 = \lambda$. Note that in order for $\mathbb{E}[L] = \mathbb{E}[W] = 1$, we must have

$$\mu = -\frac{\sigma^2}{2} = -\frac{\lambda}{2}. \quad (4.98)$$

This shift need not occur to the Gaussian variable. Instead, we can conceptualize a log-normal variable as $Y = \alpha e^X$, where α is determined by the value of μ and $\mathbb{E}[X] = 0$. Substituting these values into the result from Proposition 4.4 gives

$$D_{KL}(\omega \parallel \ell) = \frac{1}{2} \log(2\pi\lambda k^2) - 1 - \gamma + \frac{1}{2\lambda} \left(\left(\frac{\lambda}{2} + \frac{\gamma}{k} + \log \lambda \right)^2 + \frac{1}{6} \frac{\pi^2}{k^2} \right) =: R(\lambda, k). \quad (4.99)$$

Consider the problem of choosing k as to minimize R for any given λ . We can do this by fixing λ and applying a minimization procedure for R over various values of k . Once the optimal k value is determined for each λ , we can plot the resulting relative entropy against the value of λ . The results can be seen in Figure 4.3. An important reference value is when the relative entropy is below 1, in which case the asymptotic bounds in (4.40) can be applied safely. As seen in Figure 4.3, this only can occur for a narrow range of λ , and so it is unlikely that the relative entropy between a Weibull and log-normal field with the same underlying Gaussian field will be applicable to the bounds in (4.40).

Next, we consider the case of a Weibull field coming from a different Gaussian field than that of the log-normal field. Setting aside the issue of simultaneous diagonalization, we can ask if it is at all possible for the asymptotic bounds in (4.40) to be applicable. More specifically, we can look at what parameter choices of λ, k can be used to minimize the relative entropy in (4.97). To that end, we consider fixing the

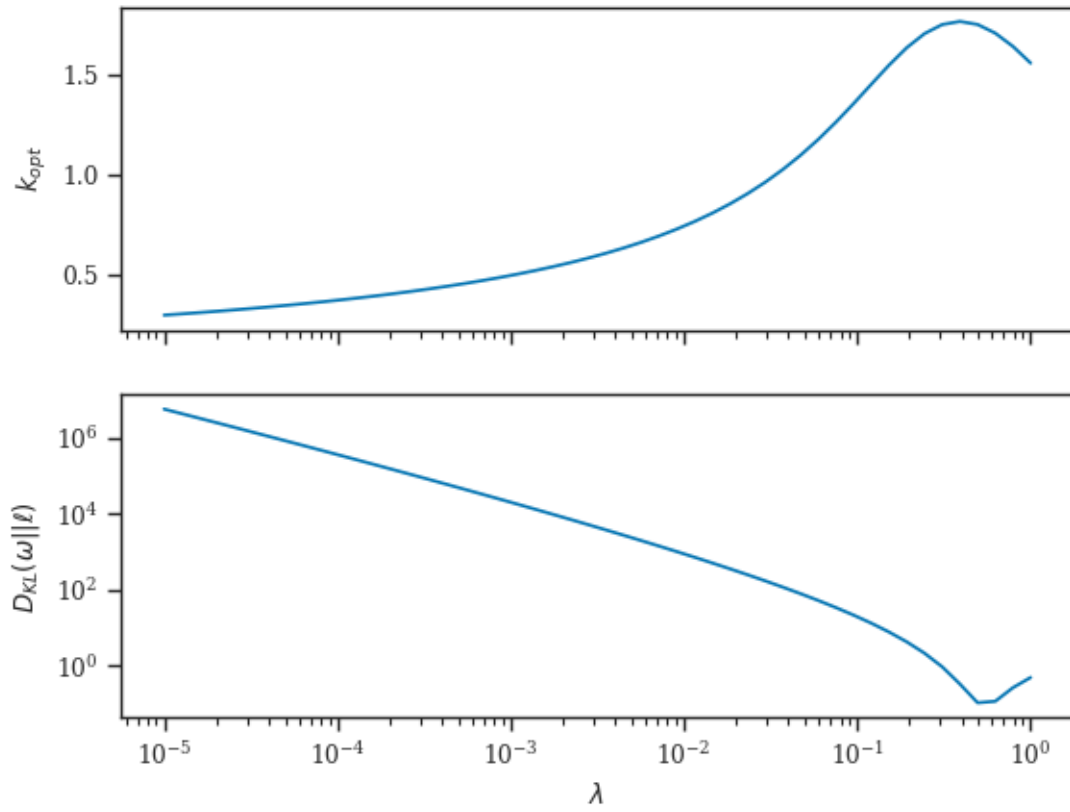


Figure 4.3: Upper: optimal value of k to minimize the relative entropy between a Weibull and log-normal distribution with $\sigma^2 = \lambda$. Lower: minimum relative entropy.

log-normal variable with a mean of 1, as in (4.98), this implies $\mu = -\sigma^2/2$. Therefore, we can fix a value of σ and examine the values of λ and k , which minimize (4.97).

Figure 4.4 shows the optimal choices of λ and k to minimize (4.97), for various values of σ . Based on these values, we can then evaluate the minimum relative entropy. This can be seen in Figure 4.5. Interestingly, the minimum relative entropy is small, nearly constant over σ , and around 0.1. Therefore, it is not impossible for the asymptotic bounds in (4.40) to be applicable to the general case of the alternative model being a Weibull field and the nominal model being log-normal. However, one must be cautious about doing so, as the minimum bounds hover around 0.1, therefore slight changes can lead to a resulting relative entropy to which (4.40) may no longer apply. A direct conversion between the σ values plotted and the eigenvalues, λ_i from diagonalization of a random field can be applied, using that each component in the KLE from Chapter 3 has $\zeta_i \sim \mathcal{N}(0, \lambda_i)$. Therefore, term-by-term the relative entropy between the two fields can be read-off using values $\sigma = \sqrt{\lambda_i}$, where λ_i are the eigenvalues of the respective Gaussian fields.

Moreover, Figure 4.4, shows how λ , the Weibull scale parameter changes with σ . Recall from Chapter 3, that for a Weibull variable built on a Gaussian with variance σ^2 , that $\lambda = \sigma^2$. As a result, Figure 4.4 indicates the eigenvalue of the Gaussian field used to build the Weibull field as a function of the eigenvalue of the nominal model in the log-normal field.

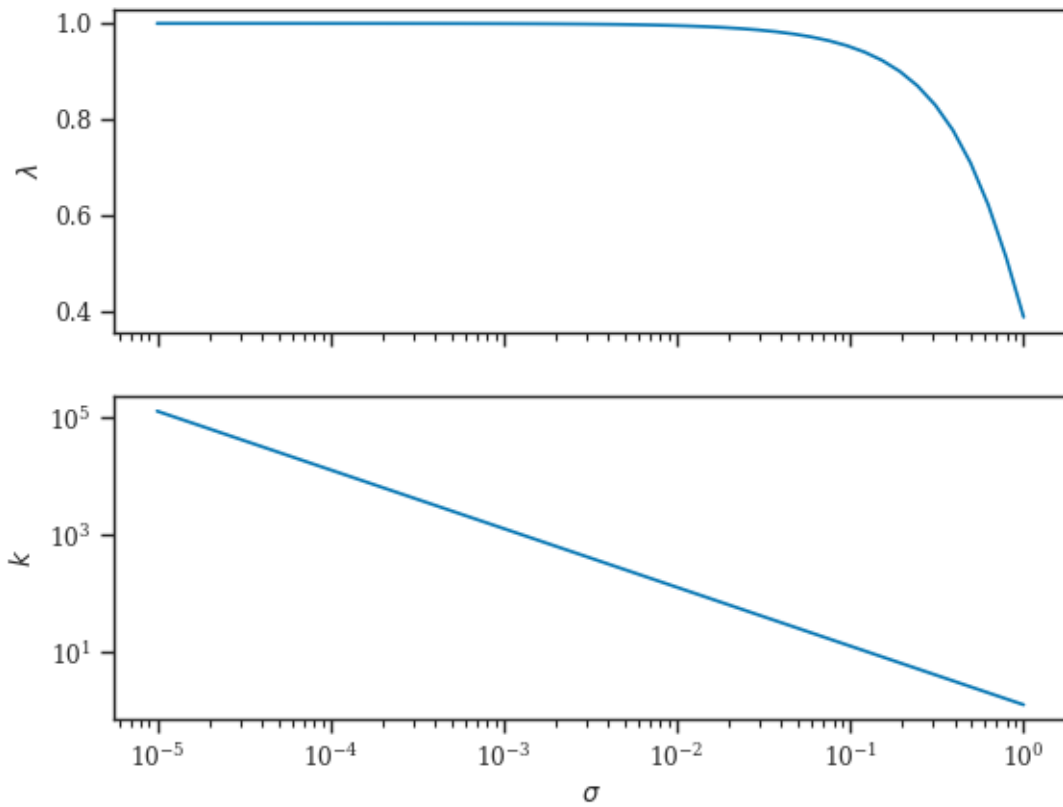


Figure 4.4: Optimal choice for λ and k to minimize the relative entropy in (4.97) with $\mu = -\sigma^2/2$, for various values of σ .

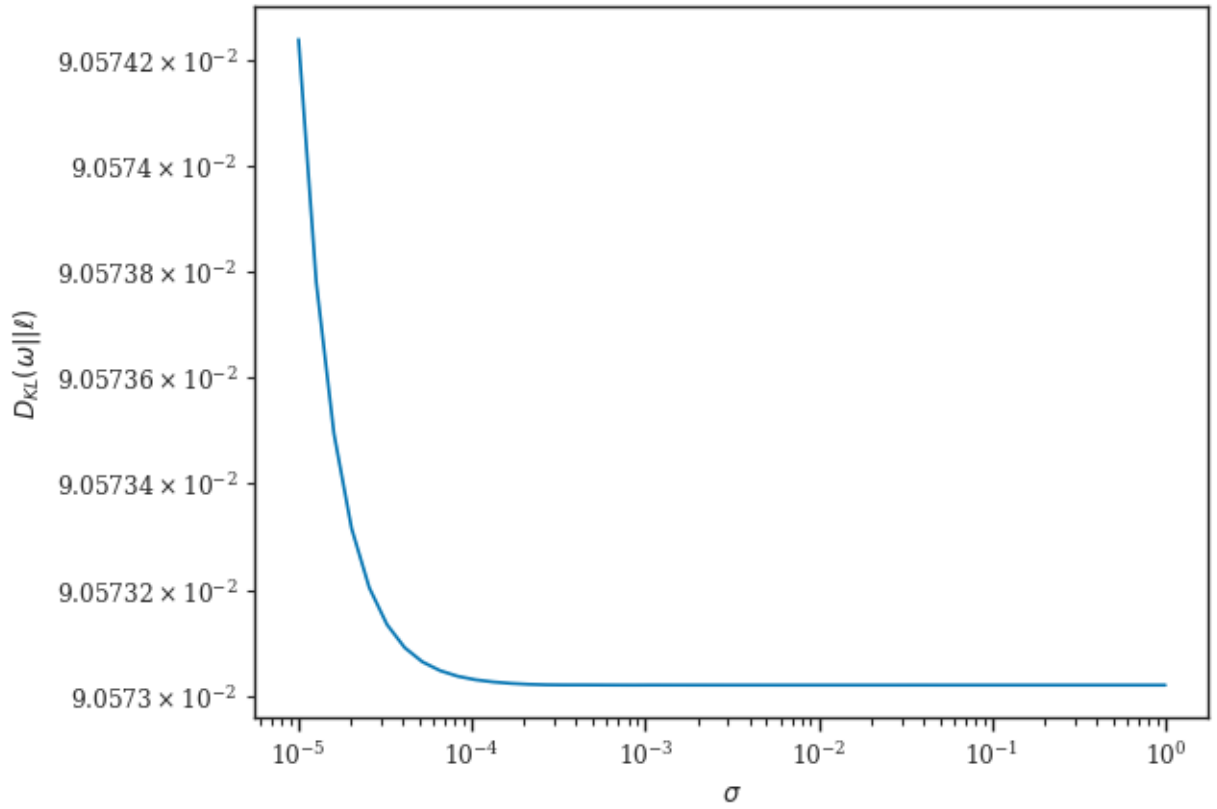


Figure 4.5: Minimum relative entropy between a mean-1 log-normal variable and a Weibull variable, using the parameter values λ, k indicated from Figure 4.4.

Chapter 5

MONTE CARLO SAMPLING FOR SOME QUANTITIES OF INTEREST

5.1 Introduction

We are now in a position to assemble together all of the details discussed in previous chapters to build a pipeline with which to evaluate various quantities of interest for damage mechanics simulations. Chapter 2 describes the methods to build a solution $(\underline{u}, \mathcal{D})$ from a given sample of the critical yield stress, Σ . Chapter 3 provides the tools needed to construct samples of these random yield stress fields in a way that is computationally feasible. Finally, Chapter 4 provides the resources to quantify the uncertainty resulting from the modeling assumptions and the randomness of the critical yield stress.

In each problem discussed in the following sections, we will specify one or more QoIs, Q , which will be extracted from the solution of the damage mechanics problem. We can conceptualize the simulation pipeline by

$$Q = (Q \circ \mathcal{F})(\Sigma), \quad (5.1)$$

where $\mathcal{F} : \Sigma \mapsto (\underline{u}, \mathcal{D})$ and $Q : (\underline{u}, \mathcal{D}) \mapsto Q$.

As discussed in Chapter 4, we will sample from Q using Monte-Carlo (MC) methods. That is, we will generate a collection of samples $\{\Sigma^{(n)}\}$ for $n = 1, 2, \dots, N$. For each sample number, n , we will compute the corresponding $Q^{(n)}$, and apply the methods discussed to the resulting collection $\{Q^{(n)}\}$.

5.2 Expanding Ring and Counting Fragments

In the experiments described by [44, 45, 46], a thin ring of material is accelerated outward in an expanding motion by way of an induced electromagnetic field.

This causes a sudden buildup of stresses within the material and ultimate material failure. When this experiment is done in a lab setting, a sample can shatter into many fragments. Of particular interest is how this shattering happens, how many fragments are created, the relative sizes of these fragments, and the relationship between the rate of expansion applied and the resulting number of fragments.

For this particular problem, we use a mean-1 log-normal random field. The underlying Gaussian field will have a covariance function, $k(x, y)$ defined by

$$\text{Cov}[\log(\Sigma(\underline{x})), \log(\Sigma(\underline{y}))] = k_\ell(\underline{x}, \underline{y}) = \delta \exp\left(\frac{\|\underline{x} - \underline{y}\|^2}{2\ell^2}\right). \quad (5.2)$$

Where δ is a scale factor, and ℓ is the correlation length of the random field. This covariance function induces a covariance operator \mathcal{C}_ℓ , and the resulting random field is given by

$$\log \Sigma \sim \mathcal{N}(\mu(\delta, \ell), \mathcal{C}_\ell). \quad (5.3)$$

Where μ is a constant value chosen so that $\mathbb{E}[\Sigma] \equiv 1$. Because this field does not admit an easily represented eigendecomposition, we instead construct a numerical diagonalization on the finite element space as discussed in Chapter 3.

For this problem, we will be considering a single QoI - the number of fragments into which the ring breaks after it fractures. Let C be the count of the number of fragments. We are examining the mapping $\Sigma \mapsto C$.

5.2.1 Geometry and Boundary Conditions

The domain, Ω , for the expanding ring problem is an annulus with inner radius R , with $0 < R < 1$, and outer radius 1. We represent the inner boundary by Γ_{inner} and the outer boundary by Γ_{outer} ,

$$\Omega = \{\underline{x} \in \mathbb{R}^2 : R < \|\underline{x}\| < 1\}, \quad (5.4)$$

$$\Gamma_{\text{inner}} = \{\underline{x} \in \partial\Omega : \|\underline{x}\| = R\}, \quad (5.5)$$

$$\Gamma_{\text{outer}} = \{\underline{x} \in \partial\Omega : \|\underline{x}\| = 1\}; \quad (5.6)$$

where $\|\cdot\|$ indicates the Euclidean norm. A diagram of this setup can be seen in Figure 5.1.

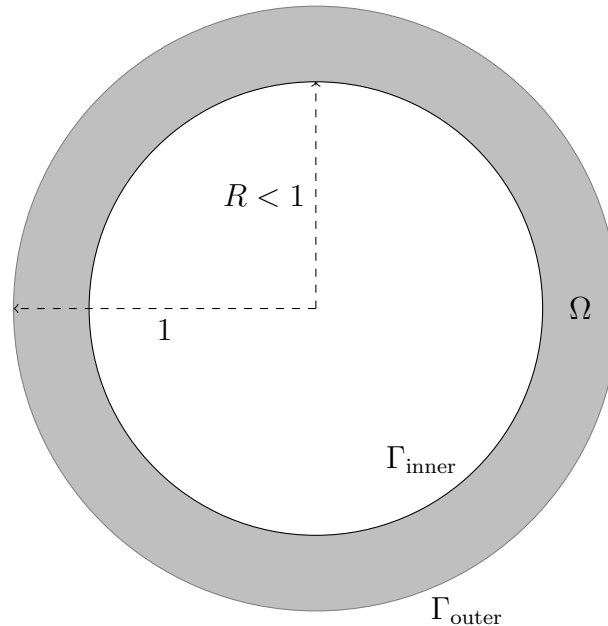


Figure 5.1: Domain and boundaries for the expanding ring problem.

The boundary conditions for the expanding ring problem are a constant speed Dirichlet condition on the inner boundary and a stress-free condition on the outer boundary. Let \underline{n} represent the unit outward normal to the surface $\partial\Omega$. Note that on Γ_{outer} that \underline{n} is simply the unit radial vector, and on Γ_{inner} that \underline{n} is the inward pointing radial vector. The boundary conditions for the expanding ring problem read

$$\underline{u}\Big|_{\Gamma_{\text{inner}}} = -(ct)\underline{n}, \quad (5.7)$$

$$\underline{\underline{\sigma}} \cdot \underline{n}\Big|_{\Gamma_{\text{outer}}} = \underline{0}. \quad (5.8)$$

Where $c > 0$ is a constant expansion speed, and t is time. The damage mechanics problem can be run forward in time using the procedure discussed in Chapter 2 to generate a solution for a given yield stress.

5.2.2 Fragment Counts

For an accurate and reproducible simulation, we need to develop an automated procedure to compute the fragment count that can quickly handle a large number of samples and which agrees with the by-eye count of the fragments for any given sample.

We suppose that the annulus domain is narrow enough that cracks, or continuous areas of $\mathcal{D} = 1$, will proceed mostly along the radial direction from the inner to the outer boundary. To define a crack, we apply the following procedure. Choose an annular segment:

$$A(\phi; \delta\phi) := \{\underline{x} = (r \cos \theta, r \sin \theta) \in \Omega : \phi \leq \theta \leq \phi + \delta\phi\}. \quad (5.9)$$

Where θ is the polar angle of the position \underline{x} . The angle ϕ is the starting polar angle of the segment, and $\delta\phi$ is the width of this segment. We define the damage in each annular segment by

$$\bar{\mathcal{D}}(\phi) = \frac{1}{|A(\phi; \delta\phi)|} \int_{A(\phi; \delta\phi)} \mathcal{D}(\underline{x}, t_{\max}) dx, \quad 0 \leq \phi < 2\pi. \quad (5.10)$$

Where $|A|$ is the area of A . Next, choose a threshold damage level, $d_* \in (0, 1]$. We say a fracture has occurred at angle θ provided there is a local maximum in $\bar{\mathcal{D}}$ at $\phi = \theta$ and $\bar{\mathcal{D}}(\theta) \geq d_*$. The number of cracks is counted by sweeping the values of ϕ through $[0, 2\pi)$. The procedure can be summarized as follows:

$$\mathcal{Q} : (\underline{u}, \mathcal{D}) \mapsto C, \quad (\underline{u}, \mathcal{D}) \mapsto \mathcal{D}(\underline{x}, t_{\max}) \mapsto \bar{\mathcal{D}}(\phi) \mapsto C. \quad (5.11)$$

Since the domain is an annulus, the number of fragments is equal to the number of cracks. A diagram outlining this approach can be seen in Figure 5.2. In it, a sample from the expanding ring is shown with its damage field plotted. An averaging window for $A(\phi, \delta\phi)$ is displayed, indicating the annular segment over which the damage is averaged.

5.2.3 Monte Carlo Sampling

We examine a collection of 1,000 samples for the random field Σ for various values of the correlation length. The forward map and QoI computation are as follows. For each sample $\Sigma^{(n)}$ of the critical yield stress,

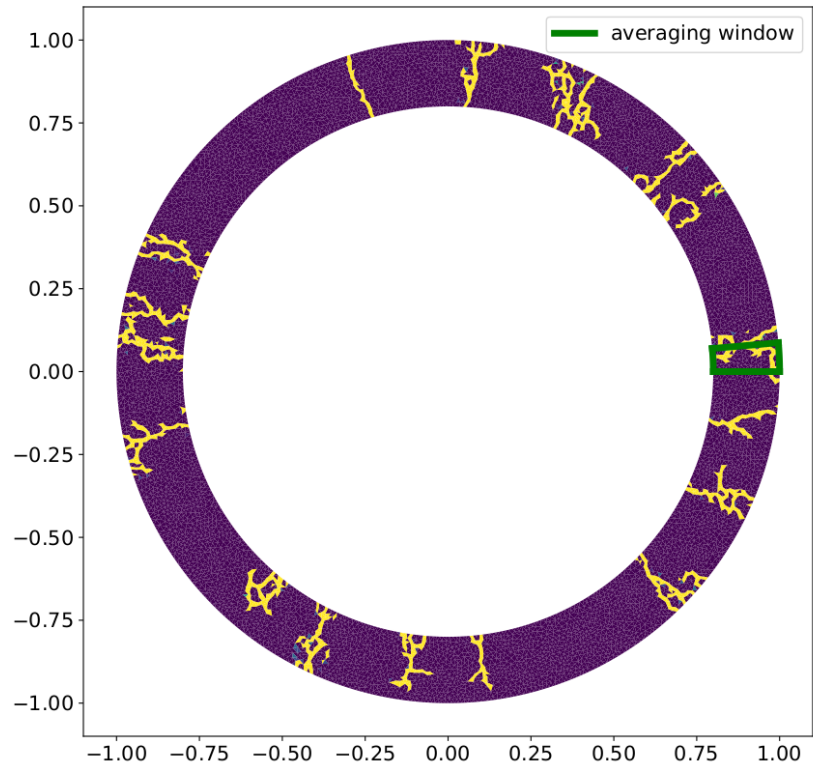


Figure 5.2: A sample of the expanding ring problem with damage field plotted. An annular segment $A(\phi, \delta\phi)$ is highlighted in green and shows its width relative to the sizes of the cracks.

1. Evaluate $(\underline{u}^{(n)}, \mathcal{D}^{(n)}) = \mathcal{F}(\Sigma^{(n)})$
2. Determine the fragment count $C^{(n)} = \mathcal{Q}((\underline{u}^{(n)}, \mathcal{D}^{(n)}))$

We use a shifted-Weibull distribution to fit the resulting number of fragments. The univariate shifted-Weibull distribution has a probability density function (PDF) of the form

$$\rho(x) = \begin{cases} \frac{k}{\lambda} \left(\frac{(x - x_0)}{\lambda} \right)^{k-1} \exp \left(- \left(\frac{(x - x_0)}{\lambda} \right)^k \right) & x > x_0 \\ 0 & x < x_0 \end{cases}. \quad (5.12)$$

For a given collection of observations, $C^{(1)}, \dots, C^{(M)}$, the parameters k, λ, x_0 can be chosen according to the Maximum Likelihood Estimator (MLE), see Chapter 4 for details. It should be noted the fragment count is a discrete variable, while the univariate Weibull distribution is a continuous distribution. This discrepancy can be remedied by building a discrete version of the Weibull distribution by “binning” values:

$$\mathbb{P}(C = m) = p(m) = \int_{m-1/2}^{m+1/2} \rho(x) dx, m \in \mathbb{N}. \quad (5.13)$$

To examine the effect of the correlation length, ℓ , on the fragment count, we ran 1,000 samples of the expanding ring problem for correlation lengths $\ell = 0.01, 0.05, 0.1$ and 0.2 . Applying the above procedure to evaluate the fragment counts, we plot a histogram of these fragment counts for each ensemble of simulations. The fitted Weibull distributions are overlayed on each plot, and their fitted parameters are listed, this can be seen in Figure 5.3.

5.3 One Dimensional Uniaxial Strain

In our paper, [32], after demonstrating the well-posedness of the damage mechanics model in the one-dimensional setting, we examined the stress dynamics of the uniaxial strain problem in the context of varying the correlation length in the random yield stress field. As the correlation length increases, there is a clear increase in the resulting standard deviation in the stress for all time points. Additionally, the uncertain

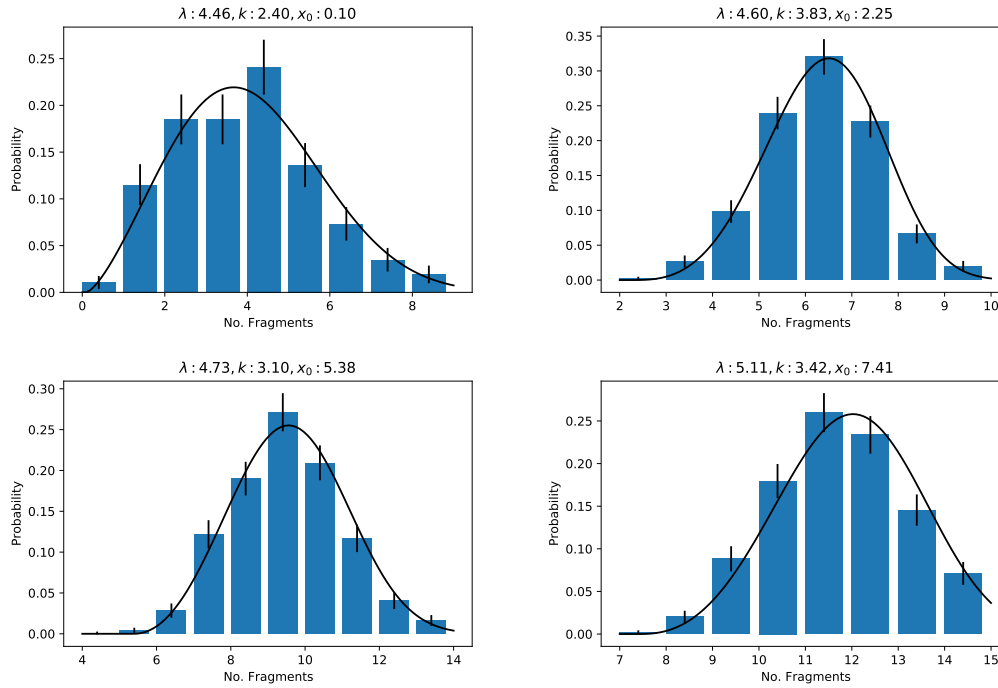


Figure 5.3: Weibull fits on fragment count histograms in the expanding ring problem for various correlation lengths. Upper left: $\ell = 0.01$, upper right: $\ell = 0.05$, lower left: $\ell = 0.1$, and lower right : $\ell = 0.2$. In each plot, the fitted Weibull parameters are listed above, and the black curve indicates the Weibull fit. The vertical black bars indicate a 95% Clopper Pearson confidence interval on each histogram bin.

behavior of the problem due to the yield stress field lends itself well to MC sampling techniques. In building off this work, we next consider the two-dimensional analog of the uniaxial-strain problem.

5.4 Two Dimensional Uniaxial Strain Problem

In this experiment, we consider the uniaxial tensile test. A rectangular segment of material will be approximated as a two-dimensional rectangle that is longer than it is wide. Along the length of the rectangle, the left end will be fixed at zero displacement, and the right end will be pulled uniformly at a constant speed. This sets the total strain along the length of the rectangle at each time. Additionally, the top and bottom of the rectangle will be stress-free by assigning zero Neumann boundary conditions.

For this experiment, there are two QoIs we will examine. The first is the average stress-strain relation. That is, given a value for the strain, we wish to know the resulting stress. Due to the action of the damage variable, we are interested in the relaxation behavior of the material during failure. Additionally, we are interested in the time at which damages begin appearing. Since the damage variable $\mathcal{D}(\underline{x}, t)$ acts as a stochastic process in t , we can consider this time of failure as a stopping time in the random-variable sense. Ultimately, we would like to build a confidence interval for the stress-strain curve over the duration of the experiment and build a probability distribution for when the damage will begin rising.

5.4.1 Domain and Boundary Conditions

The domain for the 2D uniaxial strain problem is a rectangle of length 1 and width $w < 1$. That is

$$\Omega = (0, 1) \times (0, w) \ni \underline{x} = (x, y) \tag{5.14}$$

We split the boundary of the domain into four parts. The bottom, top, left, and right segments:

$$\Gamma_{\text{bottom}} = \{\underline{x} \in \partial\Omega : y = 0\} \quad (5.15)$$

$$\Gamma_{\text{left}} = \{\underline{x} \in \partial\Omega : x = 0\} \quad (5.16)$$

$$\Gamma_{\text{right}} = \{\underline{x} \in \partial\Omega : x = 1\} \quad (5.17)$$

$$\Gamma_{\text{top}} = \partial\Omega \setminus (\Gamma_{\text{bottom}} \cup \Gamma_{\text{left}} \cup \Gamma_{\text{right}}). \quad (5.18)$$

A diagram of this domain can be seen in Figure 5.4.

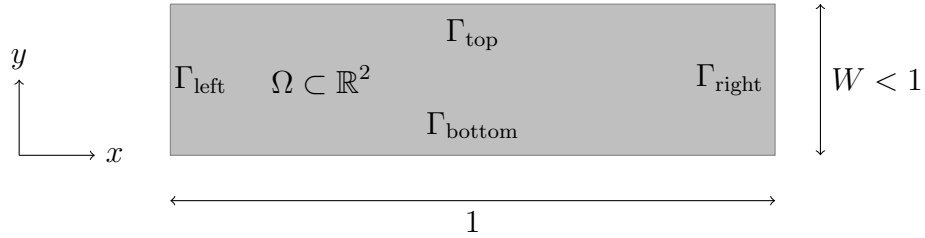


Figure 5.4: Domain and boundaries for the uniaxial strain problem in a rectangle.

The associated boundary conditions for the uniaxial strain problem are Dirichlet conditions on the left and right boundaries and free stress conditions on the top and bottom boundaries:

$$\underline{\underline{\sigma}} \cdot \underline{n} \Big|_{\Gamma_{\text{top}} \cup \Gamma_{\text{bottom}}} = \underline{0}, \quad (5.19)$$

$$\underline{u} \Big|_{\Gamma_{\text{left}}} = \underline{0}, \quad (5.20)$$

$$\underline{u} \Big|_{\Gamma_{\text{right}}} = \underline{r}(t). \quad (5.21)$$

Where $\underline{r}(t)$ is a predetermined time-dependent vector that describes the displacement at the right-hand side of the domain. For this particular problem, we use

$$\underline{r}(t) = ct\mathbf{e}_x. \quad (5.22)$$

Where c is a constant expansion speed and \mathbf{e}_x is the unit vector in the x direction. This is the 2D analog of the uniaxial strain problem discussed in [32]. Using a collection of 100 samples, we use MC sampling to examine the aforementioned QoIs.

5.4.2 Time of First Damage

As discussed above, the damage variable forms a stochastic process over the time evolution of each sample. To this end, we can consider the random variable T , corresponding to the time at which the first non-zero damage values appear, that is

$$T = \inf_{t>0} \{t : \exists \underline{x} \in \Omega \text{ with } \mathcal{D}(\underline{x}, t) > 0\}. \quad (5.23)$$

In this way, the QoI map, \mathcal{Q} , maps the solution $(\underline{u}, \mathcal{D})$ to the aforementioned variable T . The MC sampling then proceeds as

$$T^{(n)} = (\mathcal{Q} \circ \mathcal{F})(\Sigma^{(n)}), n = 1, 2, \dots, N = 100. \quad (5.24)$$

The random variable, T , comes from a continuous distribution. However, our samples will necessarily be discrete due to the numerical method used to solve the problem. Thus a value $T = \tau$ could correspond to any value $T \in [\tau, \tau + \Delta t)$, where Δt is the time step size used in the Generalized- α scheme as described in Chapter 2. Therefore, if we histogram the observed values for $T^{(n)}$, smoothing this histogram should give an idea of the true probability density function for T . This is an instance where a kernel density estimator (KDE) is extremely useful. In Chapter 4, the KDE is explored in more detail. Here we use a Gaussian kernel, with

$$\kappa_h(u) = \frac{1}{h} \kappa_1(u/h) = \frac{1}{h\sqrt{2\pi}} \exp\left(-\frac{u^2}{2h^2}\right). \quad (5.25)$$

In general, the value of h needs to be determined a priori. Using the `scipy.stats` module, this parameter is chosen automatically based on the distribution of the input data.

Using a collection of 100 samples, we generate a KDE for the distribution of T . Moreover, we can generate a cumulative distribution function (CDF), on which we can place Clopper-Pearson confidence bounds. These bounds represent a confidence interval on the probability that the first damage will arise before a given time. These results can be seen in Figures 5.5 and 5.6 respectively.

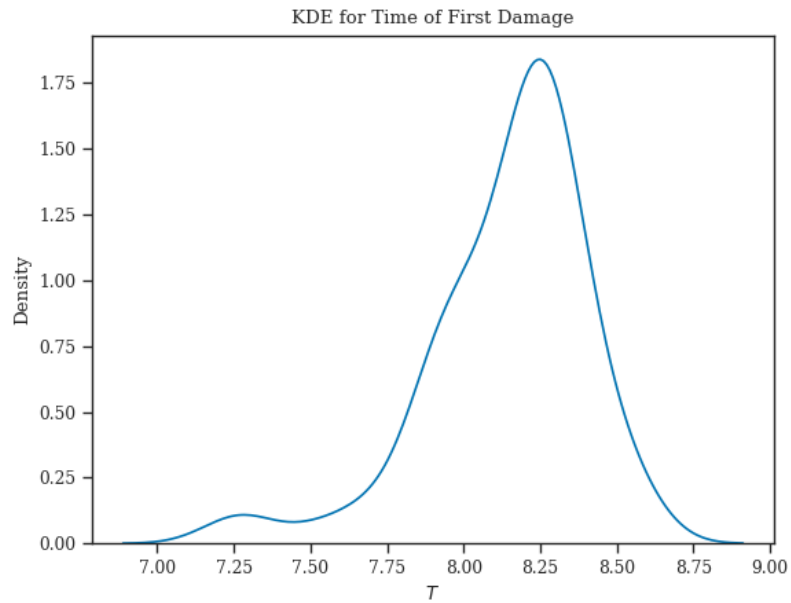


Figure 5.5: KDE for the time of first damage in the constant speed uniaxial strain problem. The KDE represents an approximation to the PDF for this stopping time.

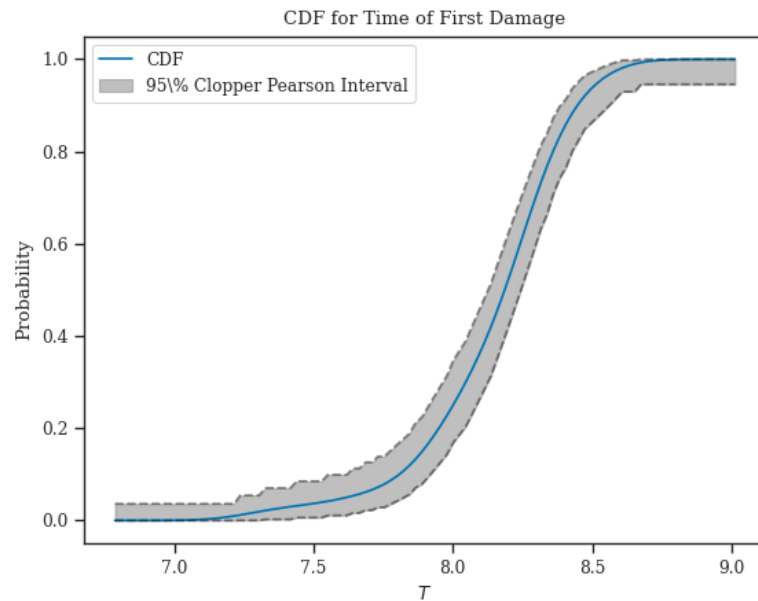


Figure 5.6: CDF for the time of first damage in the constant speed uniaxial strain problem. Also shown is a 95% Clopper-Pearson confidence interval for the CDF, which place bounds on the probability of the stopping time occurring before the specified time.

5.4.3 Stress-Strain Curve

A separate QoI we are interested in is the stress-strain curve. That is, we wish to determine an average relationship, where given a strain value, we can determine the corresponding average stress value. In the problem framework, the strain and stress are tensor-valued, so we want to represent this relationship through scalars.

Because forcing is taking place along the x -axis, we are only concerned with the x -component of the stress-strain curve. Recall that in the problem framework discussed in Chapter 2, the strain and stress values are rank-2 tensors with components σ_{ij} for i, j either 1 or 2, representing the x - and y -components respectively. Because we are only concerned with the x direction, we will use the 11 components of both tensors. This can be written mathematically as follows:

$$\hat{\varepsilon} = \int_{\Omega} \varepsilon_{11} dx \quad (5.26)$$

$$\hat{\sigma} = \int_{\Omega} \sigma_{11} dx = \int_{\Omega} (1 - \mathcal{D})\sigma_{11}^{(L)} dx \quad (5.27)$$

$$(5.28)$$

We are interested in constructing a function \mathcal{S} , with the property

$$\hat{\sigma} = \mathcal{S}(\hat{\varepsilon}). \quad (5.29)$$

It can be shown $\hat{\varepsilon} = ct$, resulting from the Dirichlet boundary conditions. Therefore examining the stress-strain relationship is equivalent to examining the stress evolution over time. By performing the QoI computation pointwise for every time, t , we build a relation $\hat{\sigma} = \hat{\sigma}(t)$. Then by joining these scalar values over all time, we are able to obtain a function $t \mapsto \hat{\sigma}$. By dividing through by the constant expansion speed, it is possible to obtain the stress-strain relationship:

$$\hat{\varepsilon}(t) = ct \mapsto t \mapsto \hat{\sigma}(t). \quad (5.30)$$

Due to the numerical discretization used to solve the problem, we do not have a continuous function $\hat{\sigma}(t)$, and instead have a random vector of the form $\hat{\sigma}_n = \hat{\sigma}(t^n)$. This

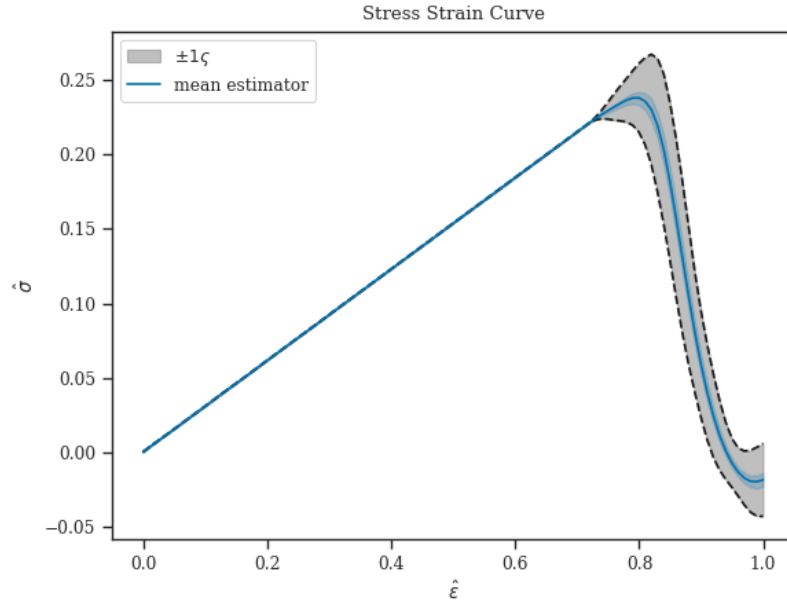


Figure 5.7: Average stress-strain curve for the uniaxial strain problem. Shaded in grey is a $\pm 1\zeta$ interval on the individual sample stress-strain curve. In solid blue is the mean estimator for the stress-strain curve, while in shaded blue is a 95% confidence interval on the estimator itself.

can be remedied by interpolating the resulting nodal stress values over time, using, for instance, a cubic spline to produce a continuous function over time. Using the one-to-one mapping between strain in time, it is then possible to build a continuous function between strain and stress. Using the data from the 100 samples used to examine the stopping time, we plot the stress-strain curve in Figure 5.7.

Recall from Chapter 4 that the asymptotic UQ bounds for a new distribution are directly proportional to the standard deviation of the QoI. Therefore, these results examined for correlation length $\ell = 0.2$ can be generalized to that of other correlation lengths using the results from Chapter 4 which describe the asymptotic UQ bounds and the relative entropy between this random field and that with a different correlation length.

5.5 Notched Uniaxial Stress Problem

In this experiment, we consider a rectangular segment of material undergoing a uniaxial tensile test. In some tests [25], a small notch is removed from part of the material. This notch focuses stresses and resulting damages, resulting in a more concentrated damage distribution and more uniform failure modes.

We consider a two-dimensional rectangle which is longer than it is wide. Along its length, the rectangle is pulled using Neumann boundary conditions. This specifies the stresses at the boundary, simulating a material that is undergoing external forcing. In the center of the top portion of the boundary, a triangular notch is removed to focus high stresses at its tip. Along the top and bottom boundaries, no external forcing is applied, and stress-free conditions are enforced. This is done by applying zero-Neumann conditions to the top and bottom boundaries, including along the boundary of the removed notch.

5.5.1 Domain and Boundary Conditions

The domain for the notched uniaxial stress problem is a rectangle with a small notch cut out of the top portion of the domain. The rectangle is of length 1 and width $w \in (0, 1)$ and pulled along its length. The notch will be an isosceles triangle of width ν and extend to a depth of δ into the rectangular domain, taken from the middle of the top portion of the domain. That is

$$\Omega_{\text{rect}} = (0, 1) \times (0, w) \quad (5.31)$$

$$\Omega_{\text{notch}} = \mathfrak{T}((0.5 - \nu/2, w), (0.5 + \nu/2, w), (0.5, w - \delta)) \quad (5.32)$$

$$\Omega = \Omega_{\text{rect}} \setminus \Omega_{\text{notch}}. \quad (5.33)$$

Where $\mathfrak{T}(A, B, C)$ is a triangle with vertices located at A , B , and C . The basic layout can be seen in Figure 5.8

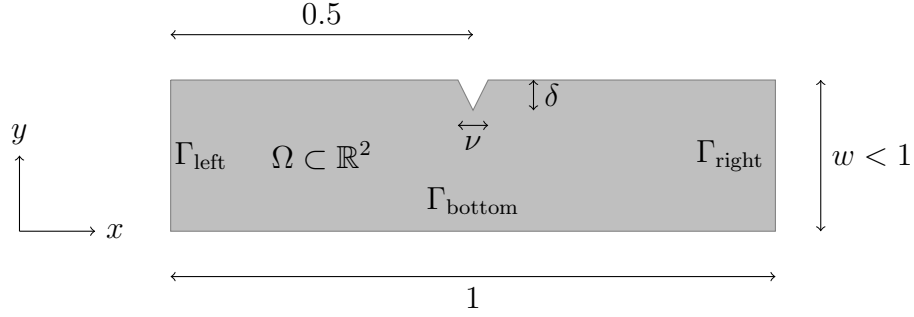


Figure 5.8: Diagram of the domain and boundaries in the notched uniaxial stress problem.

We split the boundary of the domain into four parts. The bottom, top, and left and right segments:

$$\Gamma_{\text{bottom}} = \{\underline{x} \in \partial\Omega : y = 0\} \quad (5.34)$$

$$\Gamma_{\text{left}} = \{\underline{x} \in \partial\Omega : x = 0\} \quad (5.35)$$

$$\Gamma_{\text{right}} = \{\underline{x} \in \partial\Omega : x = 1\} \quad (5.36)$$

$$\Gamma_{\text{top}} = \partial\Omega \setminus (\Gamma_{\text{bottom}} \cup \Gamma_{\text{left}} \cup \Gamma_{\text{right}}). \quad (5.37)$$

The associated boundary conditions for the notched uniaxial stress problem are fixed normal stresses on the left and right boundaries and free stress conditions on the top and bottom boundaries,

$$\underline{\underline{\sigma}} \cdot \underline{\underline{n}} \Big|_{\Gamma_{\text{top}} \cup \Gamma_{\text{bottom}}} = \underline{\underline{0}}, \quad (5.38)$$

$$\underline{\underline{\sigma}} \cdot \underline{\underline{n}} \Big|_{\Gamma_{\text{left}}} = -\underline{\underline{g}}(t), \quad (5.39)$$

$$\underline{\underline{\sigma}} \cdot \underline{\underline{n}} \Big|_{\Gamma_{\text{right}}} = \underline{\underline{g}}(t). \quad (5.40)$$

The forcing, $\underline{\underline{g}}(t)$, is a predetermined time-dependent vector describing the forcing at the boundaries of the domain. For this particular problem, we use

$$\underline{\underline{g}}(t) = g_0 \frac{(t/t_0)^2}{\sqrt{1 + (t/t_0)^2}} \underline{\underline{e}}_x \quad (5.41)$$

Where g_0 controls the magnitude of the forcing rate, t_0 controls how long the forcing takes to reach linearity in time, and $\underline{\underline{e}}_x$ is the unit vector in the x direction.

The QoIs are the stress-strain curve, the times corresponding to damage starting at the notch, the time at which this damage has propagated enough that the system has broken into two or more pieces; and the resulting damage distribution when the system has broken in two. We build the distributions of the QoIs using Monte Carlo sampling with 100 samples. Figure 5.9 shows the evolution of several fields of the notched uniaxial stress problem throughout its time duration. It also demonstrates how the crack propagates starting at the tip of the notch and proceeds downward until it reaches the bottom boundary of the domain.

5.5.2 Stopping Times - Initial Damage and Time of Breaking

Similar to that of the uniaxial strain problem, the damage variable forms a stochastic process over the course of each simulation. To that end, we wish to examine the distribution of two stopping times for this variable. The first is the time at which the first nonzero damage values occur. Observe that in Figure 5.9, once the damage first forms, it propagates downward until it reaches the bottom boundary. Based on this observation, we define the second stopping time as the time this initial crack first reaches the bottom boundary. In the physical setting, this corresponds to when the sample has fractured in two, and the remainder of the numerical simulation is non-physical.

More precisely, we can define the two stopping times as follows. Let the time at which the damage starts be defined by

$$T_{\text{start}} = \inf_{t>0} \{t : \exists \underline{x} \in \Omega \quad \text{with} \quad \mathcal{D}(\underline{x}, t) > 0\}. \quad (5.42)$$

For the second stopping time, we choose a width $\zeta \in (0, 0.5)$, which corresponds to a width around the center of the bottom boundary to search, and define the second stopping time as

$$T_{\text{fail}} = \min_{t>0} \{t : \exists x \in (0.5 - \zeta, 0.5 + \zeta) \quad \text{with} \quad \mathcal{D}((x, 0), t) = 1\}. \quad (5.43)$$

We will use an ensemble of 100 simulations to perform MC sampling of these two stopping times. To approximate the PDF of each stopping time, we will build a KDE

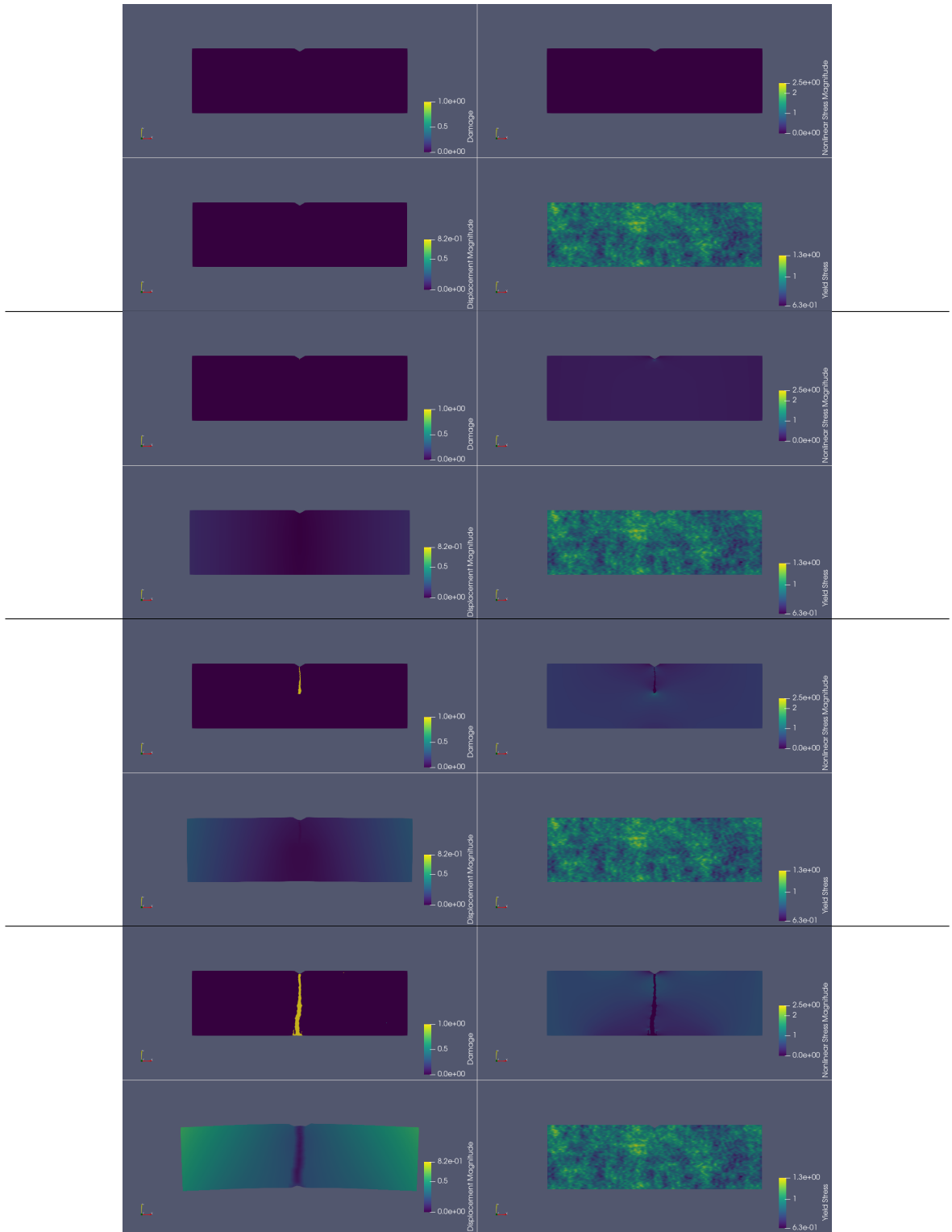


Figure 5.9: Time evolution of Damage, Stress (nonlinear), and Displacement fields for a selected sample of notched uniaxial stress problem. The yield stress field is displayed in the lower right corner. The displacement plot is warped by the displacement field. This warping is scaled up by a factor of 100. Figures are grouped in 2×2 blocks and vertically in order of $t = 0, 1.5, 3, 4$, respectively.

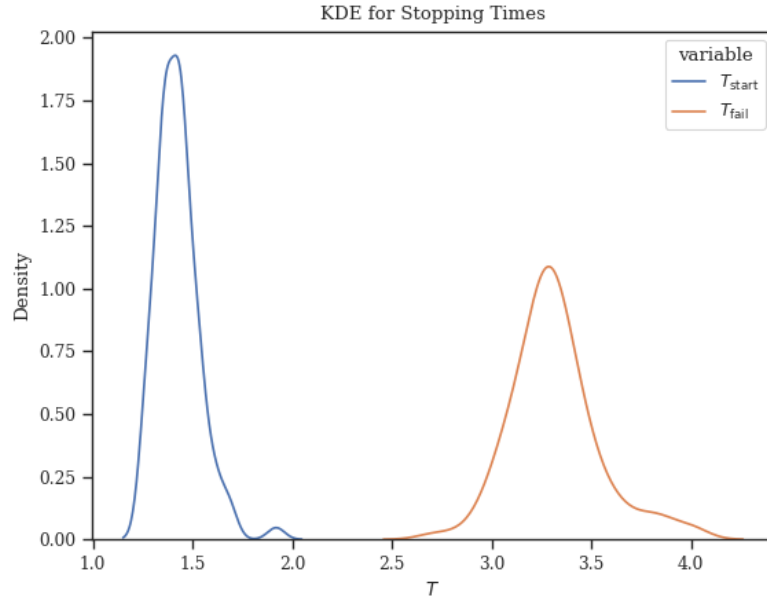


Figure 5.10: KDE plot for stopping times in the notched uniaxial stress problem. T_{start} corresponds to the time of damage initiation, while T_{fail} corresponds to the final physical time of the simulation when the crack has propagated through to the other side of the domain. The above PDF approximations were made using 100 samples for each stopping time.

using methods available in the `scipy.stats` module. The results can be seen in Figure 5.10. From this, it can be seen there is a clear separation between the distributions of the two stopping times. It is also evident T_{fail} is more widely distributed than T_{start} .

5.5.3 Stress-Strain Curve

The next QoI we examine is the average stress-strain curve. Similar to the uniaxial strain problem in the previous section, our goal is to build a model so that $\hat{\sigma} = \mathcal{S}(\hat{\varepsilon})$, where $\hat{\sigma}$ and $\hat{\varepsilon}$ are scalar averages of the stress and strain tensors respectively.

Since forcing is taking place along the x axis, we are only interested in the stress-strain curve for the x components of the stress and strain tensors. That is, we wish to build a relationship between ε_{11} and σ_{11} , each of which indicates the 11 component of

the respective tensor:

$$\hat{\varepsilon} = \int_{\Omega} \varepsilon_{11} dx \quad (5.44)$$

$$\hat{\sigma} = \int_{\Omega} \sigma_{11} dx = \int_{\Omega} (1 - \mathcal{D}) \sigma_{11}^{(L)} dx \quad (5.45)$$

$$\mathcal{S} : \hat{\varepsilon} \mapsto \hat{\sigma}. \quad (5.46)$$

In this setting, both the strain and stress are random variables due to the effect of the damage and the boundary conditions. In contrast to the uniaxial strain case, we no longer know the value of $\hat{\varepsilon}$ by a direct relation with time. From the time-discretization of the problem, we will have $\hat{\varepsilon}_n, \hat{\sigma}_n$, each of which is evaluated at the corresponding time node t^n . Importantly, between two samples n_1, n_2 , it may be the case $\hat{\varepsilon}_n^{(n_1)} \neq \hat{\varepsilon}_n^{(n_2)}$. Therefore a direct comparison between the stress values is no longer feasible.

Instead, given the collection $(\hat{\varepsilon}_n^{(m)}, \hat{\sigma}_n^{(m)})$ for each t^n for the m 'th sample, we will build an interpolant over the strain values. That is, construct a function $I^{(m)}$ such that

$$\hat{\sigma}_n^{(m)} = I^{(m)}(\hat{\varepsilon}_n^{(m)}). \quad (5.47)$$

Then we choose a uniform grid of strain values which will be the same across all samples. Let this grid be $\bar{\varepsilon}_n$, for time t^n . One way to do this is to take the pointwise average of the strain values:

$$\bar{\varepsilon}_n = \frac{1}{M} \sum_{m=1}^M \hat{\varepsilon}_n^{(m)}. \quad (5.48)$$

Then we will cast the stress values for each sample onto this uniform grid, using

$$\bar{\sigma}_n^{(m)} = I^{(m)}(\bar{\varepsilon}_n). \quad (5.49)$$

Afterward, we can do statistics on the pointwise values $\bar{\sigma}_n^{(m)}$, much the same way as in the uniaxial strain case. The results can be seen in Figure 5.11. In this figure, we plot the mean estimator on the stress-strain curve, as well as 95% confidence intervals on the estimator itself and a $\pm 1\zeta$ interval for the sample.

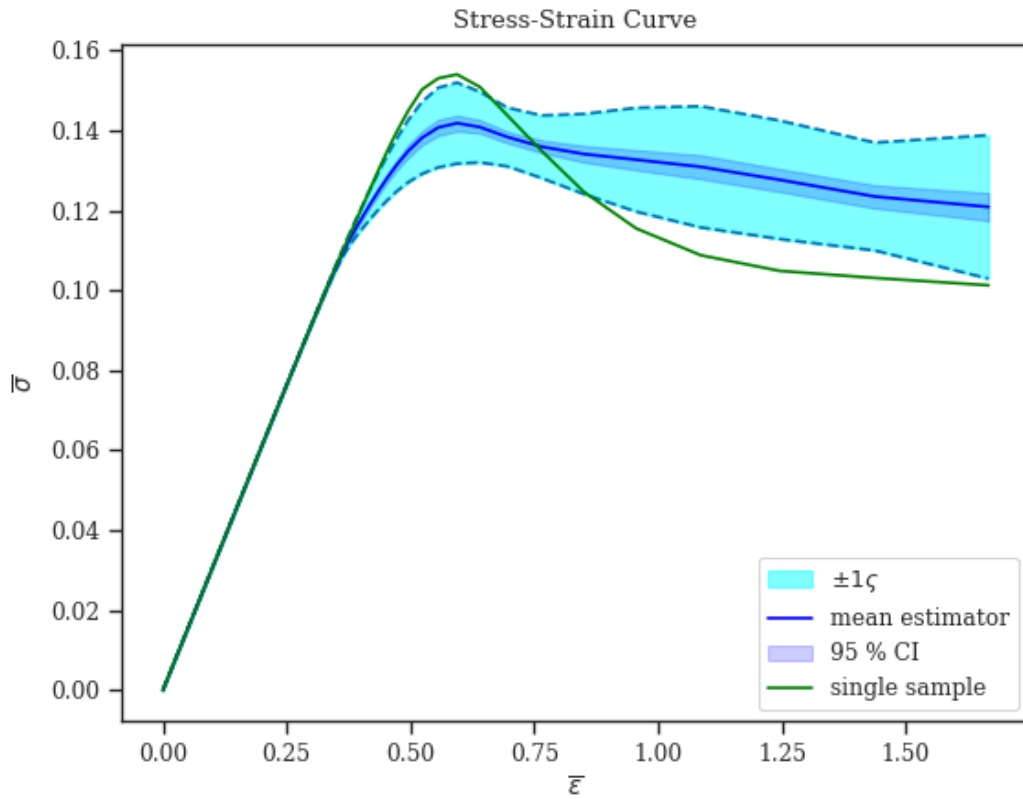


Figure 5.11: Stress-strain curve estimator with 95% confidence bounds on the estimator (blue - using standard error) and $\pm 1\zeta$ interval on the sample (cyan). In addition, the stress-strain curve corresponding to the sample shown in Figure 5.9 is displayed as a green line.

Going further, we can overlay the stopping time KDEs with the stress-strain curve. This enables us to match features in the stress-strain curve with the time of damage initiation and the time of the model failure. To convert the stopping time T into the corresponding strain value, we can build an interpolant such that

$$\bar{\varepsilon}_n = \bar{\varepsilon}(t^n). \quad (5.50)$$

Then the corresponding strains for each stopping time can be computed by evaluating $\bar{\varepsilon}(T)$. The resulting plot can be seen in Figure 5.12. We are able to see the maximum in the mean stress-strain curve corresponds with a sharp increase in the density of the failure time. This indicates features of the stress-strain curve can be correlated with system failure.

Additionally, the $\pm 1\zeta$ interval illustrates that deviations from linearity can still be expected to correlate with the rise in the KDE for T_{fail} . Through applying the asymptotic UQ bounds in (4.40), it is possible to extrapolate the model results to alternative distributions if the underlying random field for the yield stress were to have different properties. In this case, we take the correlation length $\ell = 0.2$. So for other correlation lengths, we can gain insight into the expected behavior.

5.5.4 Damage Distribution

As described above, T_{fail} gives the final time in the problem at which the problem represents a physical laboratory experiment. We take the final damage distribution to be the damage at this time:

$$\mathcal{D}_{\text{final}}(\underline{x}) := \mathcal{D}(\underline{x}, T_{\text{fail}}). \quad (5.51)$$

This random variable indicates the resulting damage distribution at the end of a simulation. We can use it to examine the mean crack propagation pattern and verify our initial assumption that the cracks initiate from the tip of the notch and proceed more or less straight down to the other boundary.

The variable $\mathcal{D}_{\text{final}}$ is itself a random field. However, we do not need to discretize it in order to sample it. Due to the finite element discretization used to solve the damage

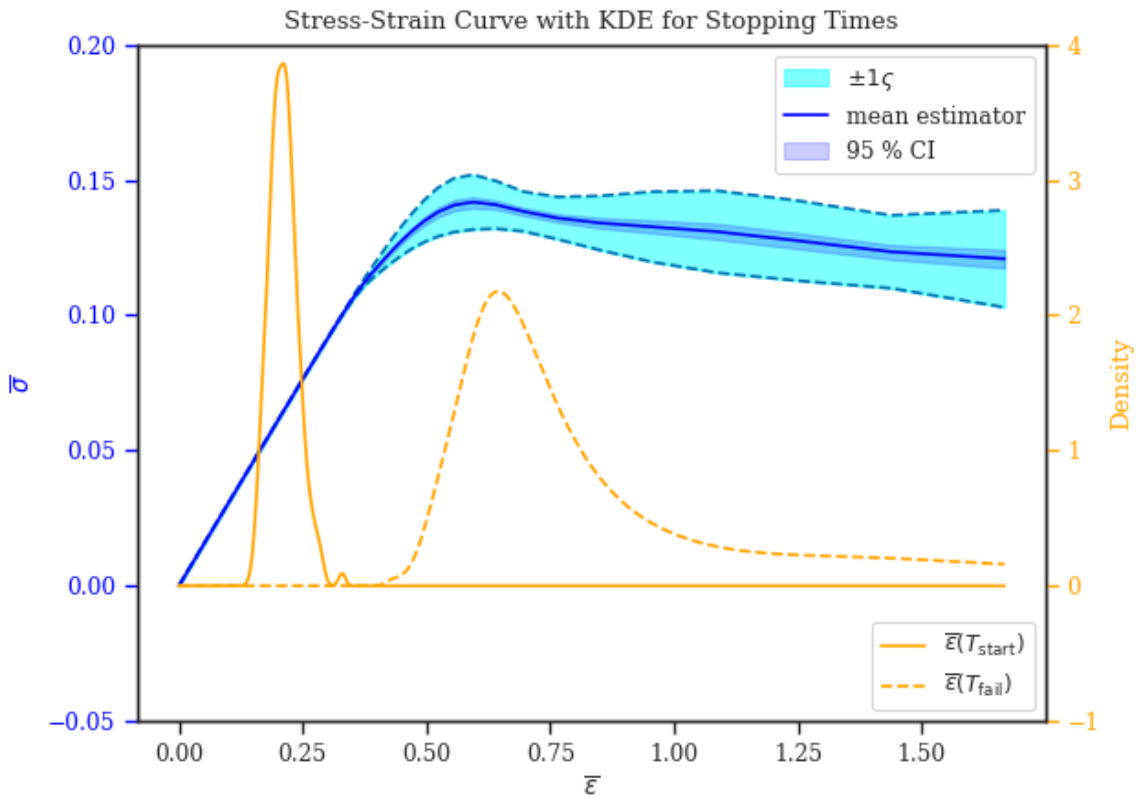


Figure 5.12: KDE plots for stopping times corresponding to when the damage starts and the final physical time of the notched uniaxial stress simulation are plotted over-top the stress-strain estimator and confidence intervals. The correspondence of the maximum value in the stress-strain curve with the sharp increase in the distribution of failure times indicates a correlation there, which could be used to evaluate the failure characteristics of these simulations.

mechanics problem, we are presented with a vector \mathbf{d} , from which we can reconstruct the damage variable using

$$\mathcal{D}(\underline{x}) = \sum_{n=1}^{\dim W} d_n w_n(\underline{x}), \quad (5.52)$$

where $\mathcal{D} \in W \subset L^\infty(\Omega)$ and w_n is a basis for W . Thus we can easily reconstruct the samples of $\mathcal{D}_{\text{final}}(\underline{x})$ from the finite element representation.

Of particular interest are the mean and variance or standard deviation of the final damage. We can compute both of these quantities pointwise for each \underline{x} as follows:

$$\overline{\mathcal{D}_{\text{final}}}(\underline{x}) = \frac{1}{N} \sum_{n=1}^N \mathcal{D}_{\text{final}}^{(n)}(\underline{x}), \quad (5.53)$$

$$s_{\mathcal{D}}(\underline{x}) = \sqrt{\frac{1}{N} \sum_{n=1}^N \left(\mathcal{D}_{\text{final}}^{(n)}(\underline{x}) - \overline{\mathcal{D}_{\text{final}}}(\underline{x}) \right)^2}. \quad (5.54)$$

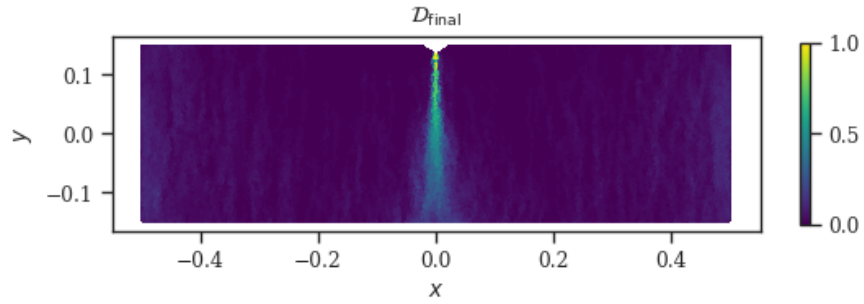
The results can be seen in Figure 5.13. This displays the mean damage field, the standard deviation of this damage field, and the standard error on the mean damage field estimator.

The high values of the standard deviation of $\mathcal{D}_{\text{final}}$ near the tip of the notch indicate small variations in the path of the damage from element to element. This can be understood by comparing the width of the yellow region in the mean damage field with that of the standard deviation. It indicates these fluctuations occur mainly in the center of the domain, and so only discern minor deviations in the damage path.

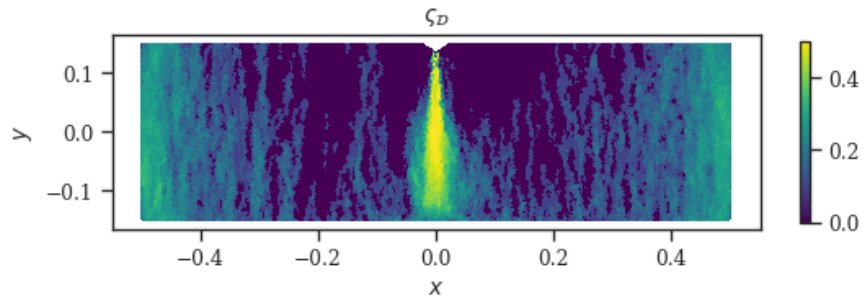
It is also evident from Figure 5.13 that the crack propagation is mostly downward as per our assumptions. However, it is also clear there are occurrences of extra damage to the sides of the domain, which can be seen clearly by the non-zero standard deviation values away from the center line of the domain. For plotting purposes, the domain of the problem was centered at the origin.

5.6 Conclusions from MC Sampling

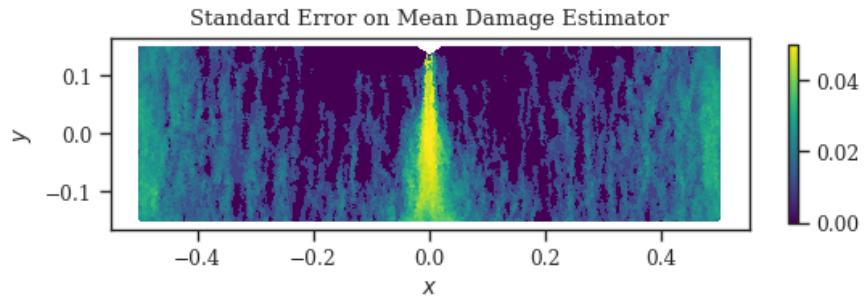
This chapter demonstrated the ability of MC sampling techniques to gather information on the random nature of the damage mechanics problem and provide



(a) $\overline{\mathcal{D}_{\text{final}}}(\underline{x})$ computed for standard MC procedure using 100 samples. The lack of damage outside the midline of the domain indicates damage primarily occurs extending vertically from the notch location.



(b) Pointwise standard deviation on $\mathcal{D}_{\text{final}}(\underline{x})$, using 100 samples in a standard MC procedure.



(c) Pointwise standard error on $\mathcal{D}_{\text{final}}(\underline{x})$, using 100 samples. This gives an indication of the precision for the mean damage estimator, namely that we have at least two significant figures for damages near 1.

Figure 5.13: Mean, standard deviation, and standard error computed pointwise for $\mathcal{D}_{\text{final}}(\underline{x})$ in the notched uniaxial stress problem.

insight into the behaviors and relationships between various QoIs. In addition, by combining ideas seen in Chapters 3 and 4, it is possible to bound the uncertainty between the models examined and possible alternative models using relatively simple means. This is vital in various engineering applications. By bounding the uncertainty for various settings, it is possible to determine tolerances and safe operating limits with limited and incomplete information.

We can also see why methods like Polynomial Chaos would be inefficient. The damage mechanics problem uses a random field with well over 100 degrees of freedom. These DoFs can come from either the FEM discretization directly, as in the expanding ring case, or from the KLE of the random field, as in the uniaxial tensile cases. Polynomial Chaos would therefore require constructing polynomial basis functions in over 100 dimensions. Furthermore, the uncertainty in these problems is a function of time, as evident from the stress-strain curves. The uncertainty band around the stress-strain curve estimator grows with time, and so Polynomial Chaos would become extremely computationally expensive to achieve reasonable results.

However, it is worth noting a major drawback of MC sampling. As discussed in Chapter 4, the primary driver of MC sampling techniques is the CLT. Consequentially improving the precision of estimators for various QoIs can require an enormous number of samples. To achieve an additional significant figure in the aforementioned problems, 100 times as many samples would need to be examined. For well-resolved FEM problems, this can quickly become prohibitively expensive. Therefore, as a next step, we will examine techniques designed to decrease the computation cost associated with MC methods.

Chapter 6

MULTILEVEL MONTE CARLO SAMPLING FOR QUANTITIES OF INTEREST

6.1 Introduction

In Chapter 5, we explored the idea of using Monte Carlo (MC) techniques to sample from the distributions of various QoIs. From these samples, we can construct estimators such as the mean and kernel density estimator (KDE). We can also quantify the precision of such estimators through quantities like the standard error and confidence intervals built using either the CLT or using Clopper-Pearson-type intervals.

A key feature of these methods is the scaling of the precision with the number of samples used in the MC procedure. If N is the number of samples used in the MC sampling ensemble, then the standard error scales as $O(N^{-1/2})$. Thus for every extra significant figure we desire, we need to multiply the total number of samples used by a factor of 100.

This scaling demonstrates a key vulnerability of MC techniques. For high-accuracy simulations, the number of samples required can be prohibitively large. This problem is exacerbated by the computational costs of high-accuracy models needed to achieve the necessary precision for each QoI sample. For example, in [32], the observed accuracy of the numerical scheme scales as $O(\Delta t)$ for time step size Δt . This linear scaling can mean that high-accuracy samples require a large number of time steps, thus increasing the computational expense for each sample.

The error incurred by a model is part of the epistemic uncertainty as in the context of Chapter 4. We can assume the magnitude of this epistemic uncertainty scales with the cost associated with a particular resolution of the model. In principle, we could examine problems that are cheap but not well resolved, allowing us to generate

more samples but incurring higher uncertainties. The alternative is to use a more well-resolved model and make concessions on the number of samples we can generate due to the computational cost.

To better explore this tradeoff, we consider a sequence of problem refinements. Let ℓ denote the problem refinement level, with $\ell = 1, 2, 3, \dots, L$. The lowest refinement will be level $\ell = 1$, while the highest is $\ell = L$, with refinement increasing as ℓ increases. With increasing refinement, we expect the epistemic uncertainty to decrease and the cost of each sample to increase.

At each level, the forward map \mathcal{F} is only resolved to a certain degree. To denote this, for level ℓ , the forward map will be written \mathcal{F}_ℓ . In the context of the damage mechanics problem, given a yield stress field Σ , the resulting QoI can be written as

$$Q_\ell = (\mathcal{Q} \circ \mathcal{F}_\ell)(\Sigma). \quad (6.1)$$

Due to the various epistemic uncertainty associated with different refinement levels, we can expect the distributions of the Q_ℓ to vary across different ℓ .

A researcher may use information from lower ℓ distributions for Q_ℓ to form hypotheses regarding the desired distribution for Q_L . However, these can only be tested by direct confirmation of generating the required samples from Q_L . As discussed above, this desired level may be prohibitively expensive. Multilevel Monte Carlo (MLMC) techniques aim to construct a rigorous framework with which information at various refinement levels can be systematically combined to yield better information on the desired distribution Q_L .

6.2 Standard MLMC

The authors in [69] present a tunable approach to perform MLMC sampling. The idea is based on splitting the expectation value for the L 'th level QoI into a telescoping series:

$$\mathbb{E}[Q_L] = \mathbb{E}[Q_1] + \mathbb{E}[Q_2 - Q_1] + \dots + \mathbb{E}[Q_L - Q_{L-1}]. \quad (6.2)$$

The expectation-of-difference terms on the right-hand side can be thought of as the biases between successive refinement levels. Let $B_\ell = Q_\ell - Q_{\ell-1}$,

$$\mathbb{E}[Q_L] = \mathbb{E}[Q_1] + \mathbb{E}[B_2] + \dots + \mathbb{E}[B_L]. \quad (6.3)$$

Suppose at level ℓ we sample a collection of N_ℓ samples from which we estimate each quantity in (6.3). Let $Q_\ell^{(n)}$ denote the n 'th sample generated at refinement level ℓ . Recall from Chapter 4 that the mean estimator is itself a random variable and will tend towards a normal distribution as per the CLT:

$$\bar{Q}_\ell := \frac{1}{N_\ell} \sum_{n=1}^{N_\ell} Q_\ell^{(n)}, \quad (6.4)$$

$$\bar{Q}_\ell \implies \mathcal{N}\left(\mathbb{E}[Q_\ell], \frac{\text{Var}[Q_\ell]}{N_\ell}\right), \quad \text{as } N_\ell \rightarrow \infty. \quad (6.5)$$

If the samples at level $\ell + 1$ are also generated at level ℓ , that is, each successive refinement level is performed on a subset of the those samples of the previous level, then we can build estimators for the biases between levels. The sum of the estimators, as a sum of Gaussian random variables, then will tend towards a known distribution due to the CLT and the additivity of Gaussians:

$$\hat{Q}_L := \bar{Q}_1 + \bar{B}_2 + \dots + \bar{B}_L, \quad (6.6)$$

$$\hat{Q}_L \implies \mathcal{N}(\mu_Q, \sigma_Q^2); \quad (6.7)$$

where

$$\mu_Q = \mathbb{E}[Q_1] + \sum_{\ell=2}^L \mathbb{E}[B_\ell] = \mathbb{E}[Q_L], \quad (6.8)$$

$$\sigma_Q^2 = \frac{\text{Var}[Q_1]}{N_1} + \sum_{\ell=2}^L \frac{\text{Var}[B_\ell]}{N_\ell}. \quad (6.9)$$

The variances of the biases can be written in terms of the variances of the underlying QoIs

$$\text{Var}[B_\ell] = \text{Var}[Q_\ell] + \text{Var}[Q_{\ell-1}]. \quad (6.10)$$

Therefore, we can compute σ_Q^2 in terms of the variances on each Q_ℓ :

$$\sigma_Q^2 = \sum_{\ell=1}^L \frac{\text{Var}[Q_\ell]}{N_\ell} + \sum_{\ell=1}^{L-1} \frac{\text{Var}[Q_\ell]}{N_{\ell+1}}. \quad (6.11)$$

For simplicity, let v_ℓ represent the appropriate variance at level ℓ :

$$v_1 = \text{Var}[Q_1], \quad (6.12)$$

$$v_\ell = \text{Var}[B_\ell], \quad \ell \geq 2. \quad (6.13)$$

The authors in [69] present an algorithm that, provided information for v_ℓ and the cost or workload at each level, can minimize the total workload while maintaining a desired level of precision. For each level, we need to define a workload per sample, W_ℓ . The total computational cost and resulting estimator precision can be written

$$\text{cost} \quad W = \sum_{\ell=1}^L W_\ell N_\ell \quad (6.14)$$

$$\text{precision} \quad \sigma_Q^2 = \sum_{\ell=1}^L \frac{v_\ell}{N_\ell}. \quad (6.15)$$

Choosing a tolerance precision σ_{tol} the optimization problem [69] solves is

$$\text{minimize } W(N_1, \dots, N_L) \quad \text{subject to } \sigma_Q^2 \leq \sigma_{\text{tol}}^2. \quad (6.16)$$

The resulting distribution for the number of samples at each level is given by

$$N_\ell^{(\text{opt})} = \frac{1}{\sigma_{\text{tol}}^2} \sqrt{\frac{v_\ell}{W_\ell}} \sum_{\ell=1}^L \sqrt{v_\ell W_\ell}. \quad (6.17)$$

An alternative optimization consideration is the following. Suppose one is limited in the total workload for the MLMC ensemble, W^* , and the goal instead is to achieve the best possible precision. This problem reads

$$\text{minimize } \sigma_Q^2 \quad \text{subject to } W \leq W^*. \quad (6.18)$$

By making the change of variables $f_\ell = 1/N_\ell$, this problem reads mathematically identically to (6.16), and it can be shown the solution to (6.18) is

$$\tilde{N}_\ell^{(\text{opt})} = W^* \sqrt{\frac{v_\ell}{W_\ell}} \frac{1}{\sum_{\ell=1}^L \sqrt{v_\ell W_\ell}} \quad (6.19)$$

In both (6.17), (6.19), note that $N_\ell^{(\text{opt})}$ is proportional to $\sqrt{v_\ell/W_\ell}$.

By assumption, the workload W_ℓ increases as ℓ increases. It is also expected that the variance v_ℓ will decrease as ℓ increases, although this is not guaranteed. It can be shown

$$N_\ell^{(\text{opt})} \geq N_{\ell+1}^{(\text{opt})} \iff \frac{W_{\ell+1}}{W_\ell} \geq \frac{v_{\ell+1}}{v_\ell}. \quad (6.20)$$

That is, it is only more worthwhile to decrease the number of samples as ℓ increases, if the workload scales up faster than the variance. If this fails for any given ℓ , it indicates the computation cost of level $\ell + 1$ outweighs any precision gains from level $\ell + 1$.

How this should be remedied is up to the user to determine. One option is to remove the offending level ($\ell^* + 1$), and renumber the remaining levels:

$$\tilde{\ell} = \begin{cases} \ell & \ell \leq \ell^* \\ \ell - 1 & \ell > \ell^* + 1 \end{cases}. \quad (6.21)$$

Alternatively, if this discrepancy happens for $\ell^* = 1$, it may indicate that the initial refinement is not well resolved and instead it may be preferable to change the second refinement to the first, and renumber accordingly

$$\tilde{\ell} = \ell - 1, \quad \ell = 2, 3, \dots, L. \quad (6.22)$$

The value chosen for the workload depends on what we consider to be the important costs of running a simulation. On many supercomputing systems, users pay by CPU hour. So a task that is given 4 cores and takes 5 hours to run would use up 20 CPU hours. According to [77], the new Darwin computer for the University of Delaware costs an industrial user \$0.05 per CPU-hour, and \$1 per GPU-hour (equivalent computation time on a GPU). Thus choosing W_ℓ to be the number of CPU hours required to run a particular simulation would enable the user to, quite literally, minimize cost.

In this thesis, we will use a computational cost proportional to the FLOP count required for a specific problem. For a problem with M degrees of freedom, if the model FLOP count scales as $O(M^p)$, for some power p , we can simply take $W_\ell = M_\ell^p$ where M_ℓ is the number of degrees of freedom at refinement level ℓ .

In general, the values for v_ℓ and W_ℓ may not be known a priori. To estimate these values, one could take a collection of seed samples on each level, for example, $N_\ell^{(\text{seed})} = 10$ for each ℓ . Evaluating the corresponding QoIs will give a small dataset from which the values for v_ℓ and W_ℓ can be estimated. This provides data on the required number of samples per each level: $N_\ell^{(\text{opt})}$. Next, additional samples can be generated as needed, and the process can be repeated until some convergence requirement is reached, for example, the required tolerance is achieved for the ensemble.

More generally, the framework proposed in [69] enables L to be chosen adaptively. That is, the highest refinement level can be pushed successively higher as required to achieve the desired precision. For the purposes of this thesis, we will only be considering fixed L to ensure computation costs remain strictly bounded.

It is possible to describe this MLMC procedure as a weighted sum of the sample values, $Q_\ell^{(n)}$. Expanding the sums, it can be shown

$$\hat{Q}_L = \sum_{\ell=1}^L \sum_{n=1}^{N_\ell} \omega_\ell^{(n)} Q_\ell^{(n)}, \quad (6.23)$$

$$\omega_\ell^{(n)} = \begin{cases} -\left(\frac{N_\ell - N_{\ell+1}}{N_\ell N_{\ell+1}}\right) & \ell < L, \quad n \leq N_{\ell+1} \\ \frac{1}{N_\ell} & \ell < L, \quad n > N_{\ell+1} \\ \frac{1}{N_L} & \ell = L \end{cases}. \quad (6.24)$$

Recall that, by assumption, $N_\ell \geq N_{\ell+1}$ for every ℓ .

The above reformulation raises some concerns regarding certain kinds of QoIs. In particular, the negative weights can bring a positive definite QoI into a negative value. A trivial example of this would be a QoI which takes values 0 or 1. Suppose we examine two levels, and a total of two samples; and the trials come back as follows

$$q_1^{(1)} = 1, \quad q_1^{(2)} = 0, \quad q_2^{(1)} = 0. \quad (6.25)$$

Then MLMC would compute \hat{q} by

$$\hat{q} = -\frac{1}{2}q_1^{(1)} + \frac{1}{2}q_1^{(2)} + \frac{1}{1}q_2^{(1)} = -\frac{1}{2}. \quad (6.26)$$

This means the standard MLMC procedure, as presented in [69], is insufficient for computing values like probabilities.

Of particular interest is the probability of an event E . We wish to apply an MLMC procedure to evaluate $\mathbb{P}(E)$. In this circumstance, negative values are not permissible. Instead, we need to modify the above framework to prevent negative probabilities.

6.3 Conditional MLMC for Probabilities

The main idea for the conditional MLMC procedure is splitting the probability at level $\ell + 1$ based on the values at level ℓ using Bayes' rule. Let E be an event whose probability we wish to determine, and let E_ℓ refer to the event distribution when sampled at refinement level ℓ . By the additivity property of the probability measure,

$$\mathbb{P}(E_{\ell+1}) = \mathbb{P}(E_{\ell+1} \cap E_\ell) + \mathbb{P}(E_{\ell+1} \cap E_\ell^c). \quad (6.27)$$

Where E^c denotes the complement of E . Using the definition of conditional probabilities gives

$$\mathbb{P}(E_{\ell+1}) = \mathbb{P}(E_{\ell+1} | E_\ell)\mathbb{P}(E_\ell) + \mathbb{P}(E_{\ell+1} | E_\ell^c)(1 - \mathbb{P}(E_\ell)). \quad (6.28)$$

Thus, supposing we know $\mathbb{P}(E_\ell)$, then we only need the conditional probabilities $\mathbb{P}(E_{\ell+1} | E_\ell)$ and $\mathbb{P}(E_{\ell+1} | E_\ell^c)$ to evaluate $\mathbb{P}(E_{\ell+1})$. We could evaluate $\mathbb{P}(E_1)$ directly and proceed iteratively. This approach was demonstrated in [72] for computing probabilities using MLMC, and we can employ a similar approach here.

A demonstrative case is when examining the probability a QoI is bounded above by some value. Let X be a random variable taking values in $\mathcal{X} \subset \mathbb{R}$, and let $X_\ell^{(n)}$ refer to the n 'th sample of X at refinement level ℓ . Consider the event $E(x) = \{X \leq x\}$. Building an approximation for the CDF for X corresponds to determining

$$C(x) = \mathbb{P}(X \leq x) = \mathbb{E}[E(x)]. \quad (6.29)$$

Once we have access to $C(x)$, differentiating gives the PDF, $\rho(x)$, with the property

$$\mathbb{P}(X \in S) = \int_S \rho(x) dx. \quad (6.30)$$

Thus by building the CDF, we have effectively reconstructed the probability measure for X .

Let $C_\ell(x) = \mathbb{P}(X_\ell \leq x)$, that is, C_ℓ is the CDF for X when sampled at refinement level ℓ . We can iteratively construct the CDF for level L by

$$C_1(x) = \mathbb{P}(X_1 \leq x) \tag{6.31}$$

$$C_{\ell+1}(x) = \mathbb{P}(X_{\ell+1} \leq x \mid X_\ell \leq x)C_\ell(x) + \mathbb{P}(X_{\ell+1} \leq x \mid X_\ell > x)(1 - C_\ell(x)). \tag{6.32}$$

Computationally we can proceed as follows. First, compute the KDE on X_1 , $\hat{\rho}_1(x)$. From this, approximate the CDF at level 1 by integrating:

$$C_1(x) \approx \int_{-\infty}^x \hat{\rho}_1(\xi) d\xi. \tag{6.33}$$

For the inductive step, we will only consider the first conditional probability, $\mathbb{P}(X_{\ell+1} \leq x \mid X_\ell \leq x)$, as the second conditional can be computed analogously.

6.3.1 Evaluating Conditional Probabilities

Consider the collection of data:

$$X_\ell^{(1)}, X_\ell^{(2)}, \dots, X_\ell^{(N_\ell)}, X_{\ell+1}^{(1)}, X_{\ell+1}^{(2)}, \dots, X_{\ell+1}^{(N_{\ell+1})}. \tag{6.34}$$

To make comparisons properly, we must consider a subset the above, where each sample is repeated at each level. Specifically, each sample $X_\ell^{(n)}$ must also be duplicated at $X_{\ell+1}^{(n)}$. This corresponds to the collection of samples

$$X_\ell^{(1)}, X_\ell^{(2)}, \dots, X_\ell^{(N_{\ell+1})}, X_{\ell+1}^{(1)}, X_{\ell+1}^{(2)}, \dots, X_{\ell+1}^{(N_{\ell+1})}. \tag{6.35}$$

We have several options to evaluate the conditional probability on this dataset. We can either consider further subsets of the data for which the conditions hold true, or we can build joint distributions on the whole of (6.35).

For the following methods, we can fix the value of x , and evaluate the conditional probability. Then, we can repeat this for all required values of x , to build the condition for all x . Repeating for $\mathbb{P}(X_{\ell+1} \leq x \mid X_\ell > x)$ we can then construct $C_{\ell+1}(x)$. One

need not consider all $x \in \mathcal{X}$ for this process. Instead, by the assumption that X has a PDF (i.e. its probability measure is absolutely continuous with respect to the Lebesgue measure), we can compute $C_\ell(x)$ on a grid of x points, x_1, x_2, \dots, x_M . Then we can compute $C'_\ell(x)$ using a finite-difference scheme. The choice of the grid points and finite-difference scheme adds epistemic uncertainty to the resulting PDF. However, as discussed in Chapter 4, it is possible to bound the introduced error simply by knowing the variance of the QoI and proposed alternative model for which the epistemic uncertainty changes.

6.3.1.1 Brute-Force by Subsampling

Fixing the value of x , then we can take a further subsample of the above data in (6.35):

$$S_x := \left\{ X_{\ell+1}^{(j)} \text{ for } j \text{ with } X_\ell^{(j)} \leq x \right\}. \quad (6.36)$$

Then using $\mathbb{P}(E) = \mathbb{E}[\mathbb{1}(E)]$, where $\mathbb{1}(\cdot)$ is the indicator function, let $\#\{\cdot\}$ be the number of elements in a finite set. We can evaluate the conditional probability by

$$\mathbb{P}(X_{\ell+1} \leq x \mid X_\ell \leq x) \approx \frac{\#\{X_{\ell+1} \in S_x : X_{\ell+1} \leq x\}}{\#(S_x)}. \quad (6.37)$$

6.3.1.2 KDE by Subsampling

Alternatively, we can build the KDE on the subsampled data. That is, construct the subsampled KDE

$$\hat{\rho}_{S_x}(\xi) = \frac{1}{\#(S_x)} \sum_{X_{\ell+1} \in S_x} \kappa(\xi - X_{\ell+1}). \quad (6.38)$$

Then the conditional probability can be computed by integrating this KDE

$$\mathbb{P}(X_{\ell+1} \leq x \mid X_\ell \leq x) \approx \int_{-\infty}^x \rho_{S_x}(\xi) d\xi. \quad (6.39)$$

As an advantage, the resulting updated CDF will likely be smoother than that of the brute-force method above. However, there are some book-keeping tasks that need care when programming this method, for dealing with the cases $\#(S_x) = 1$ and if $S_x = \emptyset$.

In particular, if $S_x = \emptyset$, then $\mathbb{P}(X_{\ell+1} \leq x \mid X_\ell \leq x) = 0$. In computing the KDE, software such as `scipy.stats` will use multiple differing data points to compute the optimal kernel smoothing value (see Chapter 4), and to produce a system which can quickly be evaluated for many points. Therefore, if only one sample is available, KDE generation can fail. Then $\mathbb{P}(X_{\ell+1} \leq x \mid X_\ell \leq x)$ is determined entirely by whether the sole element of S_x satisfies $X \leq x$.

6.3.1.3 Sum of Indicators

Using the entirety of the joint data

$$J = \left\{ \left(X_{\ell+1}^{(j)}, X_\ell^{(j)} \right), j = 1, 2, \dots, N_{\ell+1} \right\}, \quad (6.40)$$

the conditional probability can be computed as follows. First, expand the conditional probability using Bayes' rule

$$\mathbb{P}(X_{\ell+1} \leq x \mid X_\ell \leq x) = \frac{\mathbb{P}(X_{\ell+1} \leq x \cap X_\ell \leq x)}{\mathbb{P}(X_\ell \leq x)}. \quad (6.41)$$

Using $\mathbb{P}(\cdot) = \mathbb{E}[\mathbb{1}(\cdot)]$ we can write

$$\mathbb{P}(X_\ell \leq x) = \frac{1}{N_{\ell+1}} \sum_{n=1}^{N_{\ell+1}} \mathbb{1}(X_\ell^{(n)} \leq x), \quad (6.42)$$

$$\mathbb{1}(X_{\ell+1} \leq x \cap X_\ell \leq x) = \mathbb{1}(X_{\ell+1} \leq x) \cdot \mathbb{1}(X_\ell \leq x), \quad (6.43)$$

$$\mathbb{P}(X_{\ell+1} \leq x \cap X_\ell \leq x) = \frac{1}{N_{\ell+1}} \sum_{n=1}^{N_{\ell+1}} \mathbb{1}(X_{\ell+1} \leq x) \cdot \mathbb{1}(X_\ell \leq x). \quad (6.44)$$

Assembling this together gives

$$\mathbb{P}(X_{\ell+1} \leq x \mid X_\ell \leq x) \approx \frac{\sum_{n=1}^{N_{\ell+1}} \mathbb{1}(X_{\ell+1} \leq x) \cdot \mathbb{1}(X_\ell \leq x)}{\sum_{n=1}^{N_{\ell+1}} \mathbb{1}(X_\ell \leq x)}. \quad (6.45)$$

On close inspection, one can see this procedure is mathematically equivalent to the brute force by subsampling method. This approach replaces the further subsampling required by summing indicator functions.

6.3.1.4 Joint KDE

The final way to compute this conditional probability comes from building the KDE on the joint distribution of data. Using the above set J in (6.40), and the set $P = \{X_\ell^{(n)}, n = 1, 2, \dots, N_{\ell+1}\}$, one can construct the joint KDE, $\hat{\rho}_J(x_{\ell+1}, x_\ell)$, and the KDE on only the data at level ℓ : $\hat{\rho}_P(x_\ell)$. Using the Bayes' rule in (6.41), the probabilities can be approximated by integrating the respective KDEs:

$$\mathbb{P}(X_{\ell+1} \leq x \mid X_\ell \leq x) \approx \frac{\int_{-\infty}^x \int_{-\infty}^x \hat{\rho}_J(\eta, \xi) d\eta d\xi}{\int_{-\infty}^x \hat{\rho}_P(\xi) d\xi}. \quad (6.46)$$

The advantage of the joint KDE approach is that no extra subsampling need be done, and the resulting updated CDF will be smooth, enabling more accurate differentiation to determine a final PDF.

6.3.2 Measure of Precision for MLMC Distribution

In the context of MLMC, as discussed in [69], we need to determine a metric for the precision of the resulting distribution. This precision metric will enable the choice of the number of samples taken at each of the various sampling levels. In the standard MLMC case, the use of the CLT ensured there was a viable metric - the standard error - which scales with the number of sampling points and could be pushed below a specified tolerance.

In the computation of the CDF itself, the CLT was insufficient due to the allowance of negative values from the negative weights appearing in (6.23) and (6.24). However, determining the number of samples we should require at a specified refinement level depends largely on the spread of the data at that particular level. Therefore, we want to use the variance at each level.

In determining the distribution for the QoI, Q , we are changing the QoI from Q itself to an indicator function of the form $\tilde{Q}(x) = \mathbb{1}(Q \leq x)$. This is a Bernoulli random field dependent on x . Recall that for a Bernoulli random variable \tilde{Q} we have

$$\text{Var}[\tilde{Q}] = \mathbb{E}[\tilde{Q}] - \mathbb{E}[\tilde{Q}]^2. \quad (6.47)$$

Applying this for all x , we obtain

$$\text{Var}[\mathbb{1}(Q \leq x)] = \mathbb{P}(Q \leq x) - \mathbb{P}(Q \leq x)^2. \quad (6.48)$$

Therefore, at each level, we can compute the variance v_ℓ by

$$v_\ell = \int_{-\infty}^{\infty} C_\ell(x) - C_\ell^2(x) dx = \|C_\ell(x) - C_\ell^2(x)\|_{L^1}. \quad (6.49)$$

This variance can be fed into either (6.17) or (6.19) depending on whether the intended optimization is of workload or precision. Again, this precision could be estimated a priori using a collection of seed samples at each level.

There are also other metrics which can be used to compute v_ℓ . Using Clopper-Pearson intervals, the total area encapsulated within the interval is one measure of uncertainty in probability, and could be used in place of v_ℓ .

Considering the standard MLMC case described in [69], the desired metric can be an indicator of the bias between two adjacent refinement levels. So another option is to examine the discrepancy between the probability measures deduced between adjacent refinement levels.

In the MLMC context, there is no guarantee of one refinement's distribution being absolutely continuous with respect to another. Thus the relative entropy measure is not useful in this situation. A simple option is the Kolmogorov-Smirnov test statistic. In this case, the error measurement is simply the maximum height difference between C_ℓ and $C_{\ell+1}$:

$$v_\ell^{(KS)} = \sup_{x \in \mathbb{R}} |C_\ell(x) - C_{\ell+1}(x)| = \|C_\ell - C_{\ell+1}\|_{L^\infty}. \quad (6.50)$$

This generalizes easily to the case of probability distributions in higher dimensions through the total-variation norm, see Chapter 4 for more details. The L^2 norm can also be used instead of the L^∞ or L^1 norms.

Another alternative is to use the Hellinger distance, defined by

$$H^2(C_\ell, C_{\ell+1}) = \frac{1}{2} \int_{-\infty}^{\infty} \left(\sqrt{C'_\ell(x)} - \sqrt{C'_{\ell+1}(x)} \right)^2 dx \quad (6.51)$$

Where C'_ℓ denotes the derivative of C_ℓ . Through some simplification, it can be shown

$$H^2(C_\ell, C_{\ell+1}) = 1 - \int_{-\infty}^{\infty} \sqrt{C'_\ell(x)C'_{\ell+1}(x)} dx. \quad (6.52)$$

Then we can simply take $v_\ell^{(H)} = H^2(C_\ell, C_{\ell+1})$. The primary drawback to using the Hellinger distance is it requires computing the PDF at intermediate computations, while the L^p errors discussed above rely only on the computed values of C_ℓ .

For the remainder of this chapter, we will examine several experiments in applying these ideas from MLMC to various damage mechanics simulations. This will provide some examples as to how these ideas can be applied and yield insight into their advantages and drawbacks.

6.4 Notched Uniaxial Stress Problem

In this experiment, we consider an MLMC version of the notched uniaxial stress problem examined in Chapter 5. For convenience, below are listed the domain and boundary conditions associated with the damage mechanics problem in the notched uniaxial stress configuration.

6.4.1 Domain and Boundary Conditions

The domain for the notched uniaxial stress problem is a rectangle with a small notch cut out of the top portion of the domain. The rectangle is of length 1 and width $w \in (0, 1)$, and pulled along its length. The notch will be an isosceles triangle of width ν and extend to a depth of δ into the rectangular domain, taken from the middle of the top portion of the domain. That is

$$\Omega_{\text{rect}} = (0, 1) \times (0, w), \quad (6.53)$$

$$\Omega_{\text{notch}} = \mathfrak{T}((0.5 - \nu/2, w), (0.5 + \nu/2, w), (0.5, w - \delta)), \quad (6.54)$$

$$\Omega = \Omega_{\text{rect}} \setminus \Omega_{\text{notch}}. \quad (6.55)$$

Where $\mathfrak{T}(A, B, C)$ is a triangle with vertices located at A, B , and C . The basic layout can be seen in Figure 6.1

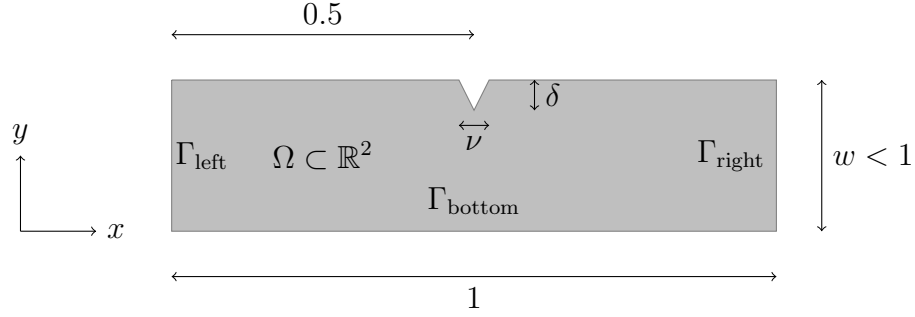


Figure 6.1: Diagram of the domain and boundaries in the notched uniaxial stress problem.

We split the boundary of the domain into four parts. The bottom, top, and left and right segments:

$$\Gamma_{\text{bottom}} = \{\underline{x} \in \partial\Omega : y = 0\}, \quad (6.56)$$

$$\Gamma_{\text{left}} = \{\underline{x} \in \partial\Omega : x = 0\}, \quad (6.57)$$

$$\Gamma_{\text{right}} = \{\underline{x} \in \partial\Omega : x = 1\}, \quad (6.58)$$

$$\Gamma_{\text{top}} = \partial\Omega \setminus (\Gamma_{\text{bottom}} \cup \Gamma_{\text{left}} \cup \Gamma_{\text{right}}). \quad (6.59)$$

The associated boundary conditions for the notched uniaxial stress problem are fixed normal stresses on the left and right boundaries and stress-free conditions on the top and bottom boundaries.

$$\underline{\underline{\sigma}} \cdot \underline{\underline{n}} \Big|_{\Gamma_{\text{top}} \cup \Gamma_{\text{bottom}}} = \underline{\underline{0}}, \quad (6.60)$$

$$\underline{\underline{\sigma}} \cdot \underline{\underline{n}} \Big|_{\Gamma_{\text{left}}} = -\underline{\underline{g}}(t), \quad (6.61)$$

$$\underline{\underline{\sigma}} \cdot \underline{\underline{n}} \Big|_{\Gamma_{\text{right}}} = \underline{\underline{g}}(t). \quad (6.62)$$

Where $\underline{\underline{g}}(t)$ is a predetermined time-dependent vector that describes the forcing at the boundaries of the domain. For this particular problem, we use

$$\underline{\underline{g}}(t) = g_0 \frac{(t/t_0)^2}{\sqrt{1 + (t/t_0)^2}} \underline{\underline{e}}_x, \quad (6.63)$$

where g_0 controls the magnitude of the forcing rate, t_0 controls how long the forcing takes to reach linearity in time, and $\underline{\underline{e}}_x$ is the unit vector in the x direction.

6.4.2 MLMC Hierarchy and QoIs

We wish to compare the results in the MLMC configuration against those from Chapter 5. To that end, we will consider an MLMC hierarchy of three refinement levels. Level $L = 3$ will correspond with the samples generated from Chapter 5, while levels $\ell = 1, 2$ will be lower resolution versions of that level. We chose the meshes for each level by starting with level 1, then doing a single iteration of the Red-Refine algorithm for level 2, and again for level 3.

At each level, the workload will be determined by the FLOP count of the linear algebra system that is to be solved to propagate the solution forward by a single time step. As discussed previously, it is observed that our algorithm scales linearly with the number of degrees of freedom (DoFs) in the FEM system. Therefore, we choose the workload W_ℓ at level ℓ to be equal to the DoF count of the FEM system for each mesh refinement.

Since we already have 100 samples at level 3 using standard MC methods, for comparison, we generate 100 samples at levels 2 and 1 as well. From these samples, we compute the maximum variance over the stress-strain curve bias values. That is, we evaluate the stress QoI pointwise over each time in the simulation, and build the bias between it and the next lower refinement level. Taking the maximum of the value over the time of the simulation produces the value used for v_ℓ in (6.17). More precisely:

$$\hat{\sigma}_\ell^{(n)}(t) = (\mathcal{Q} \circ \mathcal{F}_\ell)(\Sigma^{(n)}), \quad (6.64)$$

$$G_\ell^{(n)}(t) = \begin{cases} \hat{\sigma}_1^{(n)}(t) & \ell = 1 \\ \hat{\sigma}_\ell^{(n)}(t) - \hat{\sigma}_{\ell-1}^{(n)}(t) & \ell \geq 2 \end{cases}, \quad (6.65)$$

$$v_\ell = \max_t \{\text{Var}[G_\ell(t)]\} \quad (6.66)$$

We choose the tolerance on the standard error such that the optimal number of samples at level 1 is 100. In this way, we now have a direct comparison to the experiment in Chapter 5: examining 100 samples using standard MC methods and examining 100 samples using MLMC methods. Based on this information, Table 6.1

Level	No. Samples	Cost (CPU-hrs)
1	100	134
2	45	180
3	10	160
Total		474

Table 6.1: MLMC Hierarchy for number of samples on each refinement level in the notched uniaxial stress problem. The number of samples at each level were rounded up to the nearest 5 for a more elegant and intuitive distribution. The total cost of each refinement level in CPU-hours is also tabulated including the total cost for the MLMC ensemble.

outlines the distribution for how many samples should be generated at levels 1, 2 and 3.

The third column of Table 6.1 tallies the total computation cost, in CPU-hours of performing the MLMC procedure. Furthermore, the total computation cost of doing the standard MC experiment in Chapter 5 was 1,600 CPU hours. Thus MLMC cuts the computational cost by a quarter. As most supercomputing systems require payment by the CPU hour, this would allow the user to reduce their financial costs by 75 % for performing the simulations.

Performing an analogous computation for the time at which damage begins to start, and using the variance based on (6.49), the resultant number of samples at levels 1, 2 and 3 turns out to be 100, 34, and 12 respectively. For simplicity, we will be using the sampling distribution in Table 6.1. Based on this distribution, we will examine several QoIs from the MLMC context.

6.4.3 Stress-Strain Curve

Recalling the stress-strain curve QoI examined for the notched uniaxial stress problem in Chapter 5, we are interested in the relationship between the x components

of the stress and strain tensors. This relationship is summarized below.

$$\hat{\varepsilon} = \int_{\Omega} \varepsilon_{11} dx \quad (6.67)$$

$$\hat{\sigma} = \int_{\Omega} \sigma_{11} dx = \int_{\Omega} (1 - \mathcal{D}) \sigma_{11}^{(L)} dx \quad (6.68)$$

$$\mathcal{S} : \hat{\varepsilon} \mapsto \hat{\sigma}. \quad (6.69)$$

Where ε_{11} represents taking the 11 component of the strain tensor, $\underline{\underline{\varepsilon}}$.

For each simulation, we interpolate the stress-strain relationship onto a predetermined grid of strain values. This enables us to examine the statistics of the resulting stress values to build the stress-strain curve estimators. The results can be seen in Figure 6.2. In this figure, a 95% confidence bound is plotted around both the estimator, and a $\pm 1\zeta$ interval is plotted for the sample; shown in blue and cyan, respectively.

We can also compare the resulting estimators for the stress-strain curve using MLMC and MC procedures. This can be seen in Figure 6.3. By cutting the required computational cost, we are still able to recover the estimator to within 95% confidence.

6.4.4 Stopping Times - Initial Damage and Time of Breaking

As discussed in Chapter 5, there are two stopping times we can examine. These are, T_{start} and T_{fail} , and correspond to the first time at which nonzero damage appears and the last time at which the simulation represents a physical system. Using the MLMC hierarchy in Table 6.1, consider the KDE for each level's stopping time data, shown in Figure 6.4.

Figure 6.4 illustrates the goal of using MLMC for a probability distribution QoI. Specifically, lower-resolution data may exhibit a clear bias. Therefore MLMC should negate this bias when constructing the estimator at the finest refinement level. We apply the MLMC procedure described above to this data to build an estimator of the CDFs of the highest refinement level. The results can be seen in Figure 6.5. In this figure, it can be seen that we reconstruct the MC CDF within a 95% confidence interval around the estimator generated using MLMC.

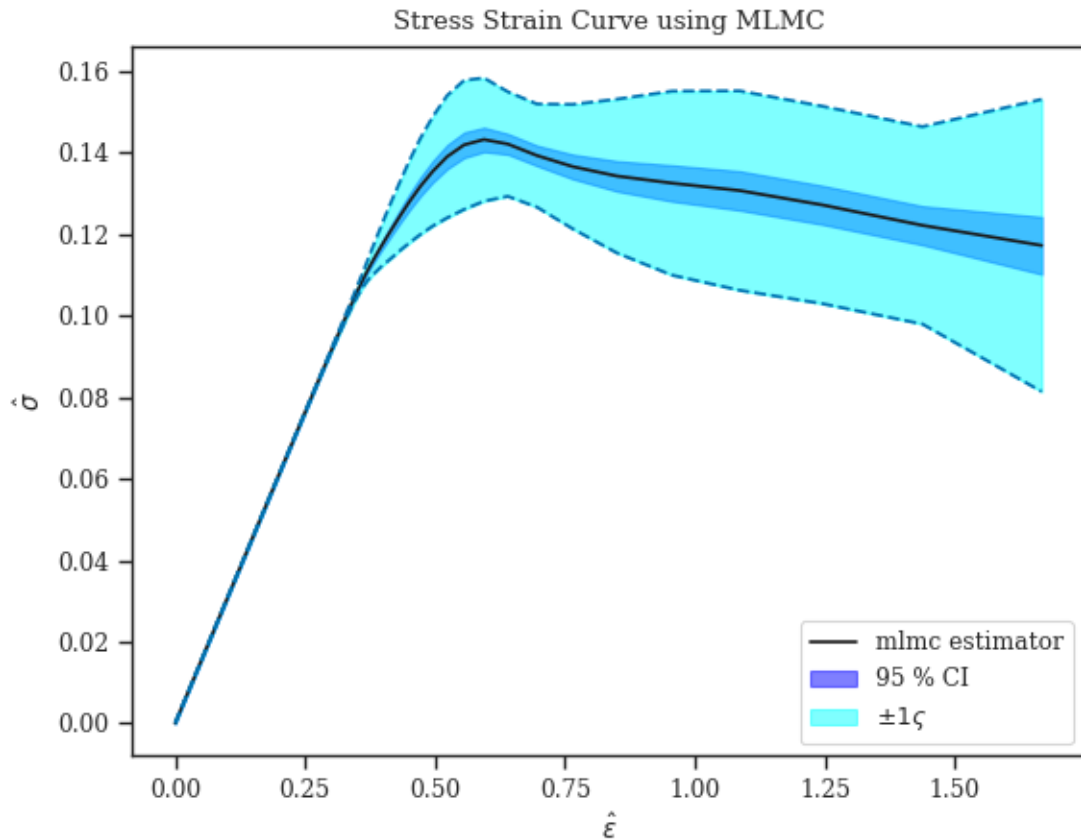


Figure 6.2: Stress-strain curve for notched uniaxial stress problem, using an MLMC hierarchy of 100 - 40 - 10 samples on refinement levels 1 - 2 - 3 respectively. For reference, a 95% confidence interval is plotted around the mean stress-strain estimator in blue, and a $\pm 1\sigma$ interval is plotted for the sample in cyan.

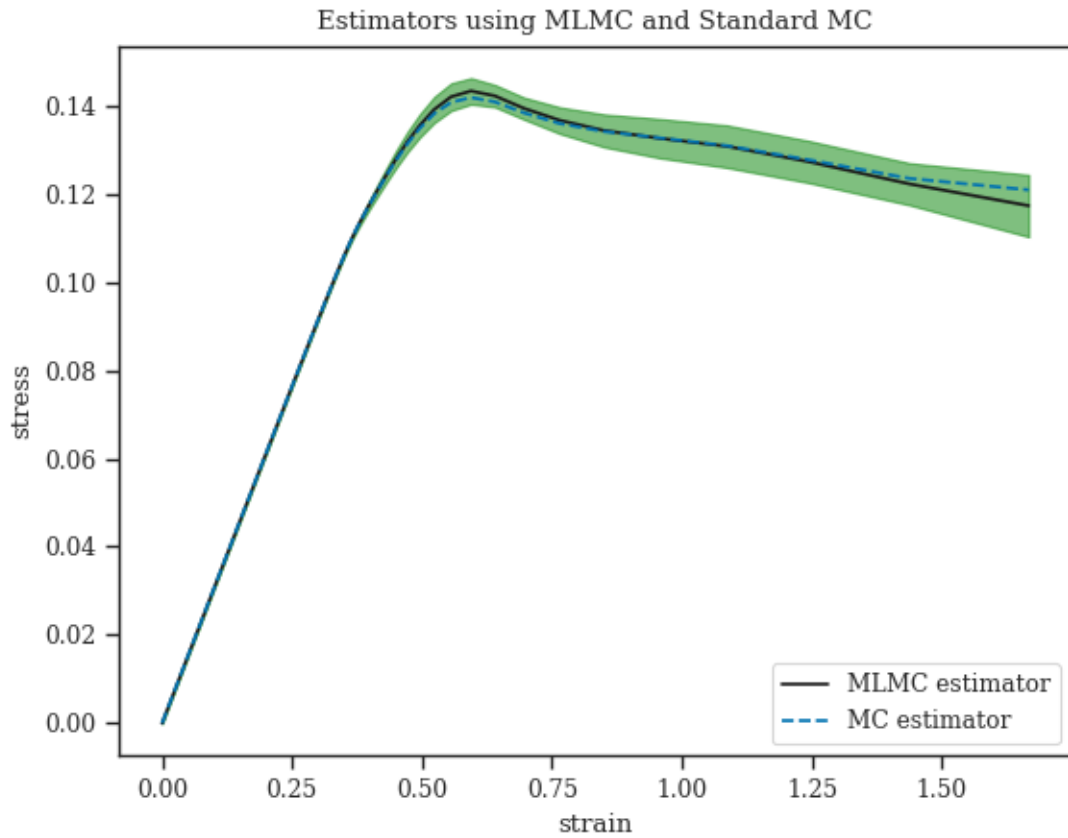


Figure 6.3: Comparison of stress-strain curve estimators using MLMC and standard MC (see Chapter 5). The green band indicates a 95% confidence interval around the MLMC estimator. As a result, we are able to recover the standard MC estimator to within 95%.

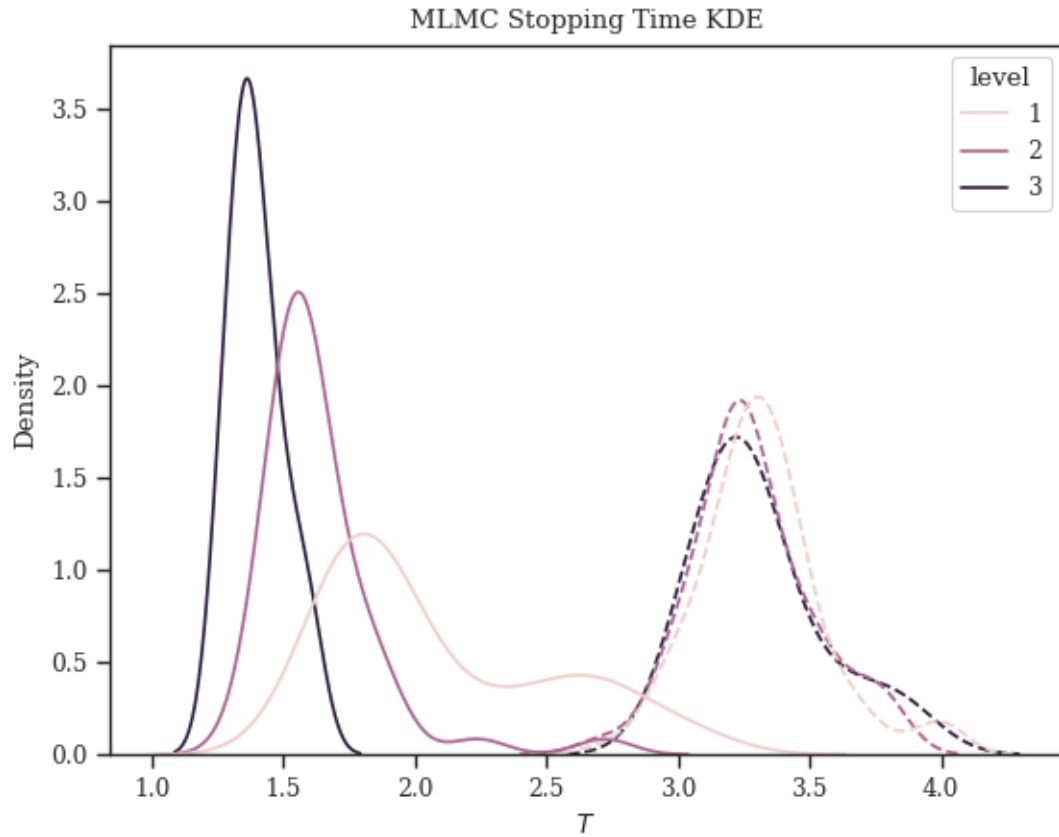


Figure 6.4: Raw KDEs for stopping times in the notched uniaxial stress problem using MLMC hierarchy. In solid lines are the KDE for T_{start} and in dashed are the KDE for T_{fail} .

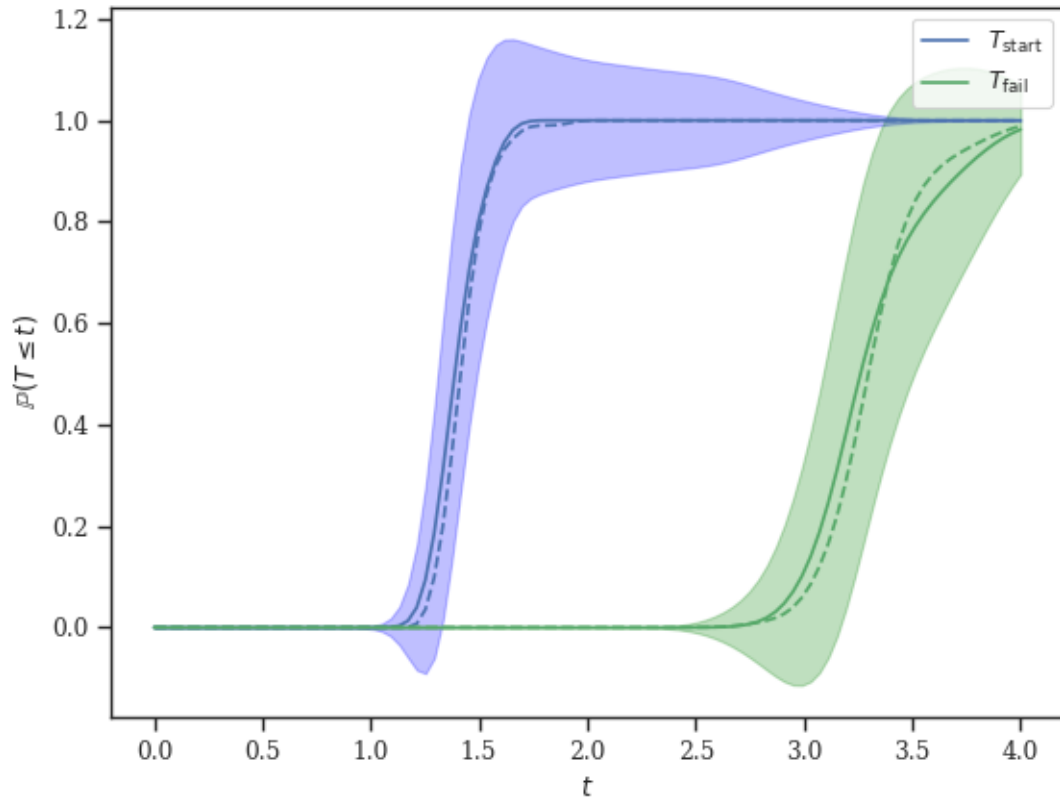


Figure 6.5: Construction of stopping time CDF for both T_{start} and T_{fail} . In solid lines are the CDFs constructed using the MLMC probability procedure discussed above. In dashed are the CDFs built using standard MC methods, using 100 samples at the highest refinement level. Using the pointwise variance of the indicator function, 95% confidence intervals are shaded around the MLMC CDF estimators. As a result, we are able to reconstruct the CDF from the MC framework with 95% confidence.

6.4.5 Damage Distribution

As described above, T_{fail} gives the final time in the problem at which the problem represents a physical laboratory experiment. We take the final damage distribution to be the damage at this time:

$$\mathcal{D}_{\text{final}}(\underline{x}) := \mathcal{D}(\underline{x}, T_{\text{fail}}). \quad (6.70)$$

We would like to apply MLMC to this damage variable to obtain a more precise estimate with less computational effort. However, doing so presents a few challenges.

First, standard MLMC, like that used in the stress-strain procedure above, will likely yield erroneous values on the damage variable. In the PDE framework, the damage variable is bounded between 0 and 1, so much like with probabilities, standard MLMC can yield negative values. However, applying the probability MLMC procedure above is not true to the nature of the damage variable. The damage variable is not intended to be treated as a probability, so it would be dishonest to examine it as such.

Instead, we can deliberately construct a probability out of the damage variable. Consider a tolerance value d_0 , which acts similar to an engineering tolerance. Suppose we are interested in the probability that $\mathcal{D} \geq d_0$. Then we can apply MLMC to the indicator function: $\mathbb{1}(\mathcal{D}_{\text{final}}(\underline{x}) \geq d_0)$, which lends itself exactly to the probability MLMC procedure. In principle, we could apply this to each $d_0 \in [0, 1]$ building a four-dimensional probability $P(\underline{x}, d_0)$. This is difficult to visualize in its entirety. Instead we will view a slice of this variable.

To exemplify how this idea could be used, consider $d_0 = 0.25$. We wish to determine in the MLMC hierarchy, what is the probability at each $\underline{x} \in \Omega$ that $\mathcal{D}_{\text{final}}(\underline{x}) \geq d_0$. The QoI is then $\mathbb{1}(\mathcal{D}_{\text{final}}(\underline{x}) \geq d_0)$, to which we apply the probability MLMC procedure. As discussed in above, there are multiple ways to build the conditional probabilities between levels used to update the final distribution. To avoid added complexity, instead of using the joint-KDE approach for high dimensional data, we will instead opt for the sum-of-indicators approach. The resulting probability field can be seen in Figure 6.6. Additionally, the variance on this QoI can be seen in Figure 6.7.

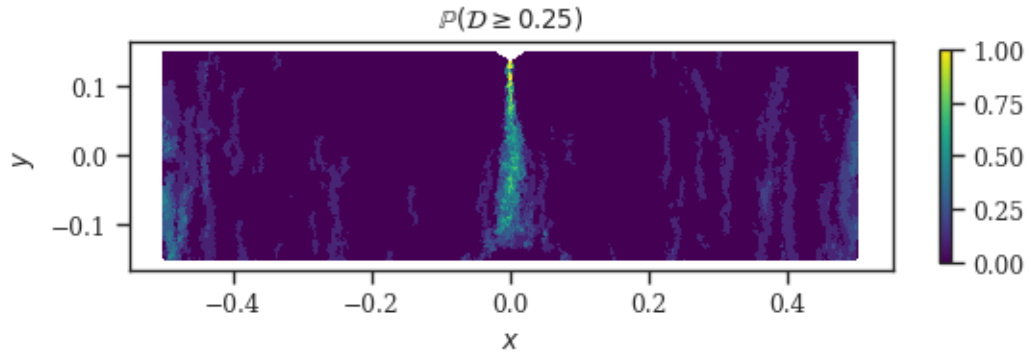


Figure 6.6: Probability the final physical damage is larger than a cutoff value for the MLMC hierarchy. The only area where this is almost sure is near the tip of the notch on the upper boundary. This fans out as it proceeds lower in the domain, and there are very few regions indicating damage away from the center of the domain.

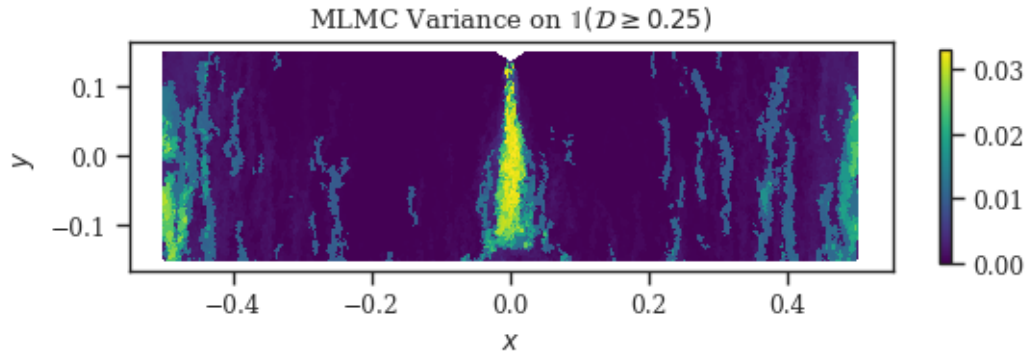


Figure 6.7: MLMC Variance on $\mathbb{1}(\mathcal{D}_{\text{final}}(\underline{x}) \geq d_0)$. The high variance near the center of the domain indicates variability in crack path. The variations along the sides of the domain indicate that some simulations exhibit additional cracking on the boundaries due to the forcing.

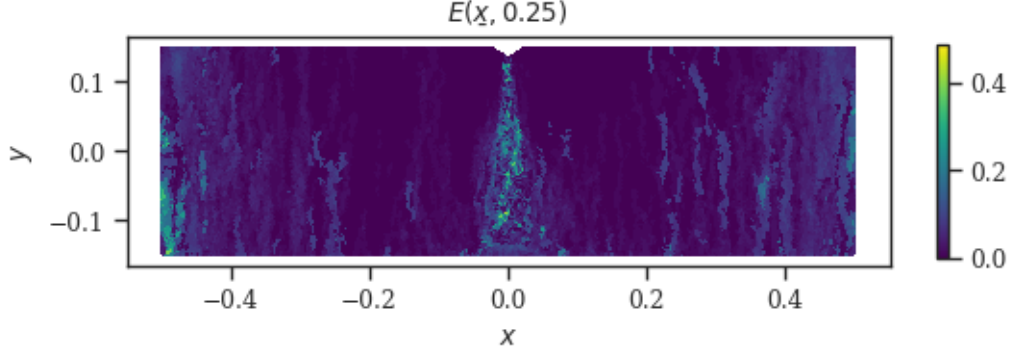


Figure 6.8: Error between MLMC and MC probability for $\mathbb{P}(\mathcal{D}_{\text{final}} \geq d_0)$.

Consider building the same estimator using the standard MC procedure in Chapter 5. We can examine the error between the MLMC and MC estimators. Let $p(\underline{x}; d_0) = \mathbb{P}(\mathcal{D}_{\text{final}}(\underline{x}) \geq d_0)$ and further define $p^{(MLMC)}(\underline{x}; d_0)$ as being the value of p as built using MLMC, and similarly for $p^{(MC)}$. Then consider the error $E(\underline{x}; d_0) = |p^{(MLMC)}(\underline{x}; d_0) - p^{(MC)}(\underline{x}; d_0)|$. A plot of $E(\underline{x}; d_0)$ can be seen in Figure 6.8. The higher error values indicate that the MLMC hierarchy used for the stress-strain curve is insufficient to reconstruct the damage probability fields within 95% confidence. This clearly demonstrates that different QoIs may need different hierarchies to achieve desired accuracies in their estimator calculations.

6.5 MLMC on One Dimensional Model for Various Time Steps

Building on the work done in [32], we examine an MLMC approach to the one-dimensional uniaxial strain damage mechanics problem. In one dimension, the uniaxial strain damage mechanics problem reads

$$\frac{\partial^2 v}{\partial t^2} + \eta_1 \frac{\partial v}{\partial t} - \eta_2 \frac{\partial}{\partial t} \frac{\partial^2 v}{\partial x^2} = \frac{\partial}{\partial x} \left((1 - \mathcal{D}) \frac{\partial v}{\partial x} \right), \quad x \in (0, 1); t \in (0, t_{\max}) \quad (6.71)$$

$$v \Big|_{x=0} = 0, \quad v \Big|_{x=1} = ct \quad t \in [0, t_{\max}] \quad (6.72)$$

$$v \Big|_{t=0} = \frac{\partial v}{\partial t} \Big|_{t=0} = 0 \quad x \in [0, 1]. \quad (6.73)$$

Where $c > 0$ is a constant expansion speed. To distinguish the 1D case from the multi-dimensional case, we use v for the scalar 1D displacement. In 1D, it can be shown [74]

Level (ℓ)	No. Time Steps (M_ℓ)	$v_\ell := \max_t \text{Var}[\hat{\sigma}_\ell(t)]$
1	10	2.93×10^{-2}
2	20	2.42×10^{-2}
3	50	1.48×10^{-2}
4	100	1.31×10^{-2}

Table 6.2: Hierarchy structure of 1D MLMC for various Δt values. Maximum variances over stress-strain curves are also shown.

that P1 FEM is equivalent to second-order centered finite differences. Additionally, we employ the Generalized- α method for time stepping the semidiscretized problem. Using the parameters $\alpha_f = \alpha_m = 0$, returns the Generalized- α method to the Newmark- β time stepping method, as used in [32].

In [32], we demonstrated this approach exhibits first-order convergence in time and second-order convergence in space discretizations. For this experiment in MLMC, we will vary the timestep, Δt used in Newmark- β . While the previous example used refinement levels that exhibited second-order convergence with increasing resolution, here it will only exhibit first-order. For this experiment, let Δt_ℓ be the timestep used at level ℓ for $\ell = 1, 2, \dots, L$. The number of solves forward in time will then be

$$M_\ell = \text{ceil}(T/\Delta t_\ell). \quad (6.74)$$

Because we will not change the spatial discretization for this experiment, the workload for each simulation is directly proportional to M_ℓ , so without loss of generality, we can take $W_\ell = M_\ell$. We examine two QoIs for this process - the stress-strain curve and the stopping time corresponding to when the first damage value equals 1.

For this experiment, we set $t_{\max} = 5$ and $c = 0.2$. We used Δt_ℓ values and M_ℓ values as given in Table 6.2. Table 6.2 also lists the variances determined for each level using a collection of 50 seed runs. These variances are that of the stress-strain curve by computing the variance pointwise for each time step, then computing the maximum value.

Level (ℓ)	No. Required Samples
1	300
2	195
3	100
4	65

Table 6.3: Number of samples to achieve a variance on the stress-strain curve bounded above by 6×10^{-4} . Values have been rounded up to the nearest 5.

6.5.1 Stress Strain Curve

The first QoI will be the stress-strain curve. It will be defined analogously to that in previous sections. Note that in 1D, the strain can be shown

$$\varepsilon = \frac{\partial v}{\partial x}, \quad (6.75)$$

where v is the 1D displacement. Therefore,

$$\hat{\varepsilon} = \int_0^1 \frac{\partial v}{\partial x} dx = ct, \quad (6.76)$$

$$\hat{\sigma} = \int_0^1 (1 - \mathcal{D}) \frac{\partial v}{\partial x} dx, \quad (6.77)$$

$$\mathcal{S} : \hat{\varepsilon} \mapsto \hat{\sigma}. \quad (6.78)$$

Note that determining the stress-strain curve is thus equivalent to determining the chronological stress distribution. At each level, let $\hat{\sigma}_\ell$ denote the stress computed at refinement level ℓ . The resulting stress values are each defined on different strain or time grids. They can be directly compared by interpolating each onto the strain or time grid from level $\ell = L = 4$.

If we require the maximum variance on the stress-strain curve to be bounded above by 6×10^{-4} , applying (6.17) gives the distribution in Table 6.3. Where, again, values have been rounded up to the nearest 5.

Next, we compare this MLMC procedure against a standard MC procedure. The results can be seen in Figure 6.9. The analogous MC procedure would be to build the stress-strain estimator using only 300 samples generated at level 4. This shows the MLMC estimator on the mean stress-strain curve, with a 95% confidence interval

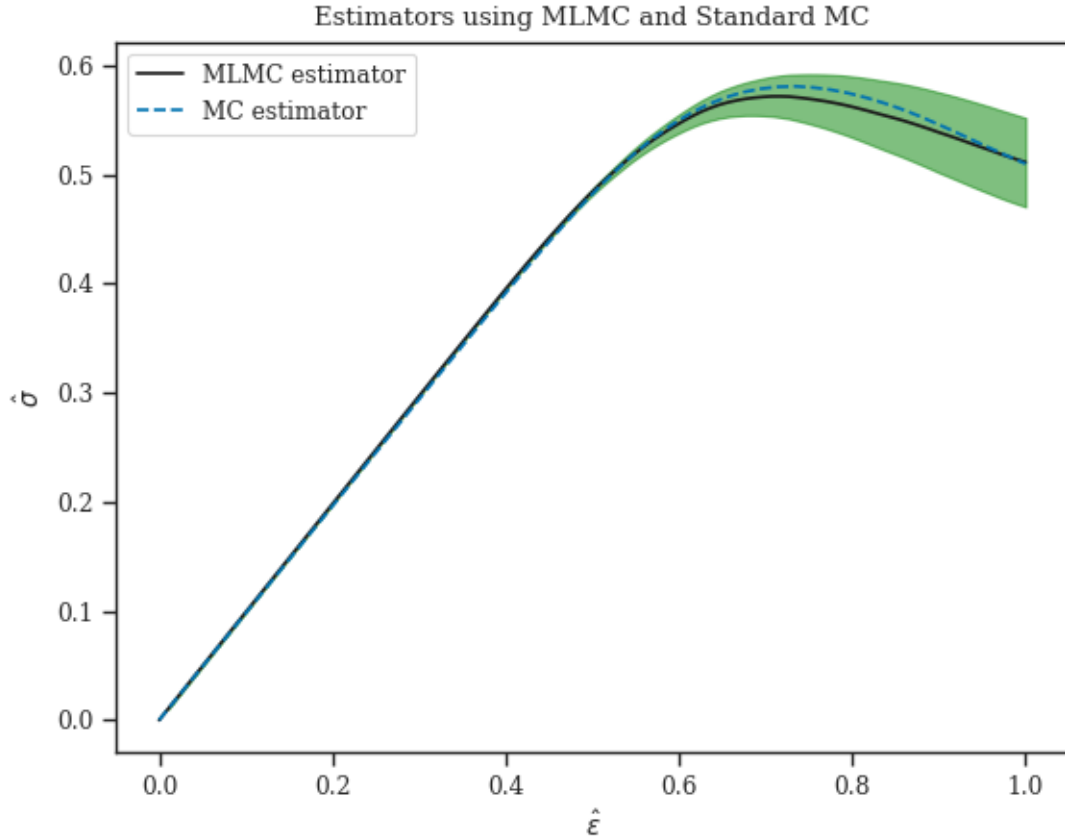


Figure 6.9: Estimators on the mean stress-strain curve for the 1D uniaxial strain model computed using an MLMC hierarchy (solid) and standard MC procedures (dashed). The banded region indicates a 95% confidence interval around the MLMC estimator.

around this estimator. Based on the workloads for each refinement level, the MLMC has a total workload of 18,400 FLOPs, while the standard MC estimator had a required workload of 30,000 FLOPs. So doing MLMC yields a computational savings of 38.7 %.

6.5.2 Stopping Time

As the next part of this experiment, we consider MLMC on the stopping time corresponding to when the damage value first reaches 1. This time indicates when the real-world analog of this problem would break, meaning the model is no longer physical. To highlight the difficulty in using an MLMC procedure for this QoI, Figure 6.10 shows the histogram plots of the resulting stopping time distribution, with a kernel density

estimator overlaid. The number and spacing of the histogram bins are affected by the various time steps for each refinement level. Consequentially, for level 1, it is evident that the KDE is low quality due to the spacing between allowed values of the stopping time.

Setting aside the issue of the KDE on level 1, determining the MLMC estimator for the distribution of this variable boils down to determining the conditional probabilities between refinement levels. Because of the time-node differences between levels, we will opt for using the subsampling approach rather than using a joint KDE. The results can be seen in Figure 6.11. Here, we also plot the CDF for the stopping time using a standard MC approach with only 300 samples at the highest refinement level. The MC estimator is contained within the 95% confidence interval around the MLMC estimator. The agreement between the two demonstrates the robustness of this probability MLMC procedure in dealing with lower resolved initial configurations.

6.6 MLMC Between 1D and 2D Models

Consider the uniaxial tensile problem with Dirichlet forcing conditions. So far, we have examined two separate models for this physical problem, one is a 1D model discussed in [32] and in the previous section, the other was discussed in Chapter 5, as the 2D uniaxial strain problem. In this section, we will apply a similar approach as in [72]. We will apply MLMC to the 1D and 2D models, considering each as a different refinement level of the problem.

The two-dimensional system is much more expensive to solve than the one-dimensional system. We can use MLMC to incorporate information from both the 1D and 2D models, giving a better estimate for QoI estimators from the 2D model for less computation cost than using standard MC methods on only the 2D model. For

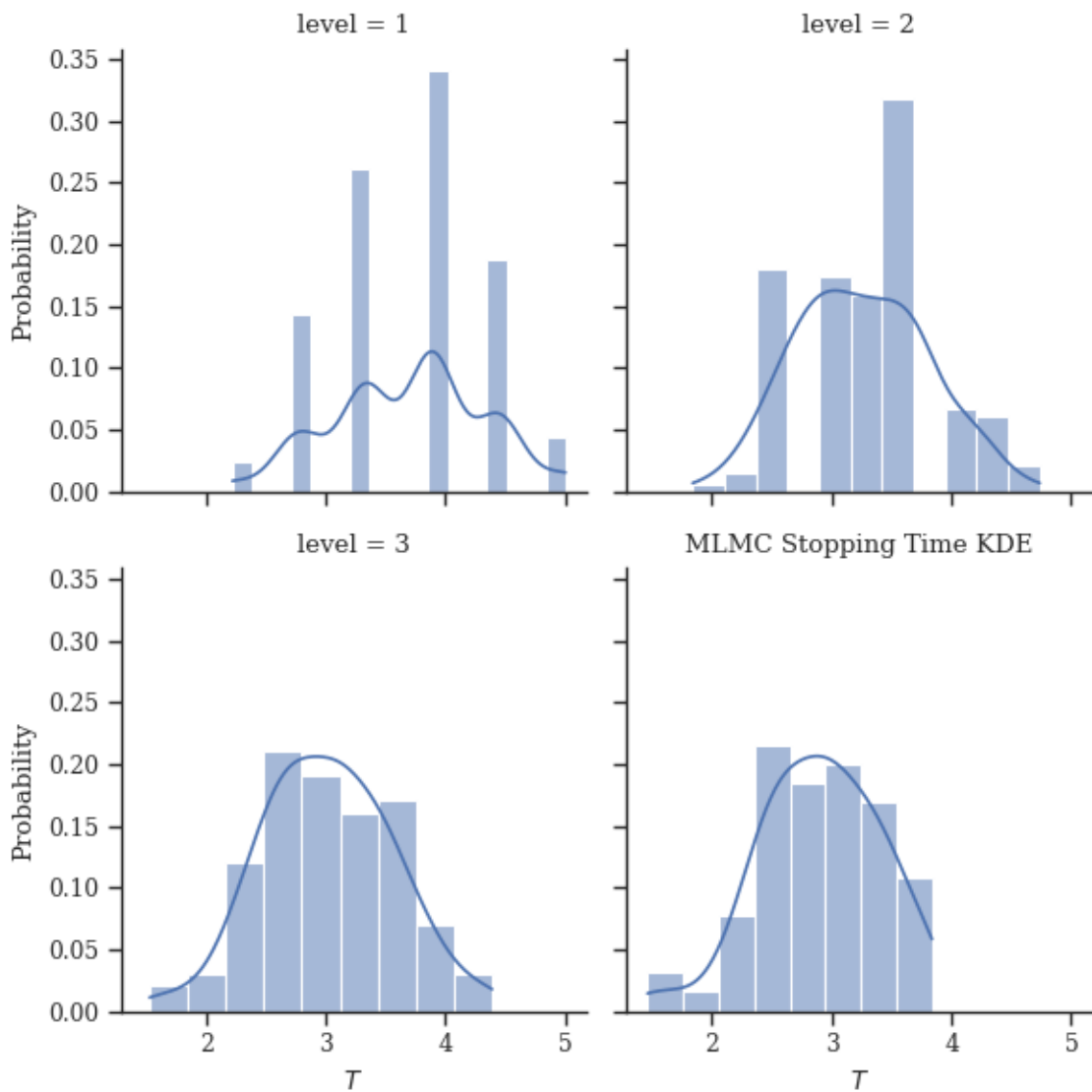


Figure 6.10: Comparison of stopping time distributions for various levels in the MLMC hierarchy from Table 6.3 for the 1D uniaxial strain problem. The coarseness of time steps at level 1 create a low quality KDE, while higher refinement levels appear to fix the problem.

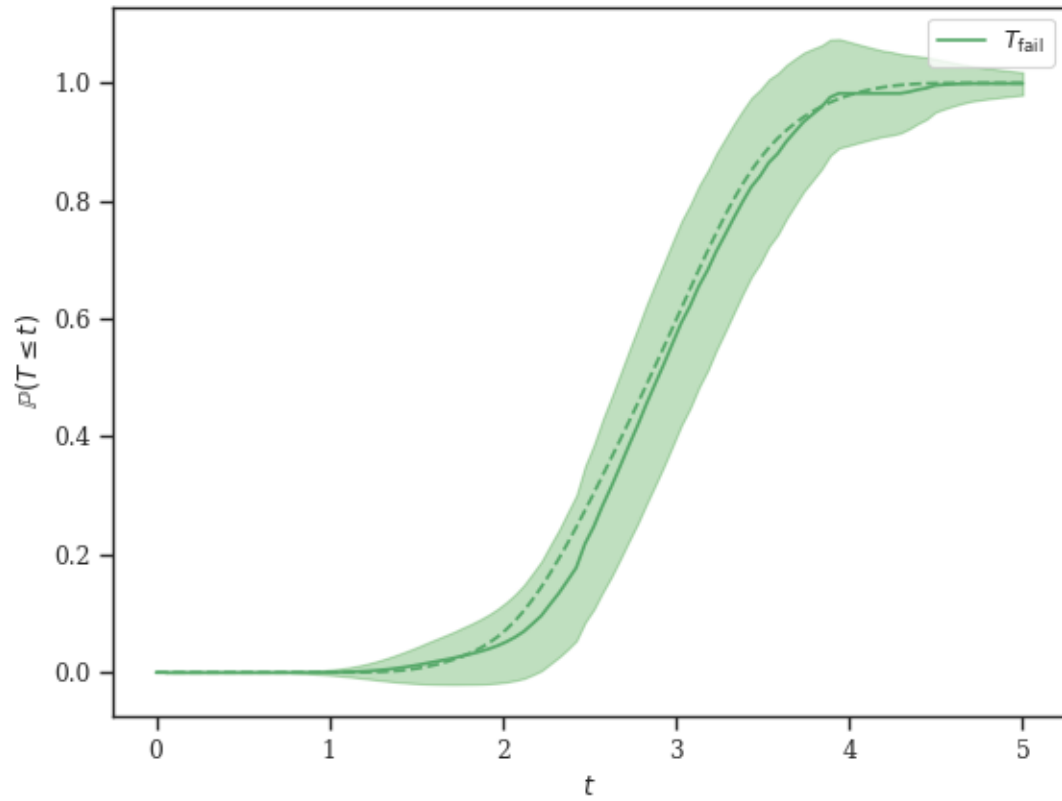


Figure 6.11: Comparison of CDFs for stopping time distribution as computed using an MLMC hierarchy in Table 6.3, and standard MC framework. The MC estimator is within a 95% confidence interval of the MLMC estimator.

convenience, recall the 2D uniaxial strain problem statement:

$$\frac{\partial^2 \underline{u}}{\partial t^2} + \eta_1 \frac{\partial \underline{u}}{\partial t} - \eta_2 \frac{\partial}{\partial t} (\nabla \cdot \underline{\sigma}^{(L)}) = \nabla \cdot ((1 - \mathcal{D}) \underline{\sigma}^{(L)}), \quad \underline{x} \in (0, 1) \times (0, w), \quad (6.79)$$

$$\underline{\sigma}^{(L)} = \mu \nabla \underline{u} + \mu (\nabla \underline{u})^T + \lambda (\nabla \cdot \underline{u}) \underline{I}, \quad (6.80)$$

$$\underline{u} \Big|_{x=0} = \underline{0}, \quad \underline{u} \Big|_{x=1} = ct \underline{e}_x, \quad \underline{\sigma}^{(L)} \cdot \underline{n} \Big|_{y=0, w} = \underline{0}, \quad (6.81)$$

$$\underline{u} \Big|_{t=0} = \frac{\partial \underline{u}}{\partial t} \Big|_{t=0} = \underline{0}. \quad (6.82)$$

Next, recall the 1D analog:

$$\frac{\partial^2 v}{\partial t^2} + \eta_1 \frac{\partial v}{\partial t} - \eta_2 \frac{\partial}{\partial t} \frac{\partial^2 v}{\partial x^2} = \frac{\partial}{\partial x} \left((1 - \mathcal{D}) \frac{\partial v}{\partial x} \right), \quad x \in (0, 1), \quad (6.83)$$

$$v \Big|_{x=0} = 0, \quad v \Big|_{x=1} = ct, \quad (6.84)$$

$$v \Big|_{t=0} = \frac{\partial v}{\partial t} \Big|_{t=0} = 0. \quad (6.85)$$

To avoid any confusion, we let v denote the displacement in the 1D case, and \underline{u} denote the displacement in the 2D case. In the MLMC framework we will consider this as a problem with two refinement levels. Level $\ell = 1$ will correspond to the 1D model, while level $\ell = 2$ will be that of the 2D model.

Both of the above models represent the same physical problem; however, both are very different mathematically. Because we are solving each problem numerically, the cost level will be based on the number of discretization points used in both space and time. In addition, MLMC requires we have a way to evaluate a given sample in both frameworks. That is, we need a 1D representation for the 2D spatially varying fields describing Σ . To this end, we will consider the 1D problem as an average of the 2D problem along the y axis,

$$v \approx U := \frac{1}{w} \int_0^w u_1 dy, \quad (6.86)$$

where u_1 denote the x -component of the displacement vector, \underline{u} . Simply integrating the 2D PDE along the y -axis yields

$$\frac{\partial^2 U}{\partial t^2} + \eta_1 \frac{\partial U}{\partial t} - \eta_2 \frac{\partial}{\partial t} \frac{\partial}{\partial x} \frac{1}{w} \int_0^w \sigma_{xx}^{(L)} dy = \frac{\partial}{\partial x} \frac{1}{w} \int_0^w (1 - \mathcal{D}) \sigma_{xx}^{(L)} dy. \quad (6.87)$$

Here, we are using the stress-free condition on the top and bottom boundaries: $\sigma_{xy} = \sigma_{yx} = 0$ when $y = 0$ and $y = w$. Next, using the relation $\sigma_{xx}^{(L)} = (2\mu + \lambda) \frac{\partial u_x}{\partial x} + \lambda \frac{\partial u_y}{\partial y}$ we can see

$$\frac{\partial}{\partial x} \frac{1}{w} \int_0^w \sigma_{xx}^{(L)} dy = (2\mu + \lambda) \frac{\partial^2 U}{\partial x^2} + \frac{\lambda}{w} \varepsilon_{xy} \Big|_{y=0}^{y=w}. \quad (6.88)$$

Using that $\sigma_{xy}^{(L)} = 2\mu \varepsilon_{xy} = 0$ when $y = 0, w$ removes the boundary term above. Lastly, the final term has

$$\frac{\partial}{\partial x} \frac{1}{w} \int_0^w (1 - \mathcal{D}) \sigma_{xx}^{(L)} dy = (2\mu + \lambda) \frac{\partial}{\partial x} \frac{1}{w} \int_0^w (1 - \mathcal{D}) \frac{\partial u_1}{\partial x} dy + \lambda \frac{\partial}{\partial x} \frac{1}{w} \int_0^w (1 - \mathcal{D}) \frac{\partial u_2}{\partial y} dy. \quad (6.89)$$

Neither term on the right-hand side yields an easy simplification, as no information is specified about u_2 . Instead, we suppose that each term in the 1D analog represents a y -average of the corresponding term in the 2D model. Therefore the 1D analog then simply makes the substitution:

$$\frac{\partial}{\partial x} \frac{1}{w} \int_0^w (1 - \mathcal{D}) \sigma_{xx}^{(L)} dy \rightarrow (2\mu + \lambda) \frac{\partial}{\partial x} \left((1 - \bar{\mathcal{D}}) \frac{\partial U}{\partial x} \right), \quad (6.90)$$

$$\bar{\mathcal{D}} = \frac{1}{w} \int_0^w \mathcal{D} dy. \quad (6.91)$$

And assumes that $\int_0^w (1 - \mathcal{D}) \frac{\partial u_2}{\partial y} dy = 0$. Thus we can expect differences between the same sample when generated on the 1D model and y -averaged on the 2D model. Moreover, this substitution provides the method for how to cast a 2D sample for Σ into the 1D context:

$$\Sigma^{(1D)} := \bar{\Sigma} = \frac{1}{w} \int_0^w \Sigma^{(2D)} dy. \quad (6.92)$$

Based on (6.92), we have a procedure to generate a sample in both the 2D and 1D models. To construct the MLMC procedure, let N_{1D} be the number of samples that will be generated for the 1D model, and let N_{2D} be the number of samples for the 2D model. We further assume that because of the relative costs of the model, $N_{1D} > N_{2D}$. We can perform MLMC as follows:

1. Generate samples $\Sigma^{(n)}$ in the 2D problem for $n = 1, 2, \dots, N_{1D}$

2. For each critical stress sample, compute

$$\bar{\Sigma}^{(n)} = \frac{1}{w} \int_0^w \Sigma^{(n)} dy. \quad (6.93)$$

3. Evaluate the QoIs in the 1D context using $Q_1^{(n)} = (\mathcal{Q} \circ \mathcal{F}_{1D})(\bar{\Sigma}^{(n)})$ for $n = 1, 2, \dots, N_{1D}$

4. For samples $n = 1, 2, \dots, N_{2D}$, evaluate the corresponding QoIs in the 2D context using $Q_2^{(n)} = (\mathcal{Q} \circ \mathcal{F}_{2D})(\Sigma^{(n)})$

5. Perform the appropriate MLMC synthesis on the resulting values $\{Q_\ell^{(n)}\}$ for $n = 1, 2, \dots$ and $\ell = 1, 2$

In addition, the number of samples for each level can be computed by using a collection of seed samples on each model and applying the formula in (6.17) or (6.19).

6.6.1 Quantities of Interest

The goal of this problem will be as follows. Generate two QoI estimators: the stress-strain curve and the time of first damage. Then we ultimately wish to construct a figure similar to Figure 5.12 in Chapter 5. This would allow a researcher to interpret the relationship between the yielding in the stress-strain curve and the time at which damage begins accumulating.

The first QoI required is the stress-strain curve. To create a uniform framework for building this QoI in both the 1D and 2D case, we consider the output from the 1D problem as having tensor-valued stress and strain, with

$$\underline{\underline{\varepsilon}}^{(1D)} = \begin{bmatrix} \frac{\partial v}{\partial x} & 0 \\ 0 & 0 \end{bmatrix}, \quad \underline{\underline{\sigma}}^{(1D)} = (2\mu + \lambda)(1 - \bar{\mathcal{D}})\underline{\underline{\varepsilon}}^{(1D)}. \quad (6.94)$$

Then we can write the stress-strain QoI in the same way for each refinement level:

$$\hat{\varepsilon} = \frac{1}{|\Omega|} \int_{\Omega} \varepsilon_{xx} dx = ct, \quad (6.95)$$

$$\hat{\sigma} = \frac{1}{|\Omega|} \int_{\Omega} \sigma_{xx} dx, \quad (6.96)$$

$$\mathcal{S} : \hat{\varepsilon} \mapsto \hat{\sigma}. \quad (6.97)$$

Level	# DoFs	N_t	Workload, W_ℓ
1	50	200	10,000
2	3,132	50	156,600

Table 6.4: MLMC Workloads for each level in the 1D-2D experiment. Total workload W_ℓ is computed as the product of # DoFs and N_t . The values of # DoFs is the number of degrees of freedom in the spatial discretization, while N_t is the number of time nodes in the chronological integration of the system.

Where Ω is the appropriate domain for the problem, and $|\Omega|$ is the area (or length) of the domain, computed as

$$|\Omega| = \int_{\Omega} 1 \, dx. \quad (6.98)$$

The second QoI is the stopping time for when the damage begins accumulating, T_{start} , which can be written

$$T_{\text{start}} = \int_{t>0} \{t \in [0, T] : \mathcal{D}(\cdot, t) > 0\}, \quad (6.99)$$

for some point in the respective problem domain. To convert the stopping time and enable its distribution to be plotted on the stress-strain curve, we can use the relation that

$$\hat{\varepsilon}(t) = ct, \quad (6.100)$$

due to the Dirichlet boundary conditions of the uniaxial strain problem.

6.6.2 MLMC Sampling and Results

Using a collection of 10 seed runs for the level 1 and 2 models, the maximum chronological variance of the stress bias (see (6.64) - (6.66)), is used along with the workloads of each refinement level to compute the optimal number of samples according to (6.17). The workloads used are based on the number of time steps used and the size of the linear-algebra system used to propagate the solution forward each step. The discretizations are shown in Table 6.4. Requiring the standard error to be bounded by 10^{-4} , (6.17) yields the sampling distribution as shown in Table 6.5.

Level	$N_\ell^{(opt)}$
1	100
2	30

Table 6.5: Optimal number of samples for each refinement level in the 1D-2D MLMC uniaxial strain experiment.

We start by examining the raw data, shown in Figure 6.12. This figure illustrates the bias between the 1D and 2D models. MLMC should correct for this bias in both the stress-strain and KDE plots.

6.6.3 Results

From these samples, we apply standard MLMC pointwise in time on the stress-strain curve to obtain a better stress-strain curve estimator. Since the 1D model uses coarser time stepping than the 2D model, we interpolate the 1D model results onto the time grid of the 2D model.

We also apply the joint-KDE probability MLMC on the stopping time to obtain a better estimator on the CDF for the stopping time. Once this CDF is obtained, we can compute the standard deviation pointwise. This can be seen in Figure 6.13, which shows the CDF estimator with $\pm 1\zeta$ bounds. Recall that the $\pm 1\zeta$ bounds can be used directly with (4.40) to give bounds on the estimator under an alternative model. Differentiating the CDF with respect to time yields an approximate PDF for this stopping time, which can be overlaid with the aforementioned stress-strain curve estimator. The result can be seen in Figure 6.13.

On examining Figure 6.13, one can make some inferences about the behavior of the problem. First, it is clear that the damage is most likely to start at some point before the peak in the stress-strain curve. Consequentially, one could infer a relationship between the time at which damage starts and the time at which the system will start to yield. Moreover, it is clear that this may not be the case every time due to the extension of the PDF estimator past the yield point in the stress-strain curve.

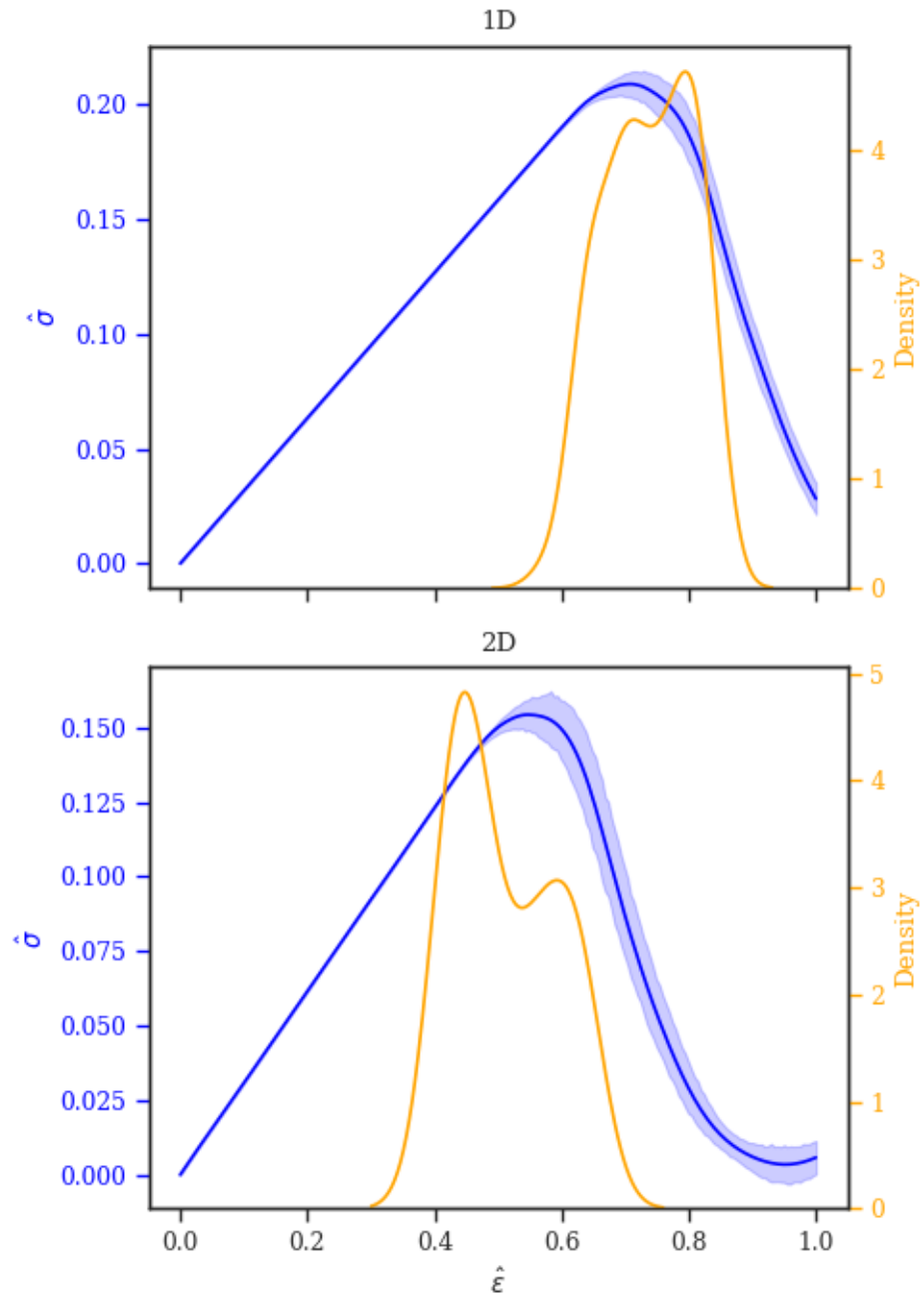


Figure 6.12: Comparison of stress-strain curves and T_{start} KDE for 1D and 2D sampling ensembles before performing MLMC.

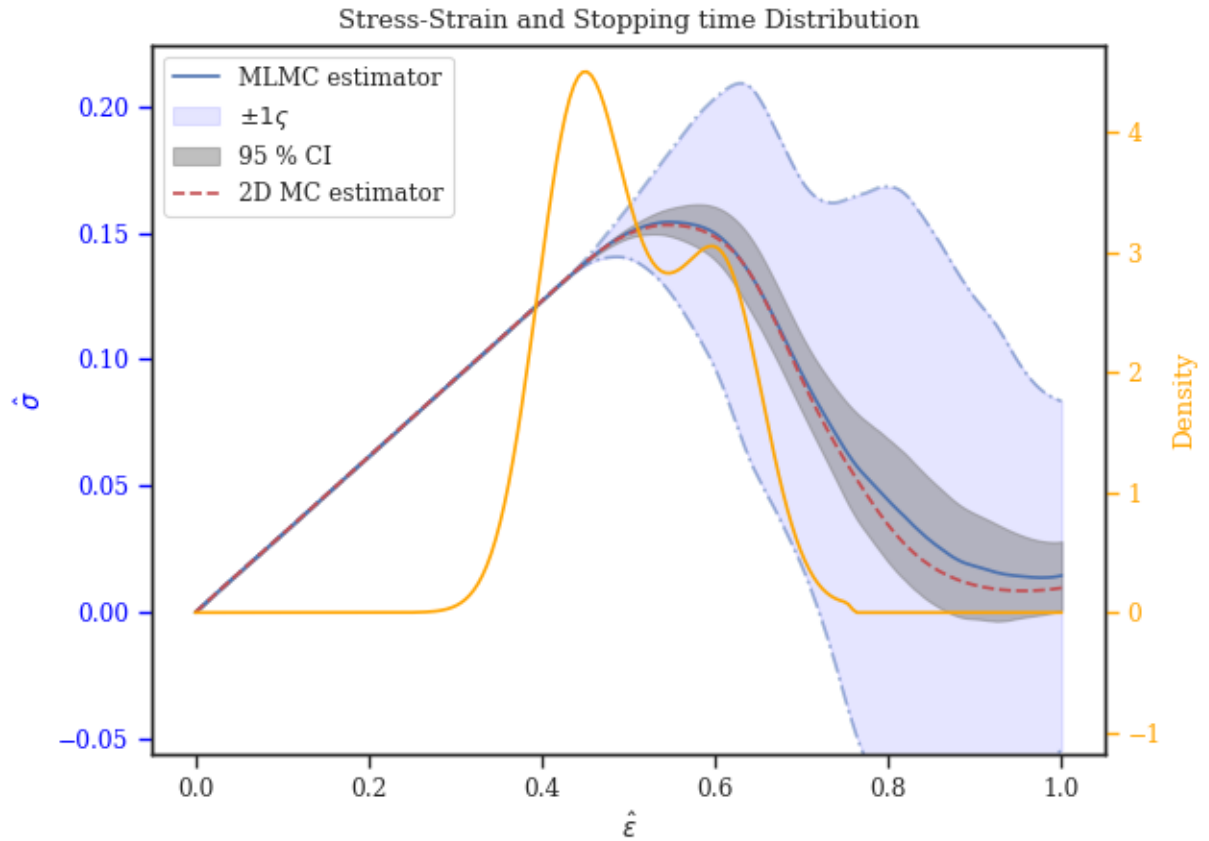


Figure 6.13: Stress-strain curve and PDF for T_{start} estimators using the 1D-2D MLMC sampling distribution. In blue is a 95 % confidence interval around the mean stress-strain curve estimator, and in cyan is a $\pm 1\zeta$ interval indicating UQ bounds.

Thus, if examining this figure in the context of a real system, one must be cautious about using the value of T_{start} to infer when a material is losing its structural integrity.

Consider further the computational costs which went into generating the above results. Based on the total number of samples at each refinement level, the workload which went into generating Figure 6.13 was approximately 5,698,000 FLOPs. However, a standard MC approach would have only used 100 simulations at level 2 (2D model). The resulting workload would have been 15,660,000 FLOPs, which is almost three times as high.

6.7 Discussion and Conclusions

For high dimensional problems, such as PDEs, which depend on randomly varying fields, MC sampling methods may be one of the few approaches which can generate reliable results, albeit at significant computational costs. Since MC methods rely on the CLT, additional significant figures in estimators require increasing sampling numbers by two orders of magnitude. MLMC methods thus provide a tunable workaround for such computational costs. By combining many lower-resolution samples with selected numbers of higher-resolution samples, it becomes possible to generate similar quality estimators to those of high-quality MC methods, with significantly lower costs. Moreover, MLMC is tunable, so one can minimize the required workload for an MLMC procedure with simple formulas while maintaining a desired level of precision. Ultimately, the distribution of the samples across the various levels is highly dependent on the statistics of the QoI being measured, so one must be cautious about the statistics used in the optimization.

The MLMC methods are very flexible in that way. There are many metrics that can be used to compute the workloads and precisions at each sample. This means MLMC can be easily customized to different problems and specific requirements. Several methods were presented in this thesis - using MLMC for real scalars, real functions, probability distributions, and for probability fields. By doing so, we demonstrated applications of MLMC techniques to areas beyond the CLT while maintaining an easy

metric for overall precision.

The problems presented in this thesis simulate damage mechanics problems in various configurations. MLMC methods enable differing simulations to be combined, such as in the 1D-2D uniaxial strain problem. In that particular case, there was a significant error between the two models, which could not be easily removed. This error captured was the boundary terms present in (6.89). Even though these errors were not explicitly handled by the MLMC construction, by determining the biases between each simulation, it is possible to still apply both simulations to the underlying problem.

The MLMC methods lend themselves well to applying methods in uncertainty quantification. The asymptotic bounds in (4.40) mean that for alternative models closely related to the nominal model, only the relative entropy between the models and the standard deviation of the QoI need be computed to place bounds on the uncertainty. Consequentially, model results can be easily extrapolated to other use cases. This further expands on MLMC techniques as a powerful tool in modeling by enabling researchers to make conclusions with incomplete information. Similarly, this UQ capability means one can safely bound the errors between an MLMC simulation using multiple refinements and a similar MC simulation done using only the most refined model. Doing so enables researchers to have more confidence in their results and opens the doors to examining problems that previously were computationally intractable. As a result, MLMC provides a reliable and rigorous framework with which high-resolution and prototype models can be combined to better approximate their real-world counterparts.

BIBLIOGRAPHY

- [1] Clayton, J. D. and Knap, J.. “ A geometrically nonlinear phase field theory of brittle fracture.” *International Journal of Fracture*, 2014
- [2] Ambati, Marreddy and Gerasimov, Tymofiy and De Lorenzis, Laura. “ A review on phase-field models of brittle fracture and a new fast hybrid formulation.” *Computational Mechanics*, 2015
- [3] Roubíček, Tomáš. “ Models of dynamic damage and phase-field fracture, and their various time discretisations.” In *Topics in Applied Analysis and Optimisation*. Springer, 2019
- [4] Wheeler, MF and Wick, T and Wollner, W. “ An augmented-Lagrangian method for the phase-field approach for pressurized fractures.” *Computer Methods in Applied Mechanics and Engineering*, 2014
- [5] Knap, Jaroslaw and Clayton, John. “ A Computational Framework for Phase-field Modeling.” *Army Research Laboratory*, 2011
- [6] Tanné, E. and Li, T. and Bourdin, B. and Marigo, J.-J. and Maurini, C.. “ Crack nucleation in variational phase-field models of brittle fracture.” *Journal of the Mechanics and Physics of Solids*, 2018
- [7] Borden, Michael J. and Verhoosel, Clemens V. and Scott, Michael A. and Hughes, Thomas J.R. and Landis, Chad M.. “ A phase-field description of dynamic brittle fracture.” *Computer Methods in Applied Mechanics and Engineering*, 2012
- [8] Bourdin, Blaise and Francfort, Gilles A. and Marigo, Jean-Jacques. “ The Variational Approach to Fracture.” *Journal of Elasticity*, 2008
- [9] Mesgarnejad, A and Bourdin, B and Khonsari, MM3340163. “ Validation simulations for the variational approach to fracture.” *Computer Methods in Applied Mechanics and Engineering*, 2015
- [10] Rosić, Bojana V. and Matthies, Hermann G.. “ Variational Theory and Computations in Stochastic Plasticity.” *Archives of Computational Methods in Engineering*, 2015

- [11] Nukala, Phani Kumar V V and Simunovic, Srdan. “ An efficient algorithm for simulating fracture using large fuse networks.” *Journal of Physics A: Mathematical and General*, 2003
- [12] de Arcangelis, L. and Redner, S. and Herrmann, H.J.. “ A random fuse model for breaking processes.” *Journal de Physique Lettres*, 1985
- [13] Batrouni, G. George and Hansen, Alex. “ Fracture in Three-Dimensional Fuse Networks.” *Physical Review Letters*, 1998
- [14] Le, Jia-Liang and Eliáš, Jan and Gorgogianni, Anna and Vievering, Joshua and Kveton, Josef. “ Rate-Dependent Scaling of Dynamic Tensile Strength of Quasibrittle Structures.” *Journal of Applied Mechanics*, 2017
- [15] Yang, Zhenjun and Frank Xu, X.. “ A heterogeneous cohesive model for quasibrittle materials considering spatially varying random fracture properties.” *Computer Methods in Applied Mechanics and Engineering*, 2008
- [16] Motamed, Mohammad and Nobile, Fabio and Tempone, Raúl. “ Analysis and computation of the elastic wave equation with random coefficients.” *Computers & Mathematics with Applications*, 2015
- [17] Clouteau, D and Ta, Q A and Cottureau, R. “ Modelling of elastic wave propagation in random media : validation and inversion issues.” *8th International Conference on Structural Dynamics*, 2011
- [18] Bažant, Zdeněk P and Novak, Drahomír. “ Stochastic models for deformation and failure of quasibrittle structures: Recent advances and new directions.” *Computational Modelling of Concrete Structure*, 2003
- [19] Ortiz, M. and Pandolfi, A.. “ Finite-deformation irreversible cohesive elements for three-dimensional crack-propagation analysis.” *International Journal for Numerical Methods in Engineering*, 1999
- [20] “Cohesive Elements.” *Sandia National Laboratory*, 2023
- [21] Park, Kyoungsoo and Paulino, Glaucio H.. “ Cohesive Zone Models: A Critical Review of Traction-Separation Relationships Across Fracture Surfaces.” *Applied Mechanics Reviews*, 2013
- [22] Zhou, Fenghua and Molinari, Jean-François and Ramesh, K.T.. “ A cohesive model based fragmentation analysis: effects of strain rate and initial defects distribution.” *International Journal of Solids and Structures*, 2005
- [23] Li, Shaofan and Liu, Wing Kam. “ Numerical simulations of strain localization in inelastic solids using mesh-free methods.” *International Journal for Numerical Methods in Engineering*, 2000

- [24] Rabczuk, Timon. “ Computational Methods for Fracture in Brittle and Quasi-Brittle Solids: State-of-the-Art Review and Future Perspectives.” *ISRN Applied Mathematics*, 2013
- [25] Weißgraeber, Philipp and Leguillon, Dominique and Becker, Wilfried. “ A review of Finite Fracture Mechanics: crack initiation at singular and non-singular stress raisers.” *Archive of Applied Mechanics*, 2016
- [26] Kovachki, Nikola and Liu, Burigede and Sun, Xingsheng and Zhou, Hao and Bhattacharya, Kaushik and Ortiz, Michael and Stuart, Andrew. “ Multiscale modeling of materials: Computing, data science, uncertainty and goal-oriented optimization.” *Mechanics of Materials*, 2022
- [27] Chernatynskiy, Aleksandr and Phillpot, Simon R. and LeSar, Richard. “ Uncertainty Quantification in Multiscale Simulation of Materials: A Prospective.” *Annual Review of Materials Research*, 2013
- [28] Rajan, Krishna. “ Materials Informatics: The Materials “Gene” and Big Data.” *Annual Review of Materials Research*, 2015
- [29] Conti, S. and Müller, S. and Ortiz, M.. “ Data-Driven Problems in Elasticity.” *Archive for Rational Mechanics and Analysis*, 2018
- [30] Bishop, J. E. and Strack, O. E.. “ A statistical method for verifying mesh convergence in Monte Carlo simulations with application to fragmentation.” *International Journal for Numerical Methods in Engineering*, 2011
- [31] Strack, O.E. and Leavy, R.B. and Brannon, R.M.. “ Aleatory uncertainty and scale effects in computational damage models for failure and fragmentation..” *International Journal for Numerical Methods in Engineering*, 2015
- [32] Plecháč, Petr and Simpson, Gideon and Troy, Jerome R.. “ Well-posedness of a random coefficient damage mechanics model*.” *Applicable Analysis*, 2022
- [33] Le, Jia-Liang and Xu, Zhifeng and Eliáš, Jan. “ Internal Length Scale of Weakest-Link Statistical Model for Quasi-Brittle Fracture.” *Journal of Engineering Mechanics*, 2018
- [34] Lemaitre, J. and Desmorat, R.. *Engineering damage mechanics: ductile, creep, fatigue and brittle failures*. Springer, 2005
- [35] Lemaitre, Jean. *A Course on Damage Mechanics*. Springer Berlin Heidelberg, 1996
- [36] Bazant, Zdenek P. and Le, Jia-Liang. *Probabilistic Mechanics of Quasibrittle Structures: Strength, Lifetime, and Size Effect*. Cambridge University Press, 2017

- [37] Temam, Roger and Miranville, Alain. *Mathematical Modeling in Continuum Mechanics*. Cambridge University Press. 2005
- [38] Loret, Benjamin and Prevost, Jean H.. “ Dynamic strain localization in elasto-(visco-)plastic solids, Part 1. General formulation and one-dimensional examples.” *Computer Methods in Applied Mechanics and Engineering*, 1990
- [39] Bažant, Zdeněk P. and Belytschko, Ted B. and Chang, Ta-Peng. “ Continuum Theory for Strain-Softening.” *Journal of Engineering Mechanics*, 1984
- [40] Su, X.T. and Yang, Z.J. and Liu, G.H.. “ Monte Carlo simulation of complex cohesive fracture in random heterogeneous quasi-brittle materials: A 3D study.” *International Journal of Solids and Structures*, 2010
- [41] Pang, Sze-Dai and Bažant, Zdeněk P. and Le, Jia-Liang. “ Statistics of strength of ceramics: finite weakest-link model and necessity of zero threshold.” *International Journal of Fracture*, 2008
- [42] de Borst, René. “ Fracture in quasi-brittle materials: a review of continuum damage-based approaches.” *Engineering Fracture Mechanics*, 2002
- [43] Bažant, Zdeněk P. and Belytschko, Ted B.. “ Wave propagation in a strain-softening bar: exact solution.” *J. Eng. Mech.*, 1985
- [44] Gourdin, William H.. “ Analysis and assessment of electromagnetic ring expansion as a high-strain-rate test.” *Journal of Applied Physics*, 1989
- [45] Gourdin, W. H. and Weinland, S. L. and Boling, R. M.. “ Development of the electromagnetically launched expanding ring as a high-strain-rate test technique.” *Review of Scientific Instruments*, 1989
- [46] Rodríguez-Martínez, J.A. and Vadillo, G. and Fernández-Sáez, J. and Molinari, A.. “ Identification of the critical wavelength responsible for the fragmentation of ductile rings expanding at very high strain rates.” *Journal of the Mechanics and Physics of Solids*, 2013
- [47] Aizenshtein, Michael and Brosh, Eli and Ungarish, Ziv and Levi, Shlomo and Tubul, Matan and Fadel, Dvir and Greenberg, Eyal and Hayun, Shmuel. “ High entropy uranium-based alloys: Thermodynamics, characterization and mechanical properties.” *Journal of Nuclear Materials*, 2022
- [48] Hackenberg, Robert. “ A Compilation of Tensile Data for Quenched and Aged Uranium-Niobium Alloys.” *Los Alamos National Laboratory*, 2016
- [49] Cathcartt, J. V. and Liu, C. T.. “ The mechanical properties of two uranium alloys and their role in the oxidation of the alloys.” *Oxidation of Metals*, 1973

- [50] Tal, David and Fish, Jacob. “ Stochastic multiscale modeling and simulation framework for concrete.” *Cement and Concrete Composites*, 2018
- [51] Wang, G. and Mattern, N. and Bednarčik, J. and Li, R. and Zhang, B. and Eckert, J.. “ Correlation between elastic structural behavior and yield strength of metallic glasses.” *Acta Materialia*, 2012
- [52] Levy, S. and Molinari, J. F. and Vicari, I. and Davison, A. C.. “ Dynamic fragmentation of a ring: Predictable fragment mass distributions.” *Physical Review E*, 2010
- [53] Zhou, Fenghua and Molinari, Jean-François and Ramesh, K.T.. “ Analysis of the brittle fragmentation of an expanding ring.” *Computational Materials Science*, 2006
- [54] Erlicher, S. and Bonaventura, L. and Bursi, O. S.. “ The analysis of the Generalized- α method for non-linear dynamic problems.” *Computational Mechanics; Heidelberg*, 2002
- [55] Shearer, Christopher M and Cesnik, Carlos E S. “ Modified Generalized- α Method for Integrating Governing Equations of Very Flexible Aircraft.” *American Institute of Aeronautics and Astronautics*, 2006
- [56] Erlicher, Silvano and Bonaventura, Luca and Bursi, Oreste S. “ The analysis of the Generalized- α method for non-linear dynamic problems.” *HAL Archives*, 2008
- [57] Rang, Joachim. “ Adaptive Timestep Control for the Generalised- α Method.” *International Conference on Adaptive Modeling and Simulation*, 2013
- [58] Neter, John and Wasserman, William and Whitmore, G.A. *Applied Statistics*. Allyn and Bacon, Inc, Boston. 1978
- [59] Walsh, John B. *Knowing the Odds An Introduction to Probability*. Americal Mathematical Society Rhode Island. 2011
- [60] Smith, Ralph C. *Uncertainty Quantification Theory, Implementation, and Applications*. SIAM CS& E Philadelphia. 2014
- [61] Carrillo, Christian Caamaño. “ Modeling and estimation of some non Gaussian random fields.” Doctoral. Chile, 2018
- [62] Carmeliet, Jan and de Borst, René. “ Stochastic approaches for damage evolution in standard and non-standard continua.” *International journal of solids and structures*, 1995
- [63] Lord, Gabriel J and Powell, Catherine E and Shardlow, Tony. *An introduction to computational stochastic PDEs*. Cambridge University Press, 2014

- [64] Steven Greene, M. and Liu, Yu and Chen, Wei and Liu, Wing Kam. “Computational uncertainty analysis in multiresolution materials via stochastic constitutive theory.” *Computer Methods in Applied Mechanics and Engineering*, 2011
- [65] Kamaljit, Chowdhary and Paul, Dupuis. “Distinguishing and integrating aleatoric and epistemic variation in uncertainty quantification.” *Mathematical Modelling and Numerical Analysis*, 2013.
- [66] Dupuis, Paul and Katsoulakis, Markos and Pantazis, Yannis and Plechac, Petr. “Path-Space Information Bounds for Uncertainty Quantification and Sensitivity Analysis of Stochastic Dynamics.” *SIAM Journal of Uncertainty Quantification*, 2016.
- [67] Minh, Hà Quang. “Infinite-Dimensional Log-Determinant Divergences Between Positive Definite Trace Class Operators.” *Linear Algebra and its Applications*. 2017
- [68] Majda, A. J. and Gershgorin, B.. “Improving model fidelity and sensitivity for complex systems through empirical information theory.” *Proceedings of the National Academy of Sciences*, 2011
- [69] Collier, Nathan and Haji-Ali, Abdul-Lateef and Nobile, Fabio and von Schwerin, Erik and Tempone, Raul. “A Continuation Multilevel Monte Carlo algorithm.” *BIT Numerical Mathematics*, 2015
- [70] Alsup, Terrence and Peherstorfer, Benjamin. “Context-aware surrogate modeling for balancing approximation and sampling costs in multi-fidelity importance sampling and Bayesian inverse problems.” *SIAM/ASA Journal on Uncertainty Quantification*, 2023
- [71] Brooks, Steve and Gelman, Andrew and Jones, Galin and Meng, Xiao-Li. *Handbook of Markov Chain Monte Carlo*. CRC Press, 2011
- [72] Dhulipala, Somayajulu L. N. and Shields, Michael D. and Chakroborty, Promit and Jiang, Wen and Spencer, Benjamin W. and Hales, Jason D. and Labouré Vincent M. and Prince, Zachary M. and Bolisetti, Chandrakanth and Che, Yifeng. “Reliability Estimation of an Advanced Nuclear Fuel using Coupled Active Learning, Multifidelity Modeling, and Subset Simulation.” *Reliability Engineering and System Safety*. 2022
- [73] Chen, Victor and Dunlop, Matthew M. and Papaspiliopoulos, Omiros and Stuart, Andrew M.. “Dimension-Robust MCMC in Bayesian Inverse Problems.” *arXiv:1803.03344 [stat]*, 2019
- [74] Brenner, Susanne C. and Scott, L. Ridgway *The Mathematical Theory of Finite Element Methods*. Springer, New York. 2010

- [75] Logg, Anders and Mardal, Kent-Andre and Wells, Garth N. *Automated Solution of Differential Equations by the Finite Element Method*. The FEniCS Project. 2011
- [76] M. S. Alnaes, J. Blechta, J. Hake, A. Johansson, B. Kehlet, A. Logg, C. Richardson, J. Ring, M. E. Rognes and G. N. Wells. “The FEniCS Project Version 1.5,” *Archive of Numerical Software* 3 (2015).
- [77] “Darwin Fees.” *University of Delaware, Data Science Institute*. <https://dsi.udel.edu/core/computational-resources/darwin/fees/> 2023
- [78] Strang, Gilbert and Fix, George. *An Analysis of the Finite Element Methods, 2nd Edition*. Wellesley-Cambridge Press. 2008
- [79] Bromideh, Ali Akbar. “Discriminating Between the Weibull and Log-Normal Distributions based on Kullback-Leibler Divergence.” *Istanbul University Econometrics and Statistics e-Journal*, 2012
- [80] Stuart, A. M. “Inverse Problems: A Bayesian Perspective.” *Acta Numerica*, 2010

Appendix A

PYTHON CODE AND ALGORITHMS USED

The source code for the examples and analysis shown throughout this thesis is available at <https://github.com/JeromeTroy/uq-damage/>. Included are installation instructions as well as examples for getting started.